Physical and Numerical Modelling of Landslide-Generated Waves

A Thesis Submitted for the Degree of Doctor of Philosophy by

Ramtin Sabeti

Department of Civil and Environmental Engineering,
Brunel University London

December 2022

Acknowledgements

I would like to express my deepest gratitude to my supervisor, Dr Mohmmad Heidarzadeh, for his support and guidance. It has been an honour and privilege working with such a knowledgeable supervisor. I would like to thank my family, in particular Ms Fatemeh Rafiei, Mr Mohammoud Faghihi, Mrs Zahra Faghihi, and Mr Nima Faghihi, whose support and encouragement has made this academic endeavour possible. I would like to express my appreciation to the Prof. Reza Ahmadian, Dr. Seyed Ghaffar, and Dr. Valentina Stojceska for serving on my examination panel. Their comments and suggestions greatly improved this thesis. Last but not least, I would like to thank my fellow researcher Dr Kourosh Eshraghi for his support throughout the course of my studies at Brunel University London.

Abstract

Landslide-generated waves are significant threats to coastal areas and lead to destruction and casualties in several locations worldwide. The recent Anak Krakatau subaerial landslide tsunami in December 2018, which resulted in more than 450 deaths, demonstrated the knowledge gap on this subject and motivated this study. Predictive equations are beneficial for estimating the amplitudes and periods of landslide-generated waves in a timely way and can be readily employed for preliminary hazard analysis. Accurate predictions of the amplitude and period of landslide-generated waves is challenging since large uncertainties are associated with landslide parameters. Here in this research, the performance of existing predictive equations is assessed by reproducing past tsunami events, which shows relatively large misestimations. In particular, the predictions made by existing equations were divided by a few orders of magnitude (10^{-1}-10^{4} m). Furthermore, most of these exiting equations need five or six parameters as inputs. This study is focused on developing new predictive equations for estimating the initial maximum wave amplitude and period of submarine and subaerial landslide-generated waves. A comprehensive series of physical experiments (75 tests) in a wave tank at Brunel University London, and numerical simulations (250 simulations) are conducted to provide a large database for developing the new predictive equations. The predictive equations in this study are developed based on non-dimensional parameters, which makes them applicable to real-world landslide cases. These equations require a few landslide parameters (e.g., landslide volume, water depth, and slope angle) to estimate the landslide-generated waves, which is an advantage compared to existing equations. 14 empirical equations are developed for estimating of maximum initial tsunami amplitude of solid-block submarine landslides, two equations for subaerial landslides including solid-block and granular material, one equation for predicting the wave period of subaerial landslide generated waves. This study's predictive equations successfully reproduce laboratory and field data with satisfactory performance. Waves generated by subaerial solid-block and granular landslides are compared in terms of maximum initial wave amplitudes. Results indicate that the maximum initial wave amplitudes generated by solid-block landslides are 107% larger than those generated by granular landslides in our experiments. Also, a critical angle of 60o is achieved for granular slides, and for slope angles more than this critical value, the maximum wave amplitudes start to decrease. It is believed that experimental and numerical investigation of landlside-generated waves, and predictive equations developed in this study have significantly contributed to the knowledge of landslide tsunamis.

List of peer-reviewed journal articles from this thesis

1- **Sabeti, R.,** and Heidarzadeh, M., 2020. Semi-empirical predictive equations for the initial amplitude of submarine landslide-generated waves: applications to 1994 Skagway and 1998 Papua New Guinea tsunamis. Natural Hazards, 103(1), 1591-1611. https://doi.org/10.1007/s11069-020-04050-4

2- **Sabeti, R.,** and Heidarzadeh, M., (2021). A new empirical equation for predicting the maximum initial amplitude of submarine landslide-generated waves. Landslides, 1-13. https://doi.org/10.1007/s10346-021-01747-w

3- **Sabeti, R.,** and Heidarzadeh, M., (2021). Numerical Simulations of Tsunami Wave Generation by Submarine Landslides: Validation and Sensitivity Analysis to Landslide Parameters. Journal of Waterway, Port, Coastal, and Ocean Engineering, 148(2), p.05021016. https://doi.org/10.1061/(asce)ww.1943-5460.0000694

4- **Sabeti, R.,** and Heidarzadeh, M., (2022). Numerical simulations of water waves generated by subaerial granular and solid-block landslides: Validation, comparison, and predictive equations. Ocean Eng., 266,112853. https://doi.org/10.1016/j.oceaneng.2022.112853

5- **Sabeti, R.,** and Heidarzadeh, M. (2022). A new predictive equation for estimating wave period of subaerial solid-block landslide-generated waves. Coastal Engineering Journal, 1-13. https://doi.org/10.1080/21664250.2022.2110657

6- Heidarzadeh, M., Miyazaki, H., Ishibe, T., Takagi, H., and **Sabeti, R**. (2022). Field surveys of September 2018 landslide-generated waves in the Apporo dam reservoir, Japan: combined hazard from the concurrent occurrences of a typhoon and an earthquake. Landslides, 1-14. https://doi.org/10.1007/s10346-022-01959-8

7- Heidarzadeh, M., Gusman, A. R., Ishibe, T., **Sabeti, R**., and Šepić, J. (2022). Estimating the eruption-induced water displacement source of the 15 January 2022 Tonga volcanic tsunami from tsunami spectra and numerical modelling. Ocean Engineering, 261, 112165. https://doi.org/10.1016/j.oceaneng.2022.112165

8- **Sabeti, R.,** Heidarzadeh, M., Romano A. and G., Barajas (2022). Numerical simulations of Three-Dimensional Subaerial Landslide-Generated Waves: Comparing OpenFOAM and FLOW-3D-Hydro. (In preparations).

Table of contents

List of figures

List of Tables

Nomenclature

l_s	Slide length
w_S	Slide width
T_S	Slide thickness
V	Slide volume
m_b	Slide mass
h	Water depth
d	Initial submergence depth
γ_s	Slide specific gravity
u_t	Terminal velocity
a_0	Initial acceleration
a_s	Slide acceleration
S_t	Motion of slide
s_0	The characteristic distance of landslide motion
t_0	The characteristic time of landslide motion
m_0	Displaced mass
ρ_w	Water density
ρ_s	Slide density
ρ	Fluid density
C_m	Added mass coefficient
f	Coulombic friction
C_d	Drag coefficient

θ	Slope angle in submarine landslide
α	Slope angle in subaerial landslide
$\eta_{max,n}$	Maximum negative initial wave amplitude
a_M	Maximum positive initial wave amplitude
η	Wave amplitude
λ_0	The characteristic wavelength
μ	Dispersive effects
F	Froude number
ψ	Critical incline angle
P	Pressure
ν	kinematic viscosity
g	Gravitational acceleration
C	Courant Number
Δt	Time step
Δx	Grid size
U	Flow velocity
ε	Mismatch error
y^+	Dimensionless wall distance
κ	Thickness of the boundary layer
u_T	Friction velocity
τ_w	Wall shear stress
v	Kinematic viscosity
y	Absolute distance from the wall
g	Gravitational acceleration
Δz	Drop height

δ	Dynamic bed friction angle
R	Reynolds number
v_s	Landslide impact velocity
W	Weber number
T_M	Maximum initial wave period
T	Wave period
M_s	Nondimensional mass
WG	Wave Gauge
STL	Still water level
NRMSE	Normalized Root Mean Square Error
N	Number of observations/calculations
obs	Observations (experimental/field data)
cal	Calculated values from predictive equations
$\overline{obs}$	Average of observations.
LES	Large Eddy Simulation
RNG	Renormalization Group
t_{imp}	Time that slide reaches to the water surface
t_{stop}	Time that slide reaches to end of the slope
FFT	Fast Fourier Transform
T_N	Nondimensional slide thickness
VOF	Volume of Fluid
F	Fraction of fluid function
V_N	Nondimensional slide volume
T_N	Nondimensional slide underwater travel time
t_s	Slide travel time

Declaration

I hereby declare that this thesis is my original research work. Sources of others' contributions are referenced within the text and appended in the reference. This work has not been submitted for any other degree at Brunel University London or any other university and higher education institution.

Chapter 1: Introduction

Chapter 1: Introduction

Tsunami, a Japanese word meaning “harbour wave”, is a series of water waves generated by sudden movements of water surface (Pelinovsky, 2006). Tsunamis are the most devastating natural phenomena of the modern world, occurring with frightening severity and intensity. According to statistics from the World Health Organization (WHO), more than 260,000 tsunami-related casualties have been recorded in the between 1998-2020. The recorded tsunamis which caused devastating and deadly consequences because of unexpected run-ups and flooding in shoreline motivated researchers to investigate the mechanism of wave generator, propagation and inundation of tsunami waves. Any wave is an energy carrier through the water. The difference between tsunami wave and a regular wave is how that energy is transferred, and how much energy that wave packs. Tsunami waves typically have very long periods and wavelengths. Consequently, they are barely noticeable in the deep ocean, while these waves approach the coastal region, water refraction and shoaling may amplify the waves significantly (Synolakis et al., 2002). Tsunamis can be generated by earthquakes, landslides, volcanic eruptions, or other extreme events such as asteroid impacts or underwater explosions (McFall, 2014; Heidarzadeh et al., 2020, 2022a). Throughout this research work only tsunamis generated by landslides are considered. A landslide is a movement of rock, debris or earth down an incline (Cruden, 1991). A landslide occurs when gravity overcomes the frictional forces keeping layers of earth/soil in place on a slope (United States Geological Survey: https://www.usgs.gov/). Mass flows can be categorized as high-density rock and soil movements, or low-density glacier falls and snow avalanches. Landslides with an initial position above, at and below the waterline are called subaerial, partially submerged and submarine landslides, respectively (Takabatake et al., 2022).

"The landslide tsunami process involves the landslide motion, tsunami wave generation, landslide runout, tsunami propagation and runup" (Kim, 2012). When the landslide reaches the free surface, a wave is generated and landslide energy is transferred to water. The induced waves quickly leave the generation area and prop-agate in the near field. The near field features of such an impulse wave depend upon the characteristics of the landslide source (e.g., volume, velocity, density, porosity, shape of the front, slope angle, etc.). Then the waves propagate in the far field where frequency and directional energy dispersion, refraction, reflection and diffraction occur, depending upon water body configuration and waves features. Finally, the wave reaches the water body boundaries and it runs up and floods coastal areas, often resulting in great damage and danger for human activities (Di Risio et al., 2011).

The crucial factor in promoting enormous progress in tsunami science is an incredible enhancement in tsunami measurements. Most of the coastal tide gauges working before 1992 were built to record tides, storm surges, seasonal oscillations and other low-frequency processes (cf. Pugh and Woodworth 2014). These were either analogue ‘‘pen-and-paper’’ gauges, or digital instruments with poor time resolution (with a 15–20 min time step). Such instruments were quite adequate to measure tides and other long-period processes but were inappropriate for tsunami monitoring. Specifically, the 1992 Nicaragua and Flores Island tsunamis, as well as other tsunamis of the early 1990s, advanced the reconstruction of the tide gauge network in the Pacific Ocean (e.g. Rabinovich and Stephenson 2004). However, most of the NOAA tide gauges still had insufficient time resolution (6 min), while in the Indian and Atlantic oceans, coastal tide gauges were either still analogue or had 6–15 min sampling. At that point in time, the common opinion was that there are no tsunamis in these oceans, and there was no reason to have higher resolution. Only the catastrophic 2004 Sumatra tsunami in the Indian Ocean, which was globally observed, including in far remote regions of the North Pacific and North Atlantic (e.g. Rabinovich et al. 2006; Titov et al. 2005a), initiated the total upgrade of the worldwide sea-level network. Modern digital tide gauges are high-resolution instruments with 15–60 s sampling, which is perfect for tsunami measurements. As a result, each new strong tsunami brings an enormous amount of high-quality data from several hundred instruments. These new data-enabled to investigate tsunamis with much higher accuracy than was possible before and to significantly improve the general tsunami understanding.

The scientific community has focused on tsunamis caused by submarine landslides, especially after the July 1998 tsunami that hit Papua New Guinea (PNG), with a maximum runup of 15 m and 2,100 casualties (Synolakis et al., 2002; Tappin et al., 2008; Heidarzadeh and Satake, 2015). (Figure 1.1). As a result of the tsunami caused by a submarine landslide in 1994 in Skagway, Alaska (USA), a construction worker was killed, and the harbour was damaged (Kulikov et al., 1996; Rabinovich et al., 1999). On October 16, 1979, another major tsunami was generated by a submarine landslide near the Nice (France) airport. Eleven people were swept away, and one was killed after the 2–3 m high tsunami washed over a section of the new harbour extension next to the Nice international airport (Gennesseaux et al., 1980; Sultan et al., 2004; Fine et al., 2005). The 1994 Skagway (Alaska), 1946 Unimak (Alaska) (Okal et al., 2003), Storegga (approximately 8,100 years ago) (Harbitz, 1992), 1741 Oshima-Oshima (Japan) (Satake and Kato, 2001), and 1999 Izmit bay (Turkey) (Yalciner et al., 1999) are other significant landslide events worldwide that resulted in damage and deaths (Heidarzadeh et al., 2014).

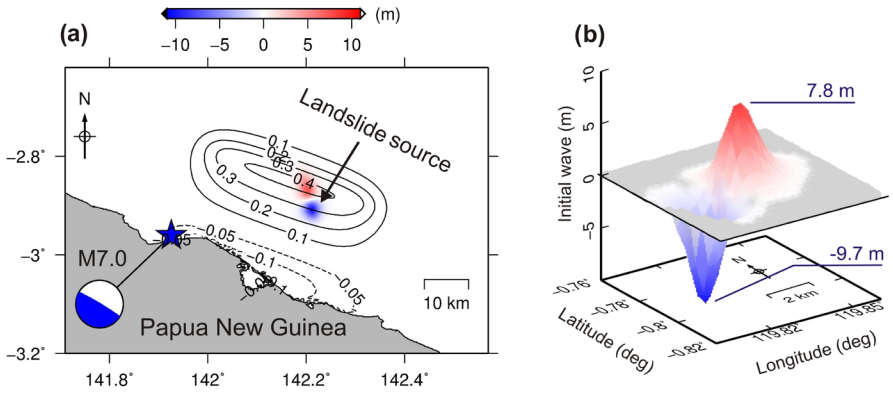

Figure 1.1 (a) The location of landslide source of the 1998 PNG tsunami based on Heidarzadeh and Satake (2015). (b) The initial waves produced by landslide tsunamis in Papua New Guinea during the 1998 tsunami.

The 1792 Unzen–Mayuyama mega slide (3.4×10^8 m^3) was the greatest subaerial landslide-generated waves disaster in the history of Japan with 15,000 fatalities (Unzen Restoration Office of the Ministry of Land, Infrastructure and Transport of Japan 2002). Mass movements due to slope failures and flank collapses have been frequently observed in volcanic areas (e.g., Moore et al. 1989; Holcomb and Searle 1991; Normark et al. 1993; McMurtry et al. 2004) and are categorized as an ordinary incident affecting oceanic volcanoes. For example, about 68 events of large debris avalanches have been detected in Hawaii, some of them with more than 200 km length and 5000 km^3 volume (Moore et al. 1994; Robinson and Eakins 2006), 47 events in Reunion Island (Oehler et al. 2004, 2007; Kelfoun et al. 2010) and 25 events in the Canary Islands (Krastel et al. 2001; Masson et al. 2002; Paris et al 2005). The recent 2018 Anak Krakatau volcanic tsunami (Indonesia) (Figure 1.2), which left a death toll of more than 450 people, once more highlighted the large tsunami hazards associated with subaerial volcanic collapses (Grilli et al., 2021; Omira and Ramalho, 2020; Muhari et al., 2019; Heidarzadeh et al., 2020). Other destructive subaerial landslides in recent decades are the 1958 Lituya Bay event, where a landslide tsunami generated the largest-ever recorded tsunami with a runup of up to 524 m (Fritz et al., 2004), and the 1963 Vajont dam incident in Northern Italy, where an impulsive landslide-generated wave overtopped the dam and caused approximately 2,000 casualties (Heller and Spinneken, 2013).

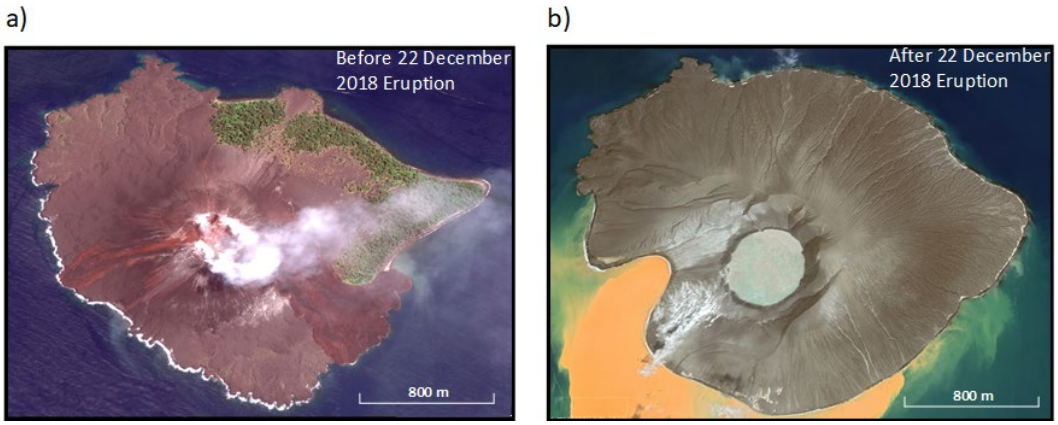

Figure 1.2. (a): Satellite image of the Anak Krakatau before the 2018 eruption. (b) Satellite image after the event. Source: Google Earth (https://earth.google.com/web/).

The accurate prediction of the maximum initial wave amplitude and maximum initial wave period of landslide around the source region are vital hazard indicators for coastal impact assessment and modelling of the propagation and inundation of landslide tsunamis (Watts et al., 2005; McFall and Fritz, 2016; Heidarzadeh et al. 2022b). The importance of these parameters is the impact of this parameter on the impulse wave which is the most potential destructive wave in case of hitting the coastal area (Watts et al., 2005). Impulse waves are commonly referred to landslide tsunamis if they occur in oceans. Impulse waves can cause disaster due to run-up along the shoreline and overtopping of dams. The wave run-up is the most threatening stage accounting for most of the fatalities. In most cases it is difficult to prevent a landslide from occurring. In some cases, it was possible to stop the creeping of active landslides with massive remedial methods. The key and also most costly example is the Clyde dam in New Zealand (Heller, 2006). The creeping of several active slides was stopped by a combination of drainage works to lower the groundwater level and large-scale mass displacements unloading the head of active frontal lobes and buttressing the toe of the lobes (Jennings et al. 1991; Heller, 2006). In addition to their threat to human communities and vital infrastructure, landslides generated tsunami also menaces installations offshore structures such as platforms, risers, FPSO, pipelines and subsea systems such as manifolds on the continental shelf and slope (Swanson and Jones, 1982; Bruschi et al., 2006).

Problem outline:

Regarding the high potential impact of landslide-generated tsunami waves on coastal region and potential causalities, a better prediction could save many lives and dramatically reduce the damage cost to at risk areas. The main reason which makes a landslide more dangerous in terms of casualties is the source location in comparison with other sources of tsunami waves. The landslides commonly occur near the shoreline. Moreover, the speed of generated waves will be 700-800 km/h approximately; hence, there would not enough time to warn the coastal communities, from one of the greatest natural hazards. Flood potential of landslide generated wave hazards is especially dangerous in restricted water bodies like lakes, dam reservoirs, bays, and fjords where their energy is trapped (Jiang and LeBlond 1992; Couston et al. 2015; Heller and Spinneken 2015). In order to provide a reliable prediction, modelling of this phenomenon through the physical experiments (by downscaling of real-world cases) and numerical simulations could apply to shed a light on the process of generation and propagation of these waves. The main reasons to employ the physical modelling are to simulate what occurs in the nature in a smaller scale, having this opportunity to measure different involved parameters in generation and propagation of these waves, and using the results of these modelling to validate the numerical models. The numerical models without the limitations of physical experiments (e.g. high cost, and long time for preparation of every experiment) could be used in large number of scenarios. The results of physical and numerical modelling in different tests create a valuable data base to be used to derived the predictive equations. These forms of equations provide a simple but accurate picture of potential generated waves which could be used by decision makers in the potential coastal regions to assess the impact of these waves on the coast. This study is provided helpful estimation for decision-makers who are responsible for coastal defence, especially in potential regions, to improve the understanding of related hazards and to decrease their destructive consequences. A key motivation for the work reported here is to improve our ability to assess and predict the amplitude of water waves generated by landslide.

This research aims to:

(i) Study the effect of different landslide parameters (i.e. water depth, slope angle, and slide volume) on the maximum initial wave amplitude, and maximum initial wave period of landslide-generated waves.

(ii) Develop new predictive equations for predicting the maximum initial wave amplitude generated by submarine and subaerial landslides along with devolving a new predictive equation for estimating the maximum initial wave period of subaerial landslides.

The objectives of this study are:

(i) Advancing the understating of the wave characteristics of landslide-generated waves through physical modelling.
(ii) Validating and applying a Computational Fluid Dynamics (CFD) package FLOW3D-Hydro to simulate landslide-generated waves. This validated landslide numerical model is applied for sensitivity analysis of maximum wave amplitudes and periods of the waves.
(iii) Generating the data, including the experimental data and artificial data (using a validated numerical model) in order to derive predictive equations.
(iv) Using genetic algorithm as an optimization technique along with considering the non-dimensional parameters for deriving accurate predictive equations with applicability to actual cases.
(v) Evaluating the performance of existing predictive equations and comparing them with new proposed equations of this study using data from actual landslide tsunami events.

Thesis outline

Chapter (2) presents background information on the landslides generated waves including subaerial and submarine landslides and critically analysis the performance of predictive equations which estimate the maximum initial wave amplitudes and periods along with details some of the historical events. Chapter (3) introduces the methods and approaches that used in physical modelling and numerical simulation of landslide generated waves along with techniques to develop the predictive equations. Chapter (4) contains results of modelling including numerical and physical models of subaerial and submarine landslides and discuss the outputs. The key findings, limitations and future study are given in Chapter (5) (conclusion).

Chapter 2: Literature review

Chapter 2: Literature review

The existing literature associated with two major sources of landside generated waves (i.e. submarine failures and subaerial failures) is analysed in this chapter. Numerous experimental, numerical, and analytical studies have been carried out to characterise the waves generated by submarine and subaerial failures, all in an effort to ensure the coastal community's safety from landslide tsunamis (Enet et al., 2007). These studies conducted over the past few decades have elucidated the mechanisms behind the generation and propagation of landslide-generated waves. Regarding the complexities associated with three-phase flows, including water, solid, and air involved in the evolution of landslide-generated waves, empirical equations (predictive equations) proved beneficial for predicting the initial maximum amplitudes and periods of the landslide's waves (Watts et al., 2005).

2.1 Submarine landslide

Regarding physical modelling, Wiegel (1955) was a pioneer in the physical modelling of water waves generated by landslides who has been inspired by many researchers after his work. Fundamentals of landslide tsunami characteristics were discovered by Wiegel (1955) as he reported that the leading wave amplitude of landslide tsunamis increases by increasing block density, by decreasing initial block submergence, and by increasing incline angle. According to Hammack (1971), the initial wave profile studied by Prins (1958) could only be produced by the very fast vertical motion of a wavemaker body over a finite vertical distance. This implies that the time scale of wave generation must be much faster than the time scale of wave propagation out of the generation region for Prins' (1958) results to be applicable to underwater landslides. Watts (1997, 1998, 2000) modelled submarine landslides with triangular blocks sliding down a ramp with an incline of 45°. The triangle prism produced a trough above the block due to the horizontal top face of the block, while the vertical front face produced a crest in front of the block. The other studies associated with the physical modelling of submarine landslides through two-dimensional solid blocks sliding down a plane slope are Najafi-Jilani and Ataie-Ashtiani (2008), Fernández-Nieto et al. (2008), Tinti and Tonini (2013), and Whittaker et al. (2015). In particular, Ataie-Ashtiani and Najafi-Jilani (2008) performed experiments in a 2.5m wide, 1.8 m deep and 25 m long wave flume using solid steel blocks with different shapes and granular material. Both the landslide width and the 15°-60° incline were narrower than the flume width. The combination of laboratory investigation and numerical method in order to introduce a new equation for predicting the amplitude of the impulsive wave at the near field has been done in this study. Sue et al. (2011) studied submarine landslides by sliding a rigid semi-ellipsoid down a 15° incline in a 14.7 m long, 0.25 m wide and 0.50

m deep basin. A smooth transition was formed between the incline and the floor of the basin. The sliding block had a major axis length of 0.5 m and a height of 0.026 m. The specific gravity of the rigid landslide was adjustable. A Particle Tracking velocimetry (PTV) technique was used to measure the landslide kinematics. Numerical simulations using a solved boundary element method based on linear, inviscid and irrotational wave theory were compared with the physical experiments.

In addition, three-dimensional experiments were also conducted by Grilli and Watts (2005), Watts et al. (2005), Enet et al., 2007 and Fujii et al. (2018). While the aforementioned researchers used soli-block to model the moving slide, Grilli et al. (2017) and Takabatake et al. (2020) applied deformable materials to model the landslide. In addition, Ataie-Ashtiani and Najafi-Jilani (2008) and Fujii et al. (2018), both of them used granular material as the sliding mass. In general, physical laboratory modelling is a straightforward way to study landslide tsunamis, and the result of experimental data can be used to validate numerical models and derive the predictive empirical equations (Watts et al., 2003; Grilli and Watts, 2005; Liu et al., 2005; Enet and Grilli, 2007; Fritz et al., 2009). Although physical models have several advantages, they also have some challenges, such as scale effects, laboratory limitations due to reflection, duration of tests, and installation and maintenance costs.

In term of analytical approach, Harbitz and Pedersen (1992) presented analytical solutions for wave excitation by submarine landslides in order to investigate the influence of governing parameters. Harbitz and Pedersen (1992) discovered an expression for the relative importance of landslide volume versus shear stress on the interface of fluid and sliding masses. Analytical solutions are typically available only for simple cases, making them incapable of accounting for more realistic landslide events (Lo and Liu, 2017).

Regarding the numerical modelling, Iwasaki (1987) investigated the water waves generated by an initially submerged rectangular block falling vertically in a constant depth channel using numerical simulations. The motion of the block began at t=0 and continued at constant velocity until the block came to rest on the channel bottom. An inviscid boundary element method code was used to simulate the generation of water waves. Heinrich (1992) used a standard Finite Difference technique to simulate the effect of water waves created by a submarine solid-block descending a sloping beach in a wave flume. The experimental results of Rzadkiewicz et al. (1997) were used to develop a numerical model using the 2D Navier Stokes model - NASAVOF2D and a 2D diffusion model to describe sediment rheology using a Bingham law. Monaghan and Kos (2000) used Smoothed Particle Hydrodynamics (SPH) to clarify wave formation and box-like landslide dynamics using a 2D numerical particle model. Liu et al. (2005) discovered that for submerged cases of the solid sliding mass, the runup decreases asymptotically as the submergence increases and approaches zero as the submergence approaches infinity. Grilli et al. (2017) used numerical simulations to investigate the effects of material rheology on the evolution of landslide tsunamis. Ruffini et al. (2019) developed a numerical model based on non-

hydrostatic shallow water equations to assess the effect of water body geometry on far-field landslide tsunami propagation. Existing numerical models for the simulation of submarine landslide tsunamis have taken advantage of diverse forms of mathematical formulations, including Boussinesq equations (Lynett and Liu, 2002; Watts et al., 2003; Fuhrman and Madsen, 2009; Zhou and Teng, 2010), shallow-water theory (Harbitz, 1992; Heidarzadeh and Mulia, 2022), fully nonlinear potential flow (Grilli and Watts, 2005), non-hydrostatic wave equations (Ma et al., 2012), and Navier-Stokes equations (Heinrich, 1992; Liu et al., 2005; Yuk et al., 2006; Abadie et al., 2010 and Montagna et al., 2011; Rabinovich et al., 1999).

2.2 Subaerial landslide

Physical experiments have been used to model impulsive waves generated by subaerial landslides, including landslide motion, effective parameters, wave characteristics, and associated runup. In this regard, Savage and Hutter (1989, 1991) models characterise avalanche and debris flow using a Coulombic friction law. Koch et al. (1994) investigated three-dimensional granular landslides on a partially curved surface. A granular material pile was released to run down a 5 m long, 3 m wide slide with an initial slope ranging from 20° to 60°. Glass beads, quartz, and marble granules were among the seven granular materials tested. Iverson (1997) measured basal fluid pressure and conducted large-scale chute experiments in an inclined flume to study momentum transfer in debris flow. A gate at the top of the flume released approximately 10 m^3 of saturated sand and gravel in the physical model. The landslides were created using quartz chips with a mean diameter of 2-4 mm on a parabolic incline with a 40° initial slope. Fritz (2002) conducted a series of physical experiments in a two-dimensional flume; the subaerial landslide-generated waves were categorised into four types (weakly nonlinear oscillatory wave, nonlinear transition wave, solitary-like wave and dissipative transient bore) based on the Froude number and slide thickness. In order to provide a better understanding of generated waves, a series of analyses were done, including classifying the waves based on the wave nonlinearity criterion, wave envelop attenuation, and impact energy conversion. Sælevik et al. (2009) studied the effect of slide volume, slide length, and slide height on the subaerial landslide-generated waves using different solid blocks in a 2D wave flume. Sælevik et al. (2009) concluded the governing parameter for the initial maximum wave amplitude is slide volume, whereas the slide height effect is relatively small. Heller and Spinneken (2012) studied the effect of three landslide parameters (slide Froude number, the relative slide thickness, and the relative slide mass) on subaerial generated waves. Bruggemann (2012) applied a larger 2D and 3D physical model than Heller and Spinneken (2012) to study the wave characteristics of subaerial landslide waves. The generated wave in the 3D model decayed much faster than in the 2D setup. The distance from the source was detected as a key factor for the wave height and wave amplitude of the generated waves. Other experimental studies have been conducted concerning subaerial

landslide-generated waves, including 2D investigations: Ataie-Ashtiani and Nik-Khah, 2008; Bullard et al., 2019; Fritz et al., 2004; Heller et al., 2008; Heller and Hager, 2010; Heller and Spinneken, 2013 and 2015; Kamphuis and Bower-ing, 1972; Miller et al., 2017; Robbe-Saule et al., 2021; Walder et al., 2003; Heidarzadeh et al., 2020), and those using three-dimensional (3D) wave basins (e.g., Bregoli et al., 2017; Heller and Spinneken, 2015; McFall and Fritz, 2016; Mohammed and Fritz, 2012; Panizzo, De Girolamo, and Petaccia, 2005; Romano et al., 2016). In terms of the landslide materials applied in physical experiments, some used a solid-block (e.g., Heller and Spinneken, 2015; Kamphuis and Bowering, 1972; Panizzo et al., 2005; Heidarzadeh et al., 2020) and others used deformable materials (e.g., Fritz et al., 2004; McFall and Fritz, 2016; Miller et al., 2017; Bullard et al., 2019; Evers and Hager, 2015; Robbe-Saule et al., 2021).

Generally, analytical solutions for the modelling of subaerial landslide-generated waves have been available for some simple idealized cases (e.g., Noda, 1970; Pelinovsky and Poplavsky, 1997; Liu et al., 2003; Haugen et al., 2005).

Accurate numerical models have the ability to model a broad range of landslide parameters that would prove extremely challenging to model physically in the laboratory. Modelers have used full Navier-Stokes AMR (Automatic Mesh Refinement) Eulerian compressible hydrodynamic code called SAGE to simulate landslide-induced tsunamis on numerous occasions, including Mader and Gittings (2002, 2003) and Gisler et al (2006). Gitting (1992) created a code for Science Applications International, Los Alamos National Laboratory, and it is best suited for compressible multi-material simulations, such as meteorite impact (Gisler et al., 2004). It solves the entire set of compressible Navier-Stokes equations, including the equation of state and various material strength constitutive models. Using a multi-fluid Navier-Stokes model. Abadie et al. (2010) presented an idealised geometry for simulating the waves generated by subaerial landslides. The viscosity of the slide was varied to investigate the effect of slide deformation on generated waves, which revealed that slide shape deformation could have a significant impact on slide motion and waveforms. To study the impact of subaerial landslides in dam reservoirs while accounting for nonlinearity and frequency dispersion, Ataie-Ashtiani and Yavari-Ramshe (2011) developed a 2D fourth-order Boussinesq-type model. For two real-world case studies, this validated model was used to estimate the maximum wave amplitudes and runup of potential subaerial landslides. Ma et al. (2015) created a model for simulating subaerial landslide motion that considers saturated granular flow and 3D non-hydrostatic wave motion (NHWAVE). By comparing the results to analytical solutions for granular dam-break flows as well as experimental data, the NHWAVE model was validated. Ruffini et al. (2019) presented a numerical model based on non-hydrostatic shallow water equations (SWASH) to quantify the effect of water body geometry on far-field landslide tsunami propagation, as well as two-dimensional numerical simulations to quantify the effect of frequency dispersion. They discovered that the dispersive process is negligible

for solitary- and cnoidal-like waves in shallow water but becomes more important for Stokes-like waves in deeper water. Lee and Huang (2021) used physical tests and numerical simulations to investigate the effect of grain size on subaerial landslide-generated waves. The simulations were carried out using a multiphase flow model based on an Eulerian framework. Physical measurements confirmed Lee and Huang's (2021) findings that finer sand materials slide faster and generate larger waves. In general, numerical modelling plays an important role these days in studying subaerial landslide tsunamis due to their flexibility and relatively low cost as compared to physical modelling (e.g., Fine et al., 2005; Lynett and Liu, 2005; Heller and Hager, 2011; Abadie et al., 2010; Heidarzadeh et al., 2019; Salmanidou et al., 2019; Heidarzadeh and Satake, 2017).

Among researchers who studied wave periods of solid-block landslide-generated waves through physical experiments are Ataie-Ashtiani and Nik-Khah (2008), Heller and Spinneken (2013), and Heller and Spinneken (2015). Ataie-Ashtiani and Nik-Khah (2008) studied the effect of slope angle, water depth, slide impact velocity, geometry, shape and deformation on impulse wave characteristics (i.e. wave amplitude and wave period) through physical experiments. They reported that slide deformation makes a maximum increase of up to 30% on wave period. Their results show the slide shape is not strongly affecting the general feature of an impulse wave and, at most periods, is changed by less than 10%. Similar to Ataie-Ashtiani and Nik-Khah (2008), Heller and Spinneken (2013) studied the effect of landslide parameters on wave period through physical experiments. They reported that the wave period mainly depends on the characteristic time of submerged landslide motion rather than its width or front shape. Heller and Spinneken (2015) compared the 2D and 3D setups in terms of the characteristics of subaerial landslide-generated waves. They showed that the wave period is, on average, 21% smaller in 3D than in 2D experiments.

2.3 Body geometry of experiments in this study:

As it was discussed in the previous subsections of this chapter, a large number of investigations on landslide-generated wave including subaerial and submarine landslides were conducted in wave flumes (Two-dimensional setup) e.g. Kamphuis & Bowering, 1972; Watts, 1998; Walder et al., 2003; Fritz et al., 2004; Ataie-Ashtiani & Nik-Khah, 2008; Bullard et al., 2019; Heller et al., 2008; Heller & Hager, 2010; Heller & Spinneken, 2013; Miller et al., 2017; Robbe-Saule et al., 2021; Takabatake et al., 2022) which emphasis on rationality and importance of 2D set up for investigation of landslide generated waves. Lange et al., 2020 stated as a result of these investigations, a significant amount of progress in understanding landslide-generated tsunamis has been accomplished due to this approach of modeling. Nonetheless, these researches were frequently conducted in 2D rather than 3D. Mohammad and Fritz (2011) reported due to the higher landslide deformation in 3D set up compared to 2D, three-dimensional landslides are less efficient wave generators than two-dimensional examples. In general, a number of considerations including, scale effect analysis, non-depersonalizing of parameters, and more importantly lateral wall effects are considered in this study to tackle the impact of 2D experiments on simulated landslide-generated waves in this study. Details of these consideration are described in third chapter of this study (Chapter 3- Data and Methods). The other proof for validity and accuracy of these experiments are shown by testing the performance of predictive equations that they developed employing databases of experiments in a two-dimensional setup of this study; in particular, wave amplitude and period of previous actual landslide tsunamis were reproduce with a high accuracy by using these equations (Table 4.3-4.6).

2.4 Selection of numerical model for this study

Mostly, models with approach of depth-integrated e.g. TWO_LAYER (Imamura and Imteaz (1995), LS3D (Ashtiani and Jilani (2007), and GLOBOUSS (Løvholt et al., 2017) have been used to simulate landslide tsunamis. The assumptions of depth-integrated models fit well with tsunami propagation and, in some situations such as submarine landslides could be apply in generation stage as well (Rauter, 2021). However, considering complexities associated with three-phase flows, including water, solid, and air involved in the evolution of subaerial landslide-generated waves (e.g., 1963 Vajont landslide or 2018 Anak Krakatau tsunamis) contradicts the assumptions of depth-integrated and prospective flow models. Numerical models that are based on solving the Navier-Stokes equations are showed a very well capability and reliability to simulate landslide generated waves, although a wide range of alternative and mixed methods was proposed such as smoothed particle hydrodynamics (e.g. Pastor et al., 2008), particle finite element method (e.g. Mulligan et al., 2020) are a few of the promising approaches. The other powerful framework is IHFOAM Solver (based on OpenFOAM) which solves the solve two-phase flow within porous media by means of the Volume-Averaged Reynolds-averaged Navier-Stokes equations and benefits from turbulent models such as k-omega (k- ω) and k-epsilon (k- ε). Among these models FLOW-3D Hydro offers a CFD package which solves Navier-Stokes equations using a finite-difference and finite volume approximation, along with Volume of Fluid method (VOF) for tracking the free surface have already been tested and showed a better performance to simulate the landslide generated waves (Montagna et al., 2011; Yin et al., 2015). Also, this CFD software offers different turbulent models such as Large Eddy Simulation – LES, k-ε, k- ω model and Renormalization Group – RNG which provide more flexibilities for users.

2.5 Predictive equations

If time is of the essence, predictive equations can be used to make educated guesses about the amplitudes or periods of landslide-generated waves, allowing for more accurate preliminary analysis (Watts et al., 2005). Although it is difficult to measure the maximum initial amplitude or period of landslide waves near the source region due to a lack of wave gauges, this information is available for some landslide events through experimental and numerical studies.

In following the proposed predictive equations are separated in terms of moving slides (granular or solid-block) and type of landslide (subaerial landslide or submarine landslide). Several researchers have proposed predictive equations for estimation of the maximum initial wave amplitude of landslide tsunamis, including the equations associated with submarine landslides, following studies were considered the solid block as the moving slide (Wiegel, 1955; Iwasaki, 1982; Heinrich, 1992; Harbitz and Pedersen, 1992; Watts, 1998; Murty, 2003; Grilli and Watts, 2005; Najafi-Jilani and Ataie-Ashtiani, 2008; Fernández-Nieto et al., 2008; Tinti and Tonini, 2013; Grilli et al., 2017; Fujii et al., 2018; Takabatake et al., 2020), subaerial granular landslides (Slingerland and Voight,1982; Fritz et al., 2004; Zweifel et al., 2006; Heller and Hagger, 2014; Robbe et al., 2021), and subaerial solid-block landslides (Noda, 1970; Bolin et al., 2014; Robbe et al., 2021). A number of predictive equations for the estimation of the maximum initial wave period for granular landslides were proposed by the following researchers: Fritz (2002), Mohammad and Fritz (2012), Heller and Hager (2014), Mcfall and Fritz (2016), and Xue et al. (2019). However, only a limited number of researchers proposed predictive equations for estimating the maximum initial wave period for solid-block landslides, including Ataie-Ashtiani and Nik-Khah (2008), Heller and Spinneken (2013), and Heller and Spinneken (2015).

It is essential to examine how accurately these equations can reproduce actual landslide events. In the following, the performance of the existing predictive equations is examined by reproducing the real-world case studies. It should be emphasised that the usefulness of predictive equations is dependent on the quality of the parameters on which they are based. In order to evaluate the performance of submarine solid-block landslides, two case studies (Skagway, 1994; Papua New Guinea, 1998) were applied to existing equations (Table 2.1 and Table 2.2). The 1994 Skagway, Alaska landslide tsunami event (Table 2.1) destroyed 300 m of the railway and claimed the life of one construction worker.

Table 2.1 Predictions made by existing equations for the maximum negative initial landslide wave amplitudes ($\eta_{max,n}$) of the 1994 Skagway event.

Author	Equation[a]	landslide parameters	Calculated value (m)	Observed value (m)
	$\eta_{max,n} = \frac{\tau t_r}{2\rho C_0}$	N/A	N/A	1.0−2.1
Harbitz and Pedersen (1992)	$\eta_{max,n} = \frac{\tau B}{2\rho {C_0}^2 \lvert 1 - F_r \rvert}$	B = 350 m w = 360 m γ_s = 1.80 T = 15 m θ = 17.5 (°)	3.5	1.0−2.1
Watts (1998)	$\eta_{max,n} = \frac{0.33 S_0}{(\frac{u_t \sqrt{gd}}{a_0 B})^{2.01}}$	B = 350 m d = 88 m γ_s = 1.80 θ = 17.5 (°)	19.4	1.0−2.1
Grilli et al. (2002)[b]	$\eta_{max,n} = 0.217 + \left(3.83\frac{w}{B}\right) - 0.632(\frac{w}{B})^2$	B = 350 m w = 360 m	3.1	1.0−2.1
Murty (2003)	$\eta_{max,n} = 0.3945V$	B = 350 m w = 360 m T = 15 m	0.8	1.0−2.1
Watts et al. (2003)	$\eta_{max,n} = 0.2193T(1 - 0.754\sin\theta + 0.1704\sin^2_\theta)(\frac{B\sin^2_\theta}{d})$	B = 350 m d = 88 m T = 15 m θ = 17.5 (°)	1.6	1.0−2.1
Watts et al. (2005)	$\eta_{max,n} = S_0(0.05741 - 0.0431\sin\theta) + (\frac{T}{B})(\frac{B\sin\theta}{d})^{1.25}$	B = 350 m d = 88 m γ_s = 1.80 T = 15 m θ = 17.5 (°)	1.3	1.0−2.1
Jilani and Ashtiani (2007)	$\eta_{max,n} = S_0 f_1(\frac{T}{B}, \theta)(\frac{d}{B})^{f_2(\frac{T}{B}\theta)}$	B = 350 m d = 88 m γ_s = 1.80 T = 15 m θ = 17.5 (°)	2.9	1.0−2.1

a: η_{max} is wave zero-to-trough (or zero-to-crest) amplitude, B and w are the slide length and width; d is the initial slide submergence; V is the volume of slide (for Murty, 2003 equation, the input value for V must be in 10^6 m^3); θ is the angle of the slope; γ_w is the specific gravity of water; τ is shear stress; t_0 is the characteristic time of landslide motion; C_0 is the wave speed; u_t is terminal velocity; a_0 is the initial acceleration; S_0 is initial distance of landside acceleration; $d_{ref} = B\sin\theta$ is reference thickness; X_f is the shifted distance of two families of free waves; t_r is running time of slide and F_r is Froude number; f_1 and f_2 are functions of T, B and θ (see Equations 4-6 in Jilani and Ashtiani, 2007) [b]: In this dimensionless equation, all values for η, w and B should be in meters.

The second case study is the 1998 Papua New Guinea tsunami, which was caused by a moderate earthquake (M_W=7) that triggered a destructive landslide tsunami (Figure 1a; Table 2.2). The landslide-generated waves destroyed three villages and killed more than 2,100 people (Tappin et al., 1998; Heinrich et al., 2001; Synolakis et al., 2002).

Table 2.2 Predictions made by existing equations for the maximum negative initial landslide wave amplitudes $\eta_{max,n}$ of the 1998 Papua New Guinea event.

Author	Equation[a]	Landslide parameters	Calculated value (m)	Observed value (m)
Harbitz and Pedersen (1992)	$\eta_{max,n} = \frac{\tau t_r}{2\rho C_0}$	N/A	N/A	11−16
	$\eta_{max,n} = \frac{\tau B}{2\rho {C_0}^2 \lvert 1 - F_r \rvert}$	B = 4500 m w = 500 m γ_s = 2.15 T = 760 m θ = 8.0 (°)	42.7	11−16
Watts (1998)	$\eta_{max,n} = \frac{0.33 S_0}{(\frac{u_t \sqrt{gd}}{a_0 B})^{2.01}}$	B = 4500 m d = 1500 m γ_s = 2.15 θ = 8.0 (°)	222.5	11−16
Grilli et al. (2002)[b]	$\eta_{max,n} = 0.217 + \left(3.83\frac{w}{B}\right) - 0.632(\frac{w}{B})^2$	B = 4500 m w = 500 m	3.7	11−16
Murty (2003)	$\eta_{max,n} = 0.3945V$	B = 4500 m w = 500 m T = 760 m	6746.0	11−16
Watts et al. (2003)	$\eta_{max,n} = 0.2193T(1 - 0.754\sin\theta + 0.1704\sin^2_\theta)(\frac{B\sin^2_\theta}{d})$	B = 4500 m d = 88 m T = 760 m θ = 8.0 (°)	8.7	11−16
Watts et al. (2005)	$\eta_{max,n} = S_0(0.05741 - 0.0431\sin\theta) + (\frac{T}{B})(\frac{B\sin\theta}{d})^{1.25}$	B = 4500 m d = 88 m γ_s = 2.15 T = 760 m θ = 8.0 (°)	59.7	11−16
Jilani and Ashtiani (2007)	$\eta_{max,n} = S_0 f_1(\frac{T}{B}, \theta)(\frac{d}{B})^{f_2(\frac{T}{B},\theta)}$	B = 4500 m d = 88 m γ_s = 2.15 T = 760 m θ = 8.0 (°)	567.8	11−16

a: η_{max} is wave zero-to-trough (or zero-to-crest) amplitude, B and w are the slide length and width; d is the initial slide submergence; V is the volume of slide (for Murty, 2003 equation, the input value for V must be in 10^6 m^3); θ is the angle of the slope; γ_w is the specific gravity of water; τ is shear stress; t_0 is the characteristic time of landslide motion; C_0 is the wave speed; u_t is terminal velocity; a_0 is the initial acceleration; S_0 is initial distance of landside acceleration; $d_{ref} = B\sin\theta$ is reference thickness;

X_f is the shifted distance of two families of free waves; t_r is running time of slide and F_r is Froude number; f_1 and f_2 are functions of T, B and θ (see Equations 4-6 in Jilani and Ashtiani, 2007) [b]: In this dimensionless equation, all values for η, w and B should be in meters.

In summary, the two benchmark tests (Tables 2.1 and 2.2) show that the estimates of initial landslide waves produced by various equations differ by several orders of magnitude. Predictions for the smaller event (1994 Skagway) appear to be more accurate than predictions for the larger event (1998 PNG). For both case studies, the Watts et al. (2003) equation performs better in predicting the maximum initial wave amplitudes. However, the Watts et al.'s (2003) equation requires several initial landslide parameters, which may make using this equation for events with limited information difficult. Some models, such as Murty (2003), perform well in predicting the 1994 event but fail for the 1998 PNG event (Table 2.1 and 2.2). This could be attributed to the physics of submarine landslide failures, as well as the limitations of the existing equations.

Similar to the aforementioned analyses, the actual real-world subaerial landslide tsunami events, such as the 2018 Anak Krakatau (solid-block slide), the 1792 Unzen (granular slide), and the 1958 Lituya Bay (granular slide) incidents (Table 2.3) were used to evaluate the performance of existing equations (Table 2.4).

Table 2.3. The landslide parameters and observed maximum positive initial wave amplitude associated with three subaerial landslide tsunamis (1958, Lituya Bay; 1792, Unzen; 2018, Anak Krakatau).

Event	Landslide type	V (m^3)	h (m)	s (m)	θ(°)	Observed a_M (m)
Lituya Bay (1958) ***	Granular	3.06×10^7	122	120	45	152 ***
Unzen (1792) **	Granular	30.4×10^7	2900	400	10	10 **
Anak Krakatau (2018) *	Solid-block	2.11×10^7	50	114	45	134 *

* Heidarzadeh et al. (2020), Grilli et al. (2019) and Grilli et al. (2021)

** Yavari-Ramshe and Ataie-Ashtiani (2016), Wang et al., (2019), and Miyamoto (2010)

*** Fritz et al. (2004)

For the granular slide of the 1958 Lituya Bay with an observed amplitude of 152 m, the equations in Table 2.4 yield predictions in the range of 129 – 515 m (error ranges of 5 – 238 %). The two best results are achieved using the equations of Fritz et al. (2004), and that of Heller and Hager (2014). From the viewpoint of applicability of the predictive equations, the ones with fewer parameters are desired since limited information are available on the landslide parameters, in general. The predictions for the solid-block event of 2018 Anak Krakatau (observed amplitude of 134 m) lie in the range of 125 – 209

m, implying an error domain of 6 – 56 % (Table 2.4). The two equations with the best results are the relationship by Bolin et al. (2014). For the event of Unzen (1792) with a reported wave amplitude of 10 m, the prediction made equations is in the range of 50 – 1,670 m (Table 2.4).

Table 2.4. Performance of the existing predictive equations for reproducing the wave amplitudes of three subaerial landslide events (1958, Lituya Bay; 1792, Unzen; 2018, Anak Krakatau).

Type	Predictive equations*	Author (year)	Observed a_M (m)	Calculated a_M (m)	Error, ε (%)
Granular landslide (1958 Lituya Bay)	$\frac{a_M}{h} = 10^{[-1.25+0.71\log(0.5\frac{\rho_s V v_s^2}{\rho_w h^3 g h})]}$	Slingerland and Voight (1982)	152	329	116
	$\frac{a_M}{h} = 0.25\left(\frac{v_s}{\sqrt{gh}}\right)^{1.4}\left(\frac{s}{h}\right)^{0.8}$	Fritz et al. (2004)	152	155	2
	$\frac{a_M}{h} = 0.44\,[\frac{v_s}{\sqrt{gh}}\left(\frac{s}{h}\right)^{0.5} m_s/(\rho_w b_s h^2)^{0.25}(\cos 0.85\,\alpha)^{0.5}]^{0.8}$	Heller and Hagger (2014)	152	213	40
	$\frac{a_M}{h} = 0.25(\frac{V_{im}^F}{b_s h^2})^{0.8}$	Robbe et al. (2021)	152	129	15
Granular landslide (1792 Unzen)	$\frac{a_M}{h} = 10^{[-1.25+0.71\log(0.5\frac{\rho_s V v_s^2}{\rho_w h^3 g h})]}$	Slingerland and Voight (1982)	10	130	1200
	$\frac{a_M}{h} = 0.25\left(\frac{v_s}{\sqrt{gh}}\right)^{1.4}\left(\frac{s}{h}\right)^{0.8}$	Fritz et al. (2004)	10	71	610
	$\frac{a_M}{h} = 0.44\,[\frac{v_s}{\sqrt{gh}}\left(\frac{s}{h}\right)^{0.5} m_s/(\rho_w b_s h^2)^{0.25}(\cos 0.85\,\alpha)^{0.5}]^{0.8}$	Heller and Hagger (2014)	10	177	1670
	$\frac{a_M}{h} = 0.25(\frac{V_{im}^F}{b_s h^2})^{0.8}$	Robbe et al. (2021)	10	15	50
Solid-block landslide (2018 Anak Krakatau)	$\frac{a_M}{h} = 1.32(\frac{v_s}{\sqrt{gh}})$	Noda (1970)	134	209	56
	$\frac{a_M}{h} = 0.667\left(0.5\,(\frac{v_s}{\sqrt{gh}})^2\right)^{0.334}\left(\frac{b_s}{s}\right)^{0.754}\left(\frac{l_s}{s}\right)^{0.506}\left(\frac{s}{h}\right)^{1.631}$	Bolin et al. (2014)	134	118	12
	$\frac{a_M}{h} = 0.25(\frac{V_{im}^F}{b_s h^2})^{0.8}$	Robbe et al. (2021)	134	31	124

*: Parameters are a_M, initial maximum wave amplitude; h, water depth; ρ_s, slide density; ρ_w, water density; v_s, slide velocity; V, slide volume; b_s, slide width; l_s, slide length; s, slide thickness; α, slope angle; m_s, slide mass; and, V_{im}^F, the volume of the final immersed deposit. We considered $V_{im}^F = V$ for both types of landslides. Landslide parameters of Lituya Bay (1958) tsunami are based on Fritz et al. (2004): v_s=110 m/s; ρ_s= 2700 kg/m^3; ρ_w=1000 kg/m^3; and landslide width (b_s=338 m). Landslide parameters of Anak Krakatau (2018) event are based on Heidarzadeh et al. (2020): v_s=44.9m/s; ρ_s= 2300 kg/m^3; ρ_w=1000 kg/m^3; l_s=1250 m; and b_s=2700 m according to Grilli et al. (2019) and Grilli et al. (2021). The equation of Bolin et al. (2014) is based on the reformatted one reported by Lindstrøm (2016). Landslide parameters of Unzen Japan (1792) tsunami are based on Yavari-Ramshe and Ataie-Ashtiani (2016), Wang et al., (2019), and Miyamoto (2010): ρ_s= 2650 kg/m^3; v_s=100 m/s; b_s=4800 m.

In terms of evaluating the performance of predictive equations for estimating the maximum initial wave period of solid-block subaerial landslides, here three predictive equations proposed by Ataie-Ashtiani and Nik-Khah (2008), Heller and Spinneken (2013) and Heller and Spinneken (2015) in Table (2.5) were tested by reproducing of 2018 Anak Krakatau event.

Table 2.5. Comparison of the performance of existing equations for the prediction of the dominant period of the 2018 Anak Krakatau subaerial landslide tsunami. Parameters are: T_M, dominant tsunami period; V, landslide volume; h, water depth; and F, Froude number. The parameters of the 2018 Anak Krakatau event are based on the average values reported by Heidarzadeh et al. (2020), and Grilli et al. (2021).

Author(s)	Predictive equation*	V (m^3)	h (m)	s (m)	F	Observed T_M (s) **	Predicted T_M (s)
Ataie-Ashtiani and Nik-Khah (2008)	$\frac{T_M}{\sqrt{h/g}} = [4.14 + 3.88(V_1F^2)^2](\frac{T_{s1}}{V_1})^{-0.114}(\frac{l_s}{s})^{0.1}(\frac{r}{h})^{0.16}$	250×10^6	100–200	100–250	1.0–1.40	378–534	355-22,895
Heller and Spinneken (2013)	$\frac{T_M}{\sqrt{h/g}} = \frac{19}{2}\left[F(\frac{s}{h})^{0.5}\left(\frac{m_s}{\rho_w w h^2}\right)^{0.25}\left(\cos\frac{6}{7}\alpha\right)^{0.5}{T_{s2}}^{0.5}\right]^{1/4}$	250×10^6	100–200	100–250	1.0–1.40	378–534	33-35
Heller and Spinneken (2015)	$\frac{T_M}{\sqrt{h/g}} = 5.5(\frac{m_s}{\rho_w w h^2})^{0.05}(\frac{r}{h})^{0.36}$	250×10^6	100–200	100–250	1.0–1.40	378–534	34-35

*: $T_{s1} = 0.43\,V_1^{-0.27}F^{-0.66}(\sin\alpha)^{1.32}$, the dimensionless slide underwater travel time, where V_1 is nondimensional slide volume defined as $V_1 = \frac{V}{wh^2}$, here w is slide width and V is slide volume; $T_{s2} = \frac{t_s}{[h+V/(s\,w)]/v_s}$, here t_s is characterise time of submerged landslide motion, $t_s = (\frac{h}{\tan\alpha})/v_s$ for cases with no transition; r (= 400 m) , distance from the impact point; w (=2000 m), slide width; s, slide thickness; l_s (=1000 m), slide length; m_s, slide mass (=6.25×10^{11}kg); ρ_w (=1000 kg/m^3), water density; α , slope angle; v_s(=44.9 m/s), slide velocity.

**: Based on Heidarzadeh et al. (2020).

The equations proposed by Ashtiani and Nik-Khah (2008), Heller and Spinneken (2013), and Heller and Spinneken (2015) result in wave periods in the range of (390 s – 24,600 s), (40 s – 52 s), and (34 s – 35 s), respectively (Table 2.5).

Chapter 3: Data and Methods

Chapter 3: Data and Methods

An overview of the physical model and instrumentation, along with numerical simulation techniques deployed, are provided in this chapter. Physical experiments on tsunamis generated by submarine, and subaerial landslides, including solid-block and granular slides, were performed at the hydraulic laboratory at Brunel University London. In terms of numerical simulations, the Computational Fluid Dynamics (CFD) package FLOW3D-Hydro (version 1.0, update 1) was applied to simulate waves generated by submarine and subaerial landslides. Widely, the format of designing the experimenters in this field (modelling of landslide-generated waves) were inspired of what occurs in the nature, in this regard, there is a slope with different angles which represent of a large natural elevation of the earth's surface (e.g. a hill); there is a water tank which represent a body of water (e.g. ocean); and there is a slide (i.e. solid-block or granular) which represent a landslide (the movement of a mass of rock, debris, or earth down a slope).

3.1: Physical modelling of submarine landslide (wave amplitude)

A series of physical tests were performed in a 0.26 m wide, 0.50 m deep and 4.0 m long wave tank at Brunel University London. The submarine slide was considered as a moving rigid body along a straight incline (Figure 3.1) with the centre of mass motion (S_t) parallel to the incline and subject to external forces from added mass, drag force, gravity and dissipation. Therefore, the following relationships were applied for estimating the terminal velocity (u_t), initial acceleration (a_0) and motion of slide (S_t) (Watts, 2000):

$$a_0 = \frac{(m_b - m_0)g(\sin\theta - f\cos\theta)}{m_b + C_m m_0} \tag{3.1}$$

$$u_t = \sqrt{\frac{2(m_b - m_0)g(\sin\theta - C_n\cos\theta)}{C_d\,\rho_w\,w_s\,l_s\sin\theta}} \tag{3.2}$$

$$S_t = S_0\left[\ln\cos\left(\frac{t}{t_0}\right)\right] \tag{3.3}$$

where m_b is the solid mass, w_s is the width of the slide, l_s is the length of the slide, m_0 is the displaced mass of water which can be obtained from the water density (ρ_w) , the solid-block volume (V) through the following equation: $m_0 = \rho_w V$, C_m is the added mass coefficient, f is the Coulombic friction which

is influenced by the solid block and incline materials, C_d is the drag coefficient depending on the solid block shape, and S_t approximates centre of mass motion along the slope over time. The characteristic distance (s_0) and characteristic time (t_0) of landslide motion are derived directly from the equation of solid block motion (Eq. 3.3) as $s_0 = \frac{{u_t}^2}{a_0}$ and $t_0 = \frac{u_t}{a_0}$.

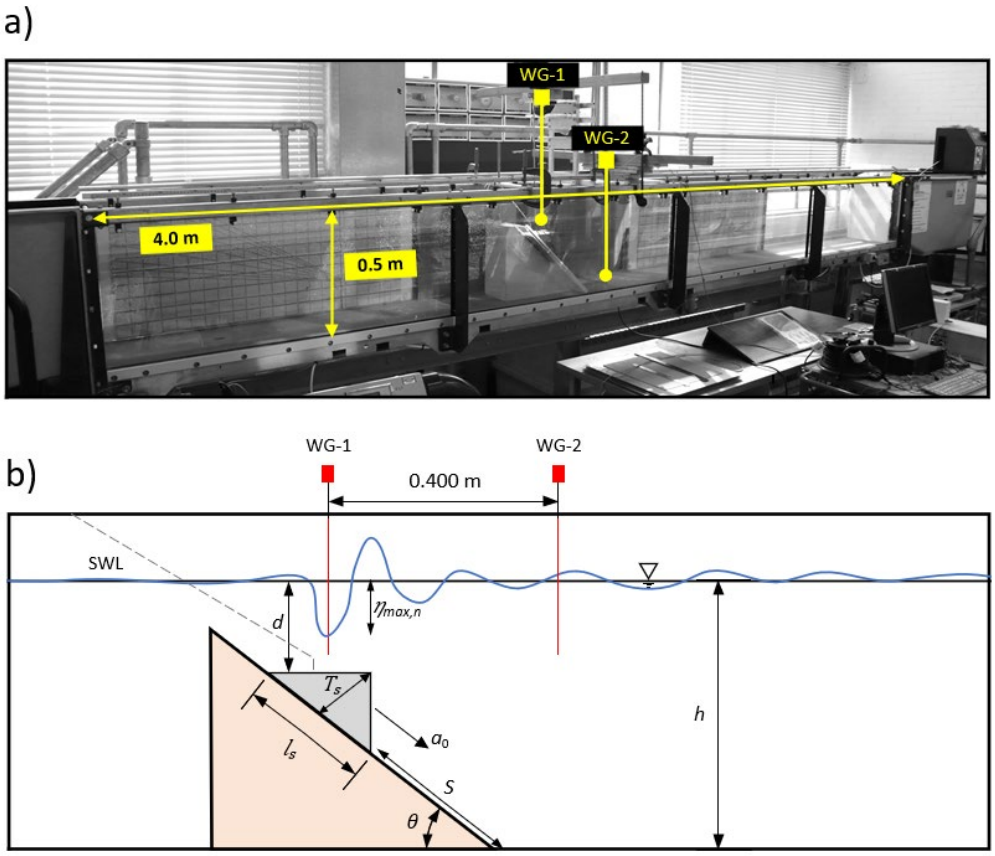

Figure 3.1. (a) Setup of physical experiments in the wave flume, a sliding mass, and two wave gauges (WG-1, WG-2) are shown. WG is abbreviation of Wave Gauge. (b) Diagram illustrating the landslide parameters: $\eta_{max,n}$, maximum negative initial wave amplitude; h, water depth; d, initial submergence depth; l_s, slide length, a_0, initial acceleration; T_S, slide thickness; θ, slope angle; S, travel distance.

To determine the kinematic coefficients (f, C_d, C_m), the Eqs. (3.1) and (3.2) were used. In particular, for determining the Coulombic friction coefficient ($f = \tan\psi$), first, we measured the critical incline angle (ψ) by increasing the slope angle in the laboratory until the block started to slide. The test was repeated three times for each solid block, and the average value of ψ was taken. Measurements of the terminal velocity (u_t) and initial acceleration (a_0) were done by using an accelerometer (model: 3-Axis Vibration/Acceleration Data Logger OM-VIB-101;

https://www.omega.co.uk/.com). The results were then applied to Eqs. (3.1) and (3.2) in order to calculate C_d and C_m. For every solid block, the measurements of velocity and acceleration were repeated three times, and the average values were taken. Based on the measurements, the mean drag coefficient of $C_d \cong 1.32$ and $C_m \cong 0.84$ were obtained.

The characteristic tsunami wavelength (λ_0) is given by the following equation (Watts, 1998; Grilli and Watts, 2005):

$$\lambda_0 = t_o\sqrt{gd} \tag{3.4}$$

where g is the gravitational acceleration, and d is the initial submergence depth. To cope with the downscaling effect of real events into laboratory size, Froude similarity has been applied in this study. The Froude similarity may work best for situations where the friction effects are negligible. The reason for this is the impact of higher values of friction on maximum slide velocity reached during the submarine slide motion (u_t). For submarine landslides, dispersive effects can be expressed by the relative depth parameter, $\mu = d/\lambda_0$ (Table 3.1). The values of μ higher than ~0.5 indicate fully dispersive deep-water waves, whereas a value of less than ~ 0.05 shows nondispersive long waves (Dean and Dalrymple, 1991). The Froude number (F) is a measure of the terminal landslide velocity (u_t) relative to the speed of a shallow-water wave in water depth (h). In general, for experimental studies of submarine slides, F was defined with the maximum slide velocity reached during the submarine slide motion (u_t) (Watts, 1997):

$$F = \frac{u_t}{\sqrt{gh}} \tag{3.5}$$

Tsunamis generated by submarine landslides in the real world are typically in the range of $F_r < 1$ (McFall and Fritz, 2016).

Table 3.1. Landslide motion characteristics measured during this study's experiments for the 45-degree slope (θ) and three different solid-blocks.

Solid block*	a_0 (m^2/s)	u_t (m/s)	S_0 (m)	t_0 (s)	d (m)	λ_0 (m)	C_m	C_d	f	μ
Solid-block-2	1.315	0.501	0.189	0.379	0.080	0.335	1.16	1.55	0.53	0.238
Solid-block-3	1.765	0.698	0.276	0.395	0.080	0.349	0.79	1.22	0.46	0.228
Solid-block-4	2.063	0.874	0.370	0.425	0.080	0.376	0.57	1.21	0.41	0.212

* Parameters are: a_0, initial acceleration (m^2/s); u_t, terminal velocity (m/s); S_0, characteristic distance of landslide motion (m); t_0, characteristic time of landslide motion (s); d, initial submergence depth (m); λ_0, wavelength (m); C_m, added mass coefficient; C_d, drag coefficient; f, Coulombic friction coefficient; μ, dispersive effect.

Figure 3.2 shows some of the existing landslide laboratory data. In Figure 3.2, Watts (1997) is abbreviated as WTS-97, Enet and Grilli (2007) is abbreviated as ENT-07, and Najafi-Jilani and Ataie-Ashtiani (2008) is abbreviated as JIL-08. WTS-97 only used triangular prisms in their experiments, whereas ENT-07 used elliptic blocks. JIL-08 modelled submarine landslides using a variety of geometrical shapes (square, triangle, and circle). Due to gaps in existing experimental data seen in Figure 3.2, some additional experiments were required to provide a sufficient dataset for deriving new predictive equations. While the data distribution over submergence depth appears to be satisfactory (Figure 3.2a), other parameters such as slide volume (Figure 3.2b) and slope angle have significant data gaps (Figure 3.2c). Although the data range for θ in existing literature varies from 15° to 60°, it covers only four values of 15°, 30°, 45° and 60° with limited data points for each angle. Accordingly, for producing data of V and θ by three different slide volumes (from 1×10^{-12} km^3 to 3×10^{-12} km^3) (Table 3.2) and five slope angles ($\theta = 20°, 30°, 38°, 45°$ and 50^0) were considered. The three values for V and three values for θ in the experiments are new as compared to existing data. Two values of θ, however, have been available from past experiments. The reason for using these values of θ was to produce a range of values for θ enabling us to establish a relationship between θ and $\eta_{max,n}$. As seen in Figure 3.2, the existing data indicate an inverse correlation between d and $\eta_{max,n}$ (Figure 3.2a) and a direct relationship between V and $\eta_{max,n}$ (Figure 3.2b). The relationship between V and $\eta_{max,n}$ can be seen by looking at a particular dataset (for example white-open circles) at a time (Figure 3.2b). Regarding θ, the new experimental data (open circles in Figure 3.2c) give a direct relationship between θ and $\eta_{max,n}$. It should point out that in Figure 3.2 for each analysis e.g. slope angle (θ) (Figure 3.2c), the other parameters such as slide volume and initial water depth were varied that's why we can observe a number of datapoints in columns in Figure 3.2a, 3.2b and 3.2c.

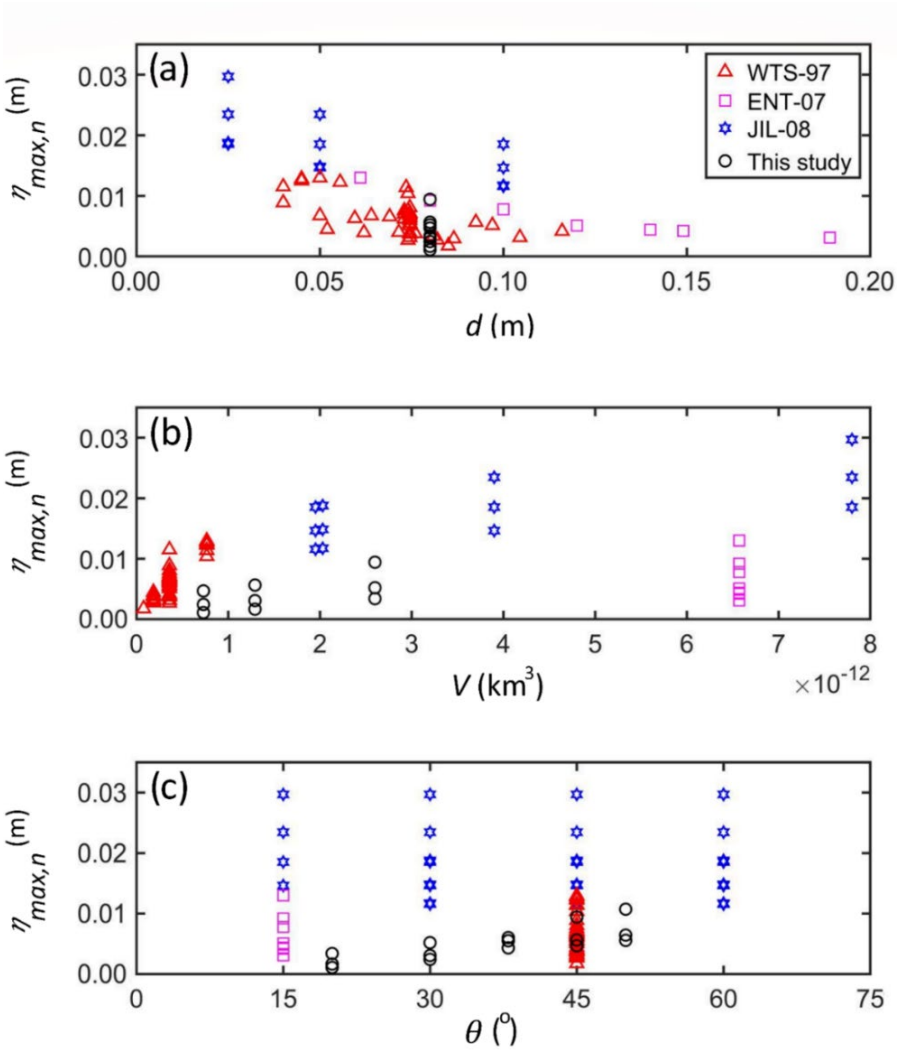

Figure 3.2. Available experimental data from literature relating the maximum negative initial wave amplitude ($\eta_{max,n}$) to (a) the initial submergence depth, d, (b) the sliding mass volume, V, and (c) the slope angle (θ). Abbreviations: ENT-07, Enet and Grilli (2007); WTS-97, Watts (1997); JIL-08, Najafi-Jilani and Ataie-Ashtiani (2008).

The experimental set-up included five different inclined planes (i.e. 20^o, 30^o, 38^o, 45^o and 50^o). The solid blocks had three different volumes (Table 3.2; 2.600×10^{-12} km^3, 1.292×10^{-12} km^3, and 0.7303×10^{-12} km^3). Other specifications of the solid blocks are given in Table 3.2. A hook was used on the solid block and a rope to move the solid block in position prior to release. The initial submergence (d) and water depth (h) in the tank were adjusted to constant values of d= 0.08 $\pm$ 0.005 m and h= 0.375 m as it was aimed to producing more laboratory data for the set-up previously used by Watts (1997). Overall, 15 were the number of conducted physical experiments by varying slope angles and slide volumes (Table 3.2) whose resulting waveforms are shown in Figures 3.3 and 3.4.

Table 3.2. Characteristics of the three solid concrete blocks used for submarine landslide experiments.

Solid block*	l_s (m)	w_s (m)	T_s (m)	V (km^3)	m_b (kg)	m_0 (kg)	γ_s
Solid-block-1	0.080	0.260	0.040	0.416×10^{-12}	1.065	0.416	2.60
Solid-block-2	0.106	0.260	0.053	0.730×10^{-12}	1.900	0.730	2.60
Solid-block-3	0.141	0.260	0.071	1.292×10^{-12}	3.355	1.292	2.60
Solid-block-4	0.200	0.260	0.100	2.600×10^{-12}	6.760	2.600	2.60

* Parameters are: l_s, slide length (m); w_s, slide width (m); T_s, slide thickness (m); V, slide volume (km^3); m_b, solid block mass (kg); m_0 the displaced mass of water (kg) and γ_s, slide specific gravity.

The generated waves were measured using two precision capacitance wave gauges (twin wire wave probe; HRIA-1016: http://equipit.hrwallingford.com/products/wave-gauges): one located at the top of the submerged slides and the other at a distance of 0.40 m from the first gauge (Figure 3.1a). Only the gauge located on the top of the mass is used in the present study, the reason for using only one wave gauge on top of the landslide is the study is focused on initial maximum wave amplitude of generated wave which occurs in the near field, the second wave gauge is only applied for validation of the numerical model in case of submarine landslide (Chapter 3.2). The gauge recordings were collected through an acquisition system at 50 Hz with an accuracy of ± 0.1 mm. The waveforms resulted from this study experiments are sorted into five groups based on the slope angles (Figures 3.3 and 3.4). Figures 3.3 and 3.4 demonstrate that by increasing the slope angle (θ) and slide volume (V), the maximum initial amplitude ($\eta_{max,n}$) increases. Increasing the initial submergence depth (d) causes a decrease in $\eta_{max,n}$. Therefore, the highest $\eta_{max,n}$ is generated by the largest concrete prism over the 50^o slope (Figure 3.4a, red).

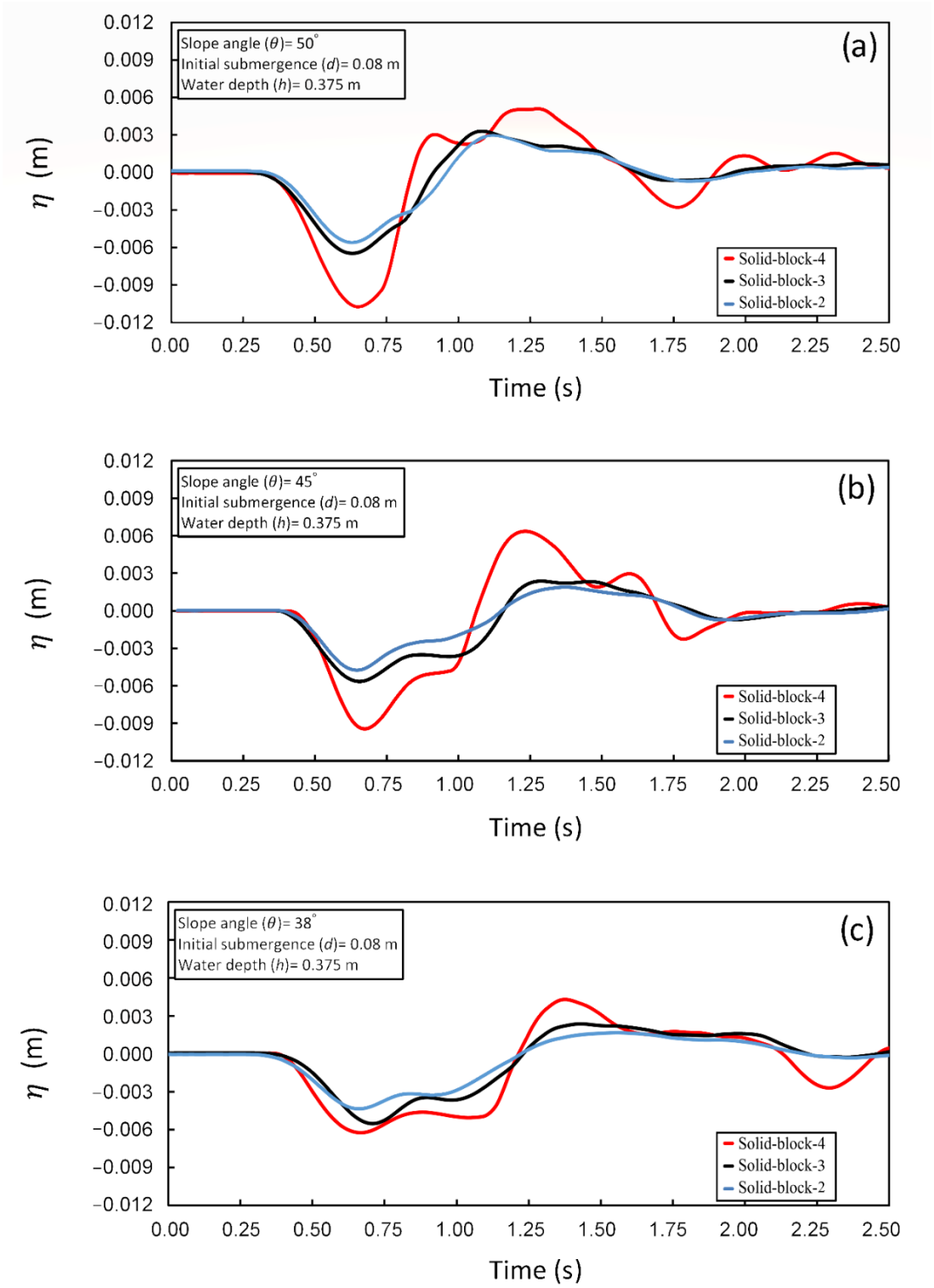

Figure 3.3. Laboratory recordings of the waves generated by a landslide at WG-1 (location of WG-1 is shown in Figure 3.2) for cases of slopes (a) $\theta = 50^{o}$, (b) 45^{o}, and (c) 38^{o}. In the panel legends, each experiment's parameters are specified.

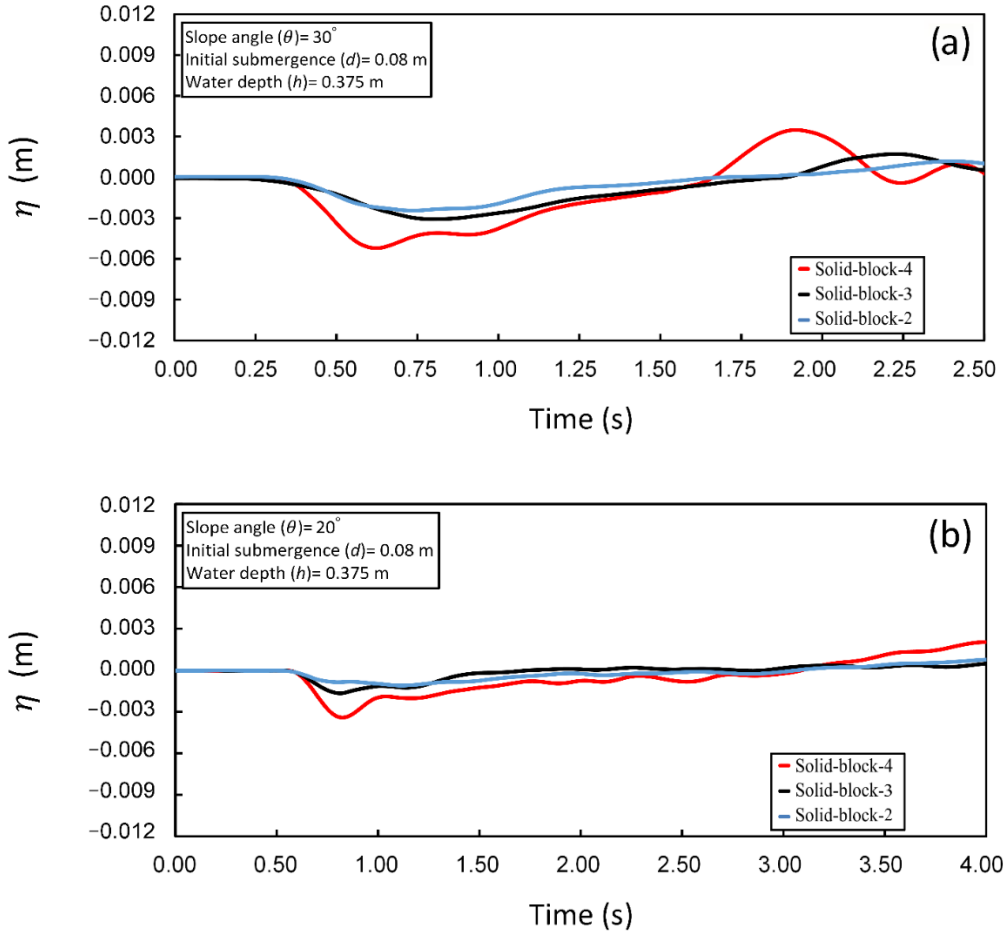

Figure 3.4. Laboratory recordings of the waves generated by a landslide at WG-1 (location of WG-1 is shown in Figure 3.2) for cases of slopes (a) $\theta = 30^{o}$, and (b) 20^{o}. In the panel legends, each experiment's parameters are specified.

The slide volume (V), initial submergence depth (d), and slope angle (θ) are three of the most crucial parameters for predicting the initial wave amplitude. Consequently, the non-dimensional maximum initial tsunami amplitude ($\frac{\eta_{max,n}}{d}$) was defined as a function of non-dimensional forms of these most crucial parameters ($\sin\theta$; $\frac{V}{d^3}$; $\frac{V}{l_s d^2}$; $\frac{d}{l_s}$; $\frac{d}{h}$ and $\frac{m_b}{\rho_w l_s d^2}$) as previously adapted by Watts (1997), Watts et al. (2005) and Najafi-Jilani and Ataie-Ashtiani (2008). In total, 14 empirical equations were developed and examined using the aforementioned non-dimensional parameters. These non-dimensional forms are inspired by previous research, including Fritz et al. (2004), Heller and Spinneken (2015) and Slingerland and Voight (1982). The powers and coefficients of the empirical equations are obtained using curve fitting of the experimental data by applying the polynomial fitting toolbox of MATLAB software (MathWorks, 2022). However, the final predictive equation for estimating $\eta_{max,n}$ are achieved through the stochastic optimization technique of Genetic

Algorithm (GA) (MathWorks, 2020). The GA toolbox uses a cost function to build a set of versatile routines for implementing a wide range of GA methods (Chipperfield et al., 1994). To quantify the quality of fit between observations (i.e. experimental and field data) and the calculations from the predictive equations, the NRMSE equation was used (Aida, 1978; Heidarzadeh et al., 2016, 2017):

$$NRMSE = \frac{\sqrt{\sum_{i=1}^{N}(obs_i - cal_i)^2}}{\sqrt{\sum_{i=1}^{N}(obs_i - \overline{obs})^2}} \tag{3.6}$$

where $i = 1, 2, \ldots, N$ refers to the number of observations/calculations; obs stands for observations (experimental/field data); cal is calculated values from predictive equations and $\overline{obs}$ is the average of observations. In an ideal case, if the agreement between observations and calculations is perfect, the NRMSE becomes zero.

3.2: Numerical simulation of submarine landslide (wave amplitude)

The numerical simulations of submarine landslide-generated waves were carried out using the Computational Fluid Dynamics package FlOW3D-Hydro (version 1.0, update 1), which is widely applied in industry and academia for modelling fluid mechanics problems (e.g. Nassiraei et al., 2016). In the 1960s and 1970s, FLOW3D-Hydro was used for the first time to simulate fluid flow algorithms at Los Alamos National Laboratory (Harlow and Welch, 1965). The solver is based on the Eulerian and Lagrangian frameworks' Finite Difference and Finite Volume formulations. The conservation of mass and momentum equations govern the flow of a Newtonian, incompressible fluid with free surface and density (ρ) in a bounded domain as follows:

$$\nabla \cdot u = 0 \tag{3.7}$$

$$\frac{\partial u}{\partial t} + u \cdot \nabla u = \frac{-\nabla P}{\rho} + \nu \nabla^2 u + g \tag{3.8}$$

where u denotes velocity, t denotes time, P denotes pressure, ν denotes kinematic viscosity, and g denotes gravitational acceleration acting in the z-direction. FLOW3D-Hydro uses the Fractional Area/Volume Obstacle Representation (FAVOR) and volume of fraction (Hirt and Nicholas, 1981) methods to solve the fully three-dimensional transient Navier-Stokes equations (Eq. 3.8). FAVOR defines solid boundaries within the Eulerian grid and computes flows corresponding to those boundaries by determining the fraction of areas and volume in partially blocked volume. FLOW3D-Hydro uses the Volume of Fluid (VOF) method to track free surface motion. FLOW3D-Hydro uses the following equation for the fraction of fluid function to compute the time evolution of the water surface while preserving the step-function nature of the distribution (Hirt and Nicholas, 1981):

$$\frac{\partial F}{\partial t} + u \,.\, (\nabla F) = 0 \tag{3.9}$$

where u is the velocity vector, t is time, and F is the fraction of fluid function.

The entire flow domain in the numerical model was 0.26 m wide, 0.50 m deep, and 1.8 m long. Water with a density of 1000 kg/m^3 at 20 ^{o}C was specified as the fluid inside the flume. The submergence depth (d) and water depth (h) were both 0.080 m and 0.375 m. Three solid concrete blocks in the shape of a prism with variable volumes were used in landslide generation simulations to provide a range of slide volumes (Table 3.2). These blocks were named Solid-block-4, Solid-block-3, and Solid-block-2, and their geometrical parameters were listed in Table 3.2. These blocks have a specific gravity (γ_s) of 2600 kg/m^3, which corresponds to the laboratory's actual blocks. The setup has a 45^o slope angle.

The equations were solved using a nested grid made up of two mesh planes with different spatial resolutions (Figure 3.5). In an area of 0.6 m (x-direction) 0.5 m (z-direction) around the landslide generation, a finer mesh with a grid size of 0.0010 m was used. In particular, it covers the impact area of the landslide with the free surface enabling a detailed reproduction of the landslide generation phase (e.g. $\eta_{max,n}$). The coarser grid, with a size of 0.00175 m, was used in the rest of the computational domain (Figure 3.5). The model's sensitivity to grid ratio was investigated (size of the larger grid to the smaller one). If the ratio of the size of the larger grid to the smaller grid is too large, spurious reflections can occur at the interface (e.g. more than 4). The grid ratio should be less than or approximately two, according to Flow Science (2021); here this value was 1.75. There were approximately 9.2×10^6 computational cells in total. The grid also covers the initial air space above the water to accommodate the block motion and surface waves.

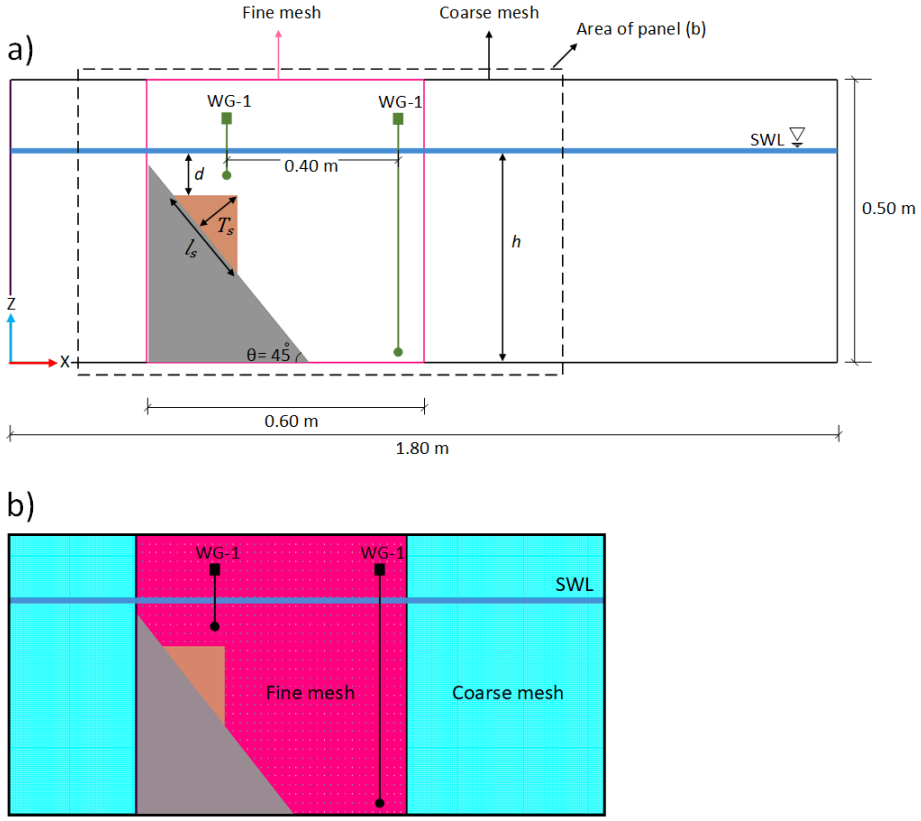

Figure 3.5. (a) The flume and sliding mass which were configured in the FLOW3D-Hydro model. Parameters are d, submergence depth; T_s, landslide thickness h, water depth; l_s, landslide length. (b) The nested two-level grid system adopted for simulations in this study comprising coarse mesh (green area) and fine mesh (pink area). SWL stands for still water level; WG stands for wave gauge. The WG-1 and WG-2 are located at X1= 0.47 m, Z1=0.33 m and X2= 0.87 m, Z2=0.022 m.

Except for the top surface, all boundary surfaces of the coarser mesh were defined as walls; the top surface was designated as a symmetrical boundary. The top, front, and back of the finer mesh area were defined as symmetric, while the other surfaces were of the wall type, with no-slip conditions around the walls. The symmetry boundary condition indicates that the conditions outside of the boundary are identical to those inside the boundary. At symmetry boundaries, the nodes can slide freely along the boundary, however, at other boundaries, the pressure in the neighbouring boundary cell is used to compute the traction. At symmetry boundaries no special conditions are needed, as there are zero velocity derivatives across the boundary, and hence zero turbulence production. Also, there is a zero-flow area that automatically ensures no advective or diffusive fluxes (Flow Science, 2022). As the free movement of waves from the front and back boundaries of the finer mesh are allowed into the coarser mesh, they are designated as symmetry boundaries. In addition, the top boundaries of both fine and coarse meshes are of symmetry types because they represent free water surfaces. Among the available options for simulating turbulent flows within FLOW3D-Hydro (i.e. Large Eddy Simulation – LES, k-ε, k- ω model and Renormalization Group - RNG), the RNG model was used in this work. The RNG model was chosen because it has a broader applicability than the standard k- ε model (Choi et al., 2007). Furthermore, in order to compare the impact of these turbulent models on the generated waves a set of simulations were conducted (Figure 3.6); The result of these tests indicate the impact of different turbulent on this problem is negligible (Figure 3.6). The coupled motion object has reproduced the landslide movement in the simulations presented here. Rather than dictating the movement of the slide through the prescribed velocity, the coupled motion object models the slide motions using fluid governing equations, gravitational and control forces, and momentums (Wei, 2005). The friction coefficient in the coupled motion is designated as 0.40 – 0.50 based on Coulombic friction measurements in the laboratory to calibrate the model.

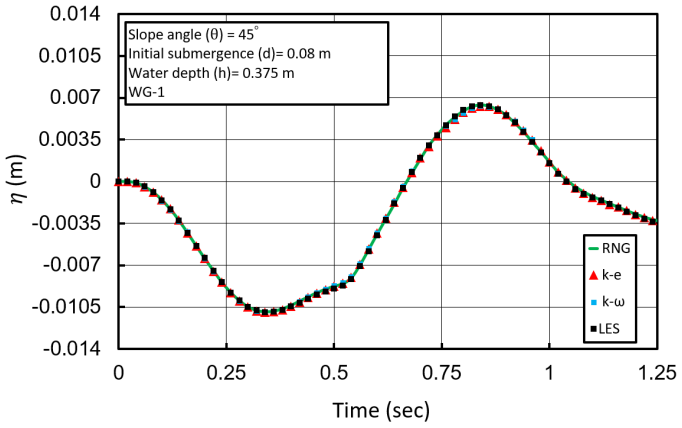

Figure 3.6. Comparison of available turbulent models (LES, k-ε, k- ω and RNG) in FLOW-3D Hydro on submarine landslide-generate waves recorded by WG-1. The Following setup were used to conduct these tests. Slope angel was 45-degree, water depth was 0.375 m, and initial water depth was 0.08 m.

The materials of the solid block and the incline influence this friction. The output interval was set to 0.02 s in the numerical model to match the time-dependent intervals of the outputs with the sampling rate of the actual wave gauge. Wave gauges located around the submerged slide are defined in the model to measure the free surface wave fluctuation; the locations of these gauges are fitted in the numerical setup corresponding to the actual locations in the physical experiments (Figures 3.1, and Figure 3.5).

The vertical amplitude of the waves in the experiments is relatively lower than the horizontal wavelength (Figure 3.7). However, such small amplitudes of the waves can be captured using the mesh with moderate cell densities in the vertical direction using the TruVOF (Volume of Fluid) approach which is unique to FLOW3D-Hydro (Flow Science, 2022). TruVOF is a split Lagrangian method that produces less cumulative volume error than other methods. The changing areas and volume fractions for each cell are calculated/updated at each time step, and the time step size is automatically adjusted to capture the dynamic free surface correctly as it changes within a cell. To ensure simulation stability and convergence, FLOW3D-Hydro employs the Courant Number (equation below) condition and ensures that it remains sufficiently below one:

$$C = \frac{U\,\Delta t}{\Delta x} \tag{3.10}$$

where C is Courant Number, Δt is time step, Δx is grid size and is U flow velocity. For simulations, FLOW3D-Hydro uses a dynamic time step (t), which means that the time step changes depending on the flow conditions. The initial time step in the simulations was 0.001 s and varied between 0.00035 and 0.0077 s during the simulations.

To examine the model's capability in reproducing real-world measurements and its validation (Oberkampf et al., 2002), numerical results are compared with previous physical experiments. (Figure 3.7). This validation is carried out with the Solid-block-4 (Table 3.2) and at two different wave gauges (WG-1 and WG-2; Figures 3.1 and 3.5). Because the purpose of this study is to investigate the wave characteristics around the source region, it is assumed that the two wave gauges around the sliding mass are adequate. Consistent with the physical model's results, where the Friction coefficient was in the range of 0.40 – 0.50, this coefficient was varied in the same range in this study numerical model (Figure 3.7). According to the comparison in Figure 3.7 between the modelled wave (i.e. simulations) and the actual one (i.e. observation), the numerical model performs satisfactorily. By adjusting the friction coefficient, this numerical model was calibrated to produce the best match with laboratory observations. The following equation was used to calculate the quality of match between observations and simulations:

$$\varepsilon = \frac{Obs_i - Sim_i}{Obs_i} \times 100 \tag{3.11}$$

where ε is the mismatch error, Obs_i is the observation point from physical experiments and Sim_i is the simulation results. The results show that a friction coefficient of 0.45 produces the best match with the fewest errors (Table 3.3); thus, it was used in the simulations.

Table 3.3. Calculating mismatch error between observations and simulations using Equation (3.11), for two wave gauges (WG).

Friction Coefficient	Simulation mismatch (WG-1)	Simulation mismatch (WG-2)
0.40	13%	16%
0.45	7%	9%
0.50	15%	13%

The model reproduces the maximum and minimum wave amplitudes as well as the wave period satisfactorily (Figure 3.7). There is a small deviation between simulations and observation immediately after the wave trough. Although the model has reproduced such deviation, its magnitude does not necessarily match the observations.

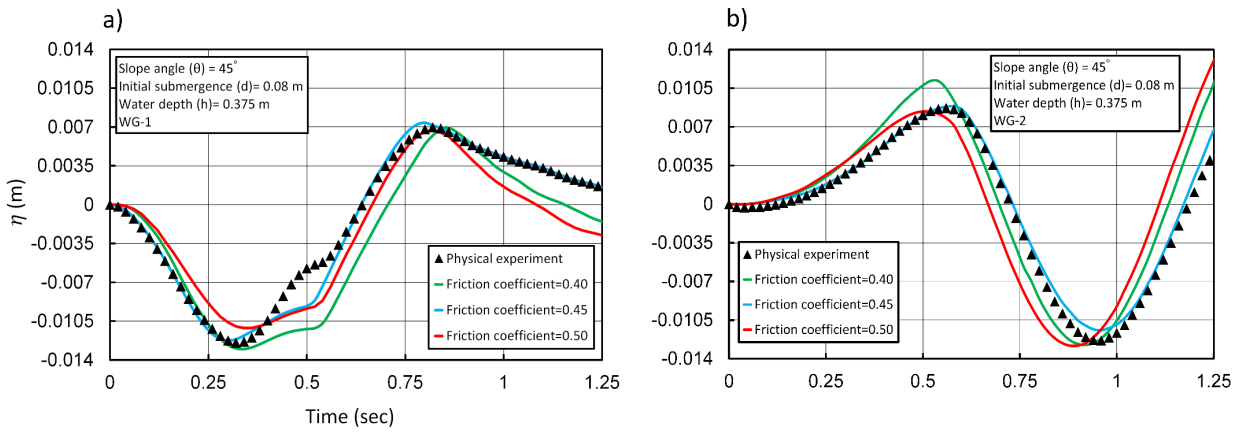

Figure 3.7. Comparison of this study's simulation results (coloured lines) with experimental waveforms at WG-1 (a) and WG-2 (b) (black triangles). Colour lines represent the variation of friction coefficients in simulations. This experiment employs the Solid-block-4 (Table 3.2).

To perform a mesh sensitivity analysis, the grid resolution was varied by doubling and halving the current meshes, and the results are shown in Figure 3.8. The results of the larger mesh (Figure 3.8, blue waveform) deviate by approximately 8% from those of the other two finer meshes. The waveforms from the two finer meshes are approximately identical (Figure 3.8, green and pink waveforms) which demonstrate that the results become stable. As a result, the mesh sizes chosen for this study (Figure 3.8,

pink waveform, mesh sizes 0.00175 m and 0.0010 m for coarse and fine meshes, respectively) are appropriate.

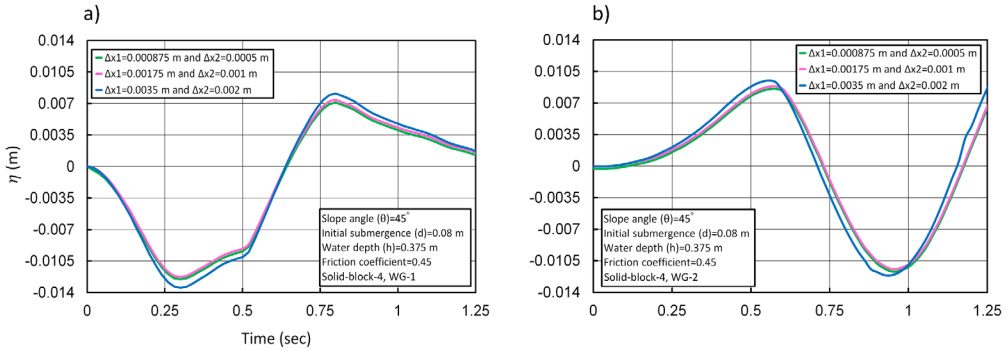

Figure 3.8. Sensitivity analysis of numerical simulations at WG-1 (a) and WG-2 (b) For various grid sizes. Δx1 and Δx2 are the coarse and fine mesh grid sizes, respectively. This sensitivity analysis employs the Solid-block-4 (Table 3.2).

Figure 3.9 shows a qualitative comparison of wave snapshots at different times between observations and simulations, indicating good agreement. It is worth noticing that the model (Figure 3.9, right) reproduces multiple wave troughs and peaks observed in the laboratory (Figure 3.9, left). This numerical model was generally accurate enough to carry out this research.

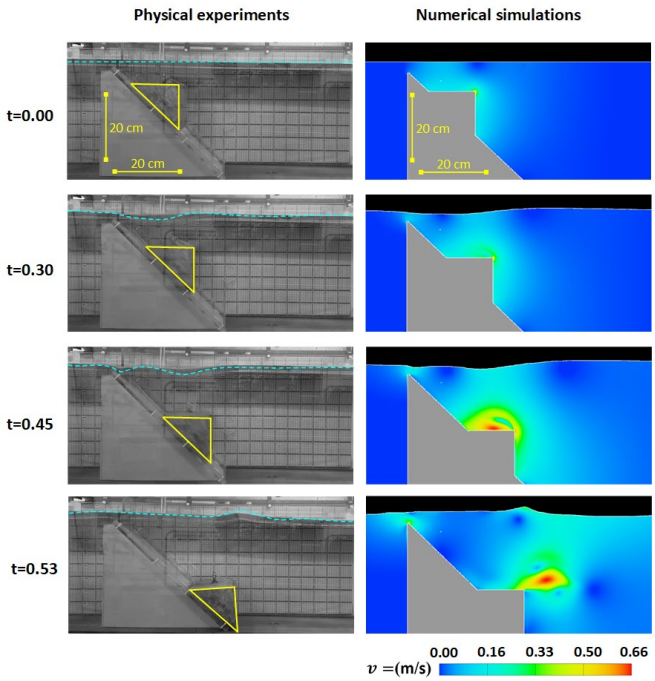

Figure 3.9. Snapshots of numerical simulations at various times (right column), as well as comparisons with physical experiments (left column). The colormap in the right panels depicts the velocities of water particles. The blue dashed lines in the left panels depict the water surface at various times. Solid-block-4 (Table 3.2) was the solid-block used in this study (Appendix).

Instead of calculating the viscous sub-layer as a separate region in a turbulent flow, FLOW3D-Hydro employs the logarithmic law-of-the-wall. The programme computes the law-of-the-wall velocity in the mesh cells adjacent to an obstacle and uses momentum equations to ensure that the velocity profile continues beyond the obstacle. The logarithmic layer normally extends in the region $30 \leq y^+ \leq 0.1\delta^+$ where, $y^+ = \frac{y\, u_T}{v}$ is the dimensionless wall distance; $\delta^+ = \frac{\kappa u_T}{v}$; κ is the thickness of the boundary layer; $u_T = \sqrt{\tau_w/\rho}$ is friction velocity; τ_w is wall shear stress; ρ is fluid density; v is the kinematic viscosity; and y is the absolute distance from the wall (Flow Science, 2022). For estimating y^+, the shear stress τ_w is needed to manually estimate. If manual estimation of τ_w is not possible, multiple simulations can be run to find the best fit. In general, y^+should be greater than 30 but less than several hundred (e.g., 300 – 500). Where the wall shear stress (τ_w) is unknown, y^+ cannot be determined a priori, and iterative simulation meshing may be required to find a suitable size. For this study's simulations, y^+ was ranged from 30 to 163, ensuring that meshing process was accurate.

3.3: Physical modelling of subaerial landslide (wave amplitude)

To validate the presented numerical model (Section 3.4), two sets of physical experiments involving solid-block and granular landslides were carried out at Brunel University London in a flume with following dimensions: 4.0 m in length, 0.26 m in width, and 0.5 m in height. In the physical experiments, the slope angle (α) and water depth (h) for both solid-block and granular landslides were set to 45 degrees and 0.246 m, respectively (Figure 3.10). A digital camera (Sony A6300) with a sampling frequency of 120 frames per second recorded the sliding process and measured the travel time (t_s).

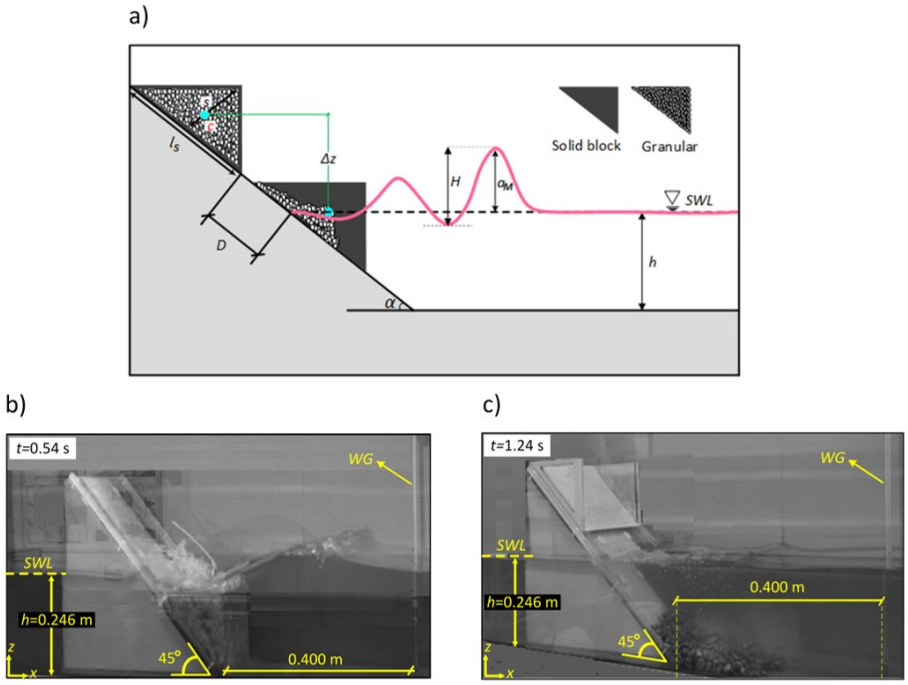

Figure 3.10. (a) Sketch showing the parameters used in this study for modelling subaerial solid-block and granular landslides. (b) Water surface status at time 0.54 s during the physical modelling of a subaerial solid-block landslide. (c) Same as "a", but for subaerial granular landslide at time 1.24 s. The location of the wave gauge for both granular and solid-block slides is at X=0.850 m, and Z=0.02 m. Parameters are: h, water depth; α, slope angle; SWL, still water level; t, simulation time; and η, wave amplitude; a_M, maximum wave amplitude; α, slope angle; l_s, length of landslide; D, travel distance (the distance from toe of the sliding mass to the water surface); Δz, the drop height measured between the locations of the landslide centroid at rest and the landslide centroid reaching the initial water level.

Since the travel distance for both solid-block and granular landslides was kept constant (D=0.045 m), the acceleration of the slides (a_s) can be calculated using the equation $a_s = 2\,D/{t_s}^2$ (Xue et al., 2019). Throughout this study, travel distance was defined as the distance from the toe of the sliding mass to the water surface (Figure 3.10). The impact velocity of a landslide could be calculated using the equation ${v_s}^2 = 2a_sD$. In the physical experiments (Section 3.2), the measured landslide velocities were roughly consistent with the values calculated using energy balance between the slide release and the impact location (Fritz et al., 2004):

$$v_s = \sqrt{2g\Delta z(1 - \tan\delta\cot\theta)} \tag{3.12}$$

where g is the gravitational acceleration, Δz is the drop height (Figure 3.10) (Δz=0.28 m for solid block and Δz=0.23 m for granular material in presented physical experiments, Section 3.2), θ=45° is slope angle, and δ is dynamic bed friction angle between slide bottom and slope surface for solid block (δ=24° and for granular material δ=28°).

The kinematics and dimensional data for the solid-block and granular slides used in the physics experiments are provided in Table 3.4. Granular landslides were constructed out of natural Granite, with a grain density of 2,750 kg/m^3, a grain diameter of 10 mm, a bulk slide density of 1,680 kg/m^3, and a bulk slide porosity of 15%. Blocks of concrete with a density of 2,600 kg/m^3 were used to simulate the waves generated by a landslide. Both the solid-block and granular slides had the same volume (V=2.60×10-3 m3). Net weights of solid-block and granular material landslides were 6.86 and 6.02 kg which indicates a 13% weight difference between them.

Table 3.4. The solid-block and granular landslides' geometrical and kinematic information used in physical experiments of subaerial landslides.

Parameter, unit	Solid-block***	Granular material
Slide width (w_s), m	0.260	0.260
Slide length (l_s), m	0.200	0.200
Slide thickness (T_s), m	0.100	0.100
Slide volume (V), m^3	2.60×10^{-3}	2.60×10^{-3}
Specific gravity (γ_s)	2.600	2.750
Slide weight (m_s) *, kg	6.860	6.020
Slide velocity (v_s), m/s	1.816	1.310
Slide Froude number** (F_r)	1.165	0.836

*: The weights of the solid block and granular material are slightly different because of the larger porosity of the granular material. **: Slide Froud number is calculated by using the following equation: $F = v_s/\sqrt{gh}$; the water depth (h) is 0.246 m in the presented physical experiments (Section 3.2). ***: The solid-block which used in this analysis is Solid-block-4 (Appendix).

Ataie-Ashtiani and Nik-Khah (2008) verified that the dynamic parameters of the waves generated by landslides are hardly affected by the shape of the sliding mass. Maximum landslide-generated wave amplitudes were reported to change by up to 15% when mean grain size was changed from 10 mm to 30 mm (Tang et al., 2018). Even without accounting for grain size, the predictive equations developed by Heller and Hager (2014) show impressive results. However, Tang et al. (2018) noted that the angle of the landslide's front could have a minor effect on the amplitude of the waves. It was considered in this study's physical experiments that were shown that scale matters (Section 3.2). Heller et al. (2008) proposed a criterion for avoiding scale effects, reporting that the effects can be negligible for Reynolds numbers ($R = g^{0.5}h^{1.5}/\nu$) greater than 3.0×10^5 and Weber numbers ($W = \rho g h^2/\sigma$) greater than 5.0×10^3 or water depth (h) approximately above 0.20 m. It should point out this format of Reynolds number is empirically derived through the study of Heller et al. (2008) where he compares two case of 2D and 3D subaerial landslide generated wave in physical experiments. At 20 degrees Celsius, the kinematic viscosity of water calculated to be $\nu = 1.01\times10^{-6}$ m^2/s and a surface tension coefficient to be $\sigma = 0.073$ N/m (Xue et al., 2019). $R = 3.8\times10^5$ and $W = 8.1\times10^5$ can be obtained using data from the physical experiments of this study (Table 3.5), suggesting that the scale effect is negligible in the presented experiments. Also, in order to avoid the lateral wall effect the criterion which proposed by (Du et al., 2003) were considered in this study; based on this criterion the width of flume must be at least 20 times more the diameter of grain size, the width of flume in this study is 0.260 m and the grain size is 10 mm (0.01 m) which is 26 times more than the grain size.

Chapter 3.4: Numerical simulation of subaerial landslide (wave amplitude)

In order to simulate the subaerial landslides, the FlOW3D-Hydro (version 1.0) was applied. The general specifics of this numerical model were introduced in Section 3.2.

The whole flow domain was 0.26 metres wide, 0.50 metres deep, and 4 metres long. The fluid inside the flume was set to water with a density of 1,000 kg/m^3. The depth of the water (h) ranged from 0.150 to 0.246 m. The angle of the slope (α) ranged from 30^o to 60^o. In the simulations, six solid blocks and six granular materials in the shape of a prism with different volumes (0.70×10^{-3}–2.60×10^{-3} m^3) were used to give a range for slide volumes (Table 3.5). During the validation phase of the numerical model, the water depth was 0.246 m and the slope angle was 45^o for both types of slides (Figure 3.11). According to the slides in the lab, the specific gravity (γ_s) of solid blocks was 2.60, and the specific gravity of granular material was 2.75. For soli-block modelling the Moving Object model was applied in setup of FLOW-3D Hydro (as same as the slide motion in Chapter 3.2) this model can simulate rigid body motion, while Sediment Transport Model are employed to model the granular material landslide. The sediment Transport model assumes multiple non-cohesive sediment species with different properties. The size of grain in simulation is matched with actual grain size (10 mm) in physical experiments.

For each type of landslide, the equations were solved using a uniform grid with a single mesh plane. In an area of 4.0 m (x direction) 0.5 m (z direction), a grid size of 0.0020 m was used for solid blocks, while a grid size of 0.0010 m was used for granular materials in the same area. For solid-block landslides, the total number of computational cells was 3.75×10^6, and for granular landslides, it was 15×10^6. Even though the model is only in two dimensions, it is recommended to have at least a few cells in the width direction (y-direction) (Flow Science, 2022), the reason for this is the solver (FLOW-3D Hydro) is only works in Three-Dimensional environment, in consequence to using this solver in a 2D problem there must be a few cells in y-direction to provide a semi-3D problem which could be solved by FLOW-3D Hydro, thus, in the y-direction, 10 cells were set for the mesh plane. A simulation of a granular landslide takes about 3.5 hours to run on a PC with an Intel (R) Core (TM) i7-8700 CPU with frequency of 3.20 GHz and 32 GB of RAM.

Table 3.5. Geometric data of the slides used for numerical simulations in this section simulations.

Slide-Number*	Slide width (w_s), m	Slide length (l_s), m	Slide thickness (T_s), m	Slide volume (V), m^3
Slide-1	0.260	0.106	0.051	0.70×10^{-3}
Slide-2	0.260	0.115	0.056	0.85×10^{-3}
Slide-3	0.260	0.121	0.064	1.00×10^{-3}
Slide-4	0.260	0.141	0.071	1.30×10^{-3}
Slide-5	0.260	0.185	0.085	2.00×10^{-3}
Slide-6	0.260	0.200	0.100	2.60×10^{-3}

*: Granular slides and solid-block geometry are the same. Solid-block landslides have a specific gravity (γ_S) of 2.60, while granular landslides have a specific gravity (γ_S) of 2.75.

The top, front, and back of the mesh areas were defined as symmetric, while the other surfaces were of the wall type, with no-slip conditions around the walls. The RNG model was used to simulate turbulent flows (Choi et al., 2007). The landslide movement has been reproduced by the coupled motion object in the simulations presented herein. The time intervals of the numerical model outputs were set to 0.02 s to be consistent with the actual sampling rates of the wave gauges in this study's laboratory. Because the greatest value for maximum initial wave amplitude occurred approximately 0.40 m from the slope's toe, this location was chosen for wave gauge installation (Figure 3.11).

Based on Coulombic friction measurements in the laboratory to calibrate the model for solid-block slides, the friction coefficient (f) in the coupled motion is 0.45, and it was 0.53 for granular landslides. With the following equation, the friction coefficient (f) is related to the dynamic bed friction angle (δ):

$$f = \tan(\delta) \tag{3.13}$$

As the Coulombic friction coefficient varies considerably over a small domain, the predictive equations of the majority of previous studies do not include it as an independent variable (Fritz et al., 2004; Heller and Spinneken, 2015; Noda, 1970).

The Courant number (Eq. 3.10) as a metric to ensure the stability of numerical calculations was always kept well below one. The initial time step for simulations was 0.0012 s and varied between 0.00015 and 0.0075 s during the simulations. The numerical models (for granular slides and solid-blocks) were validated by comparing their outputs to laboratory experimental data (Figure 3.10). The aforementioned criteria (Eq. 3.11) were used to assess the quality of the agreement between laboratory observations and simulations. The results show that the mismatch errors between physical experiments and numerical models for solid-block and granular materials are 5% and 6%, respectively, indicating

that presented models reproduce the measured waveforms satisfactorily (Figure 3.11 c–d). The Fast Fourier Transform (FFT) of the MATLAB package (MathWorks, 2022) was used for spectral analysis of the water waves.

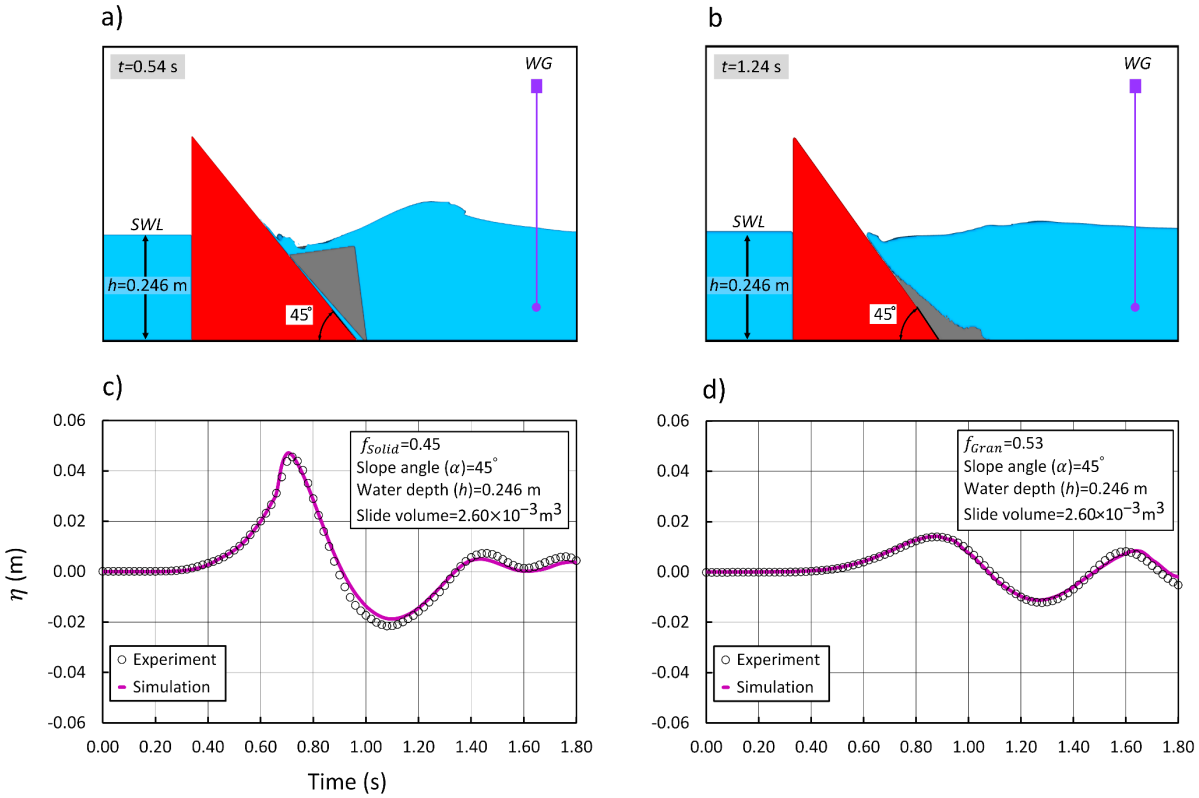

Figure 3.11. (a) and (b) Numerical simulations of the landslide set-ups shown in "a" and "b" at the same times, respectively. (c) and (d) Comparisons of measured (circles) and simulated (pink lines) waves at the location of the wave gauge (WG) for subaerial solid-block and granular landslides, respectively. The location of the wave gauge for both granular and solid-block slides is at X=0.850 m, and Z=0.02 m. Parameters are: h, water depth; α, slope angle; SWL, still water level; t, simulation time; and η, wave amplitude.

Mesh sensitivity analyses for solid-block and granular landslides were performed to determine the most efficient mesh resolution (Figure 3.12). To ensure that the model captures the smaller wave amplitudes generated by granular materials, the initial mesh size for the granular slides was twice that of the solid-block slides. The effect of mesh density on simulated waveforms was investigated in both types of landslides by doubling and halving the current meshes. For the solid block, the coarser mesh was deviated 4% (Figure 3.12a, Δx =0.0040) from the two other finer meshes; for the granular landslide, the deviation was 5% (Figure 3.12a, Δx =0.0020). Because the simulation results from two finer meshes for both solid-block and granular materials show no improvement, the current mesh sizes (Δx =0.0020

for solid block and Δx =0.0010 for granular material) were appropriate and were used for the next simulations.

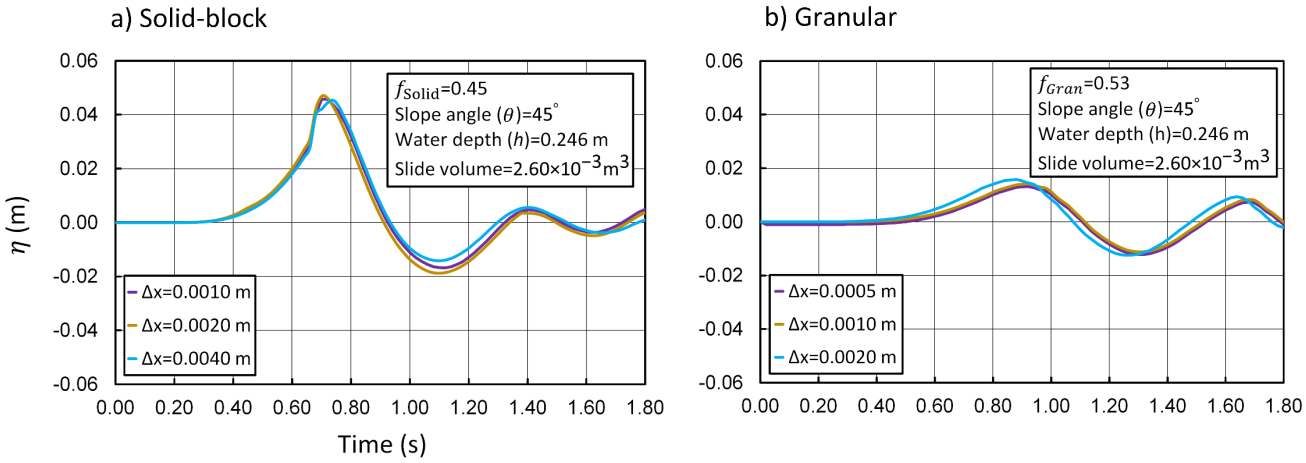

Figure 3.12. Sensitivity analysis to mesh size (Δx) for subaerial solid-block (a) and granular (b) landslides. The slope angle and water depth for these experiments are set to 45° and 0.246 m, respectively.

Panizzo et al. (2005) was discussed the mechanism of landslide motion both under air and underwater, stating that the motion begins at rest and accelerates under gravitational forces until it impacts the water, causing a rapid decrease in slide velocity until it stops. Figure 3.13 depicts the displacement and velocity profiles of the landslides throughout their entire travel. These profiles were based on landslide block 6 (Slide-6 in Table 2), with a water depth of h=0.286 m and a slope angle of 45°. The velocity of the slide (v_s) was reached its maximum value at the time of the slide's intrusion into water, which is known as the impact time (t_{imp}). Following the impact, the slides was moved in a submarine motion until they stop (t_{stop}). To determine the displacement and velocity of the slides, a probe (one for solid-block slides and one for granular slides) was attached to the centre of each landslide and measured the displacement and velocity of the landslides from the release point until they stopped. The solid-block landslide has a maximum velocity of 1.8 m/s, while the granular slide has a maximum velocity of 1.35 m/s, as shown in Figure 3.13. The solid landslide takes approximately 1.0 s to come to rest, whereas the granular landslide takes approximately 1.3 s.

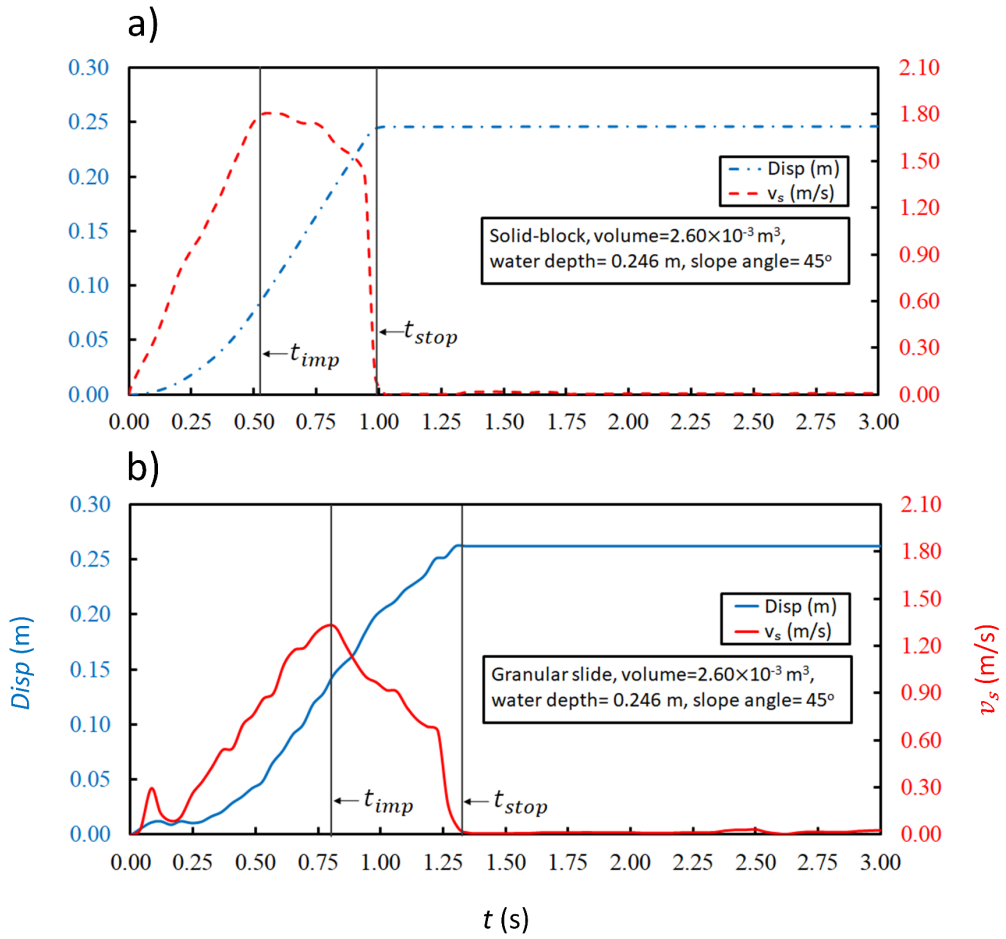

Figure 3.13. (a) Solid-block landslide displacement and velocity versus time simulation for Slide-6 (Table 2). (b) The same as 'a,' but for granular landslides. Parameters are: v_s is slide velocity; t_{stop} is the stop time of the landslide; t_{imp} is the time of the impact of the subaerial landslide with water surface; $Disp$ is displacement.

The published experimental data on both solid-block and granular landslides (Figure 3.14), as well as new numerical data generated by this study were used to develop the predictive equations. Zweifel et al. (2004), Saelevik et al. (2009), Miller et al. (2017), and Xue et al. (2017) are the authors of the published data (2019). All of these experiments are based on 2D laboratory tests conducted in wave flumes with lengths of 11 m, 25 m, 33 m, and 10 m, respectively. Zweifel et al. (2004) used physical modelling to investigate subaerial landslide dynamics and discovered that the water depth and slide thickness were the governing parameters on maximum wave amplitudes. Saelevik et al. (2009) investigated the impact of slide geometry on the impulsive waves produced by subaerial landslides. According to the findings of Saelevik et al. (2009), decreasing the slide length creates a deeper void for the collapse of the leading wave, resulting in a larger trailing wave. Miller et al. (2017) studied the impact of effective mass (a fraction of total landslide mass) on activating the leading wave in a series of large-scale physical modelling (flume length of 33 m).

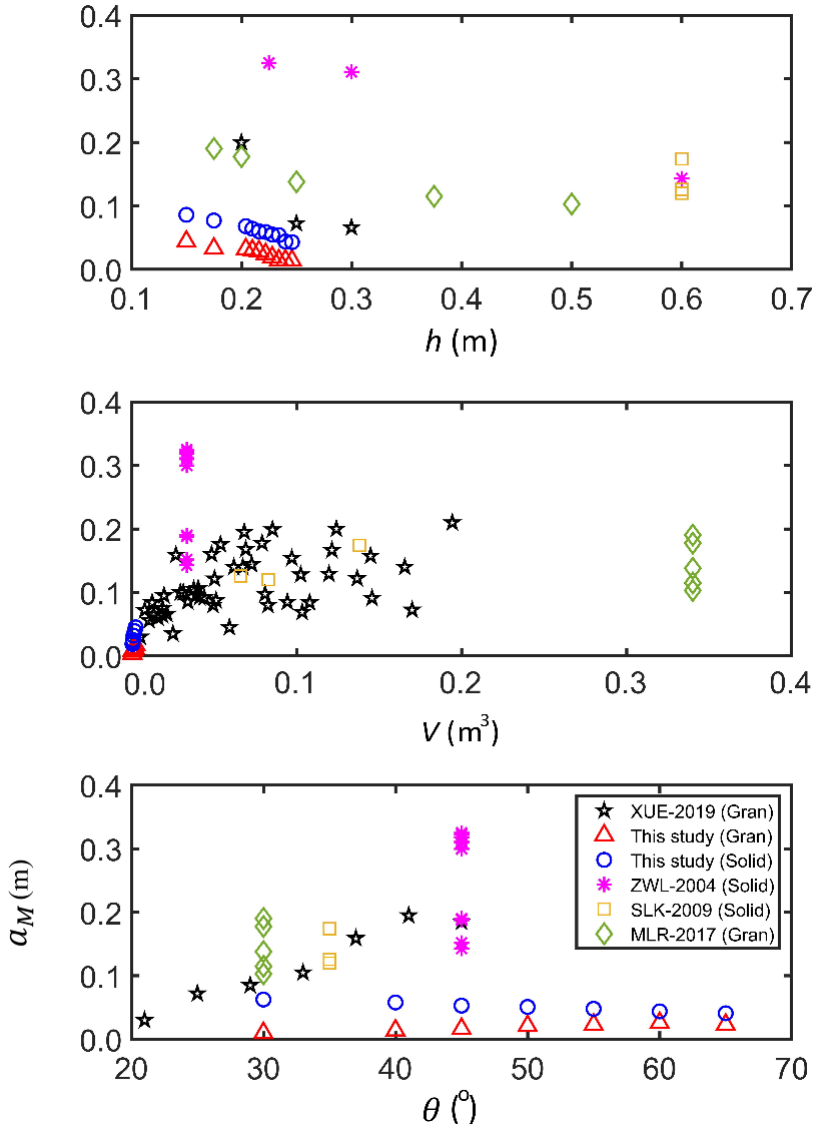

Figure 3.14. Expiring experimental data on subaerial solid-block and granular landslides, as well as this study artificial numerical data, were used to develop the resented predictive equations. XUE-2019, Xue et al. (2019); ZWL-2004, Zweifel (2004); SLK-2009, Saelevik et al. (2009); MLR-2017, Miller et al. (2017) are abbreviations (2017). The following parameters are used: h, water depth; V, slide volume; θ, slope angle; and a_M, maximum initial wave amplitude. The non-breaking wave data was used by Miller et al. (2017).

Figure 3.14 summarises previously published data, whereas Figure 3.15 displays wave classifications for data generated in this study as well as some of the literature data (for which information was available), indicating that all data points belong to intermediate waves and the majority are of the Stocks type.

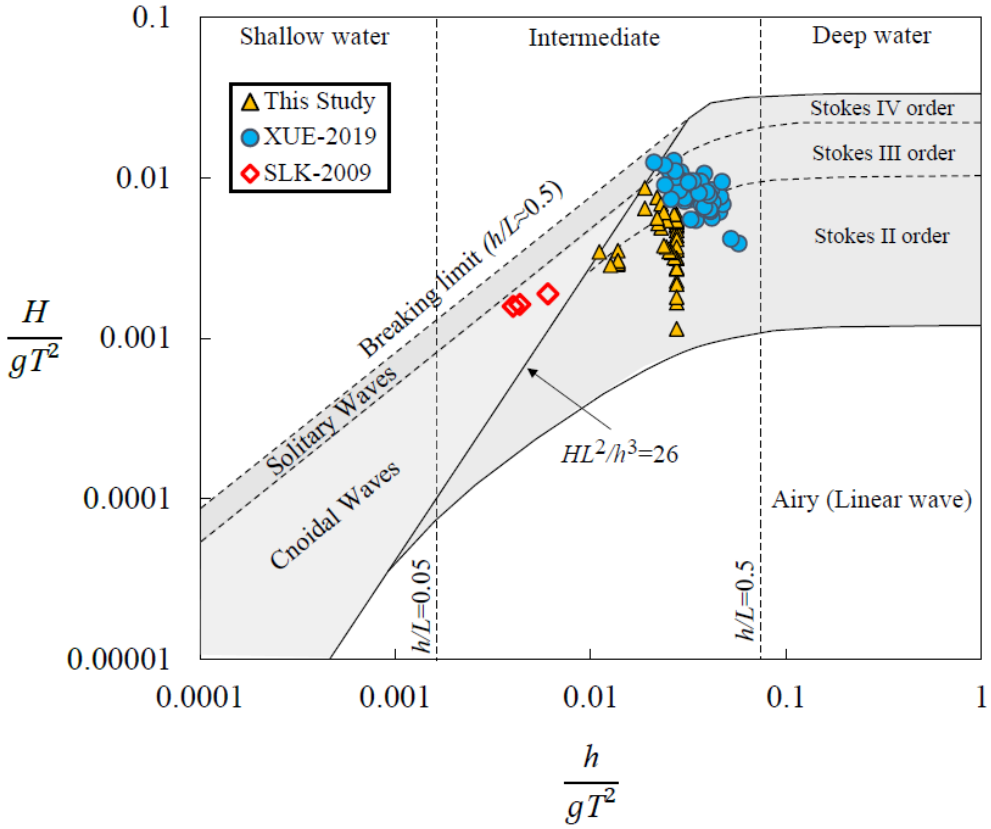

Figure 3.15. Wave classifications for this study's experimental data (triangles), Xue et al. (2019) (circles, XUE-2019), and Saelevik et al (diamonds, SLK-2009). The wave period (T) for Xue et al. (2019) data is calculated using their equation: $T = 5.237F^{0.253}(\frac{T_s}{h})^{0.032}(\frac{l_s}{h})^{0.029}\tan^{0.028}\theta$, where F is the Froude number, T_s is slide thickness, l_s is slide length, h is water depth, θ is the slope angle, and H is wave height from trough to crest.

Chapter 3.5: Physical experiments of subaerial landslide (wave period)

In this section, the physical modelling of subaerial solid-block landslide-generated waves was studied in the wave flume at Brunel University London with following dimensions: 0.26 m in width, 0.50 m in depth, and 6.0 m in length (Figure 3.16). In total, 51 tests of subaerial landslides were performed by varying the volume of the sliding mass (Table 3.7), the water depth, the Froude number, and the wave time series. The sliding masses properties were provided in Table 3.2 (Appendix).

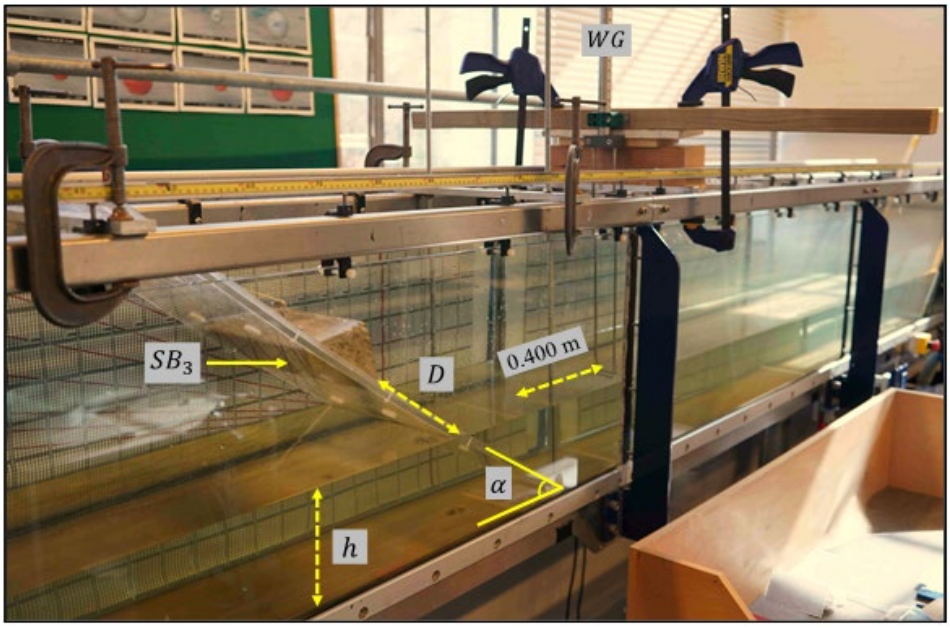

Figure 3.16. The wave flume was used in this study for physical experiments, photo showing the wave gauge (WG) and slope. The parameters are as follows: α, slope angle; h, water depth; D, travel distance (the distance between the toe of the sliding mass and the water surface); and Sb_3, Solid-block-3 (Table 3.2). The toe of the slope and the wave gauge are 0.40 m apart.

In this section of the study, the incline's slope angle was set to 30°. 51 scenarios were tested by varying the water depth from 0.06 m to 0.31 m, applying four sliding masses ($V1$- the smallest, $V2$, $V3$, and $V4$- the largest), and changing the velocity of the mass (Table 3.6).

Table 3.6. The condition of each test for 51 physical tests of subaerial solid-block landslide-generated waves. The slope angle is 30° for all tests. The parameters are as follows: F, Froude number; h, water depth; T_M, wave period; D, travel distance (the distance from toe of the sliding mass to the water surface); a_M, maximum wave amplitude; $M_s = m_s/(\rho_w w h^2)$, nondimensional mass slide, where ρ_w is density of water, and w is width of the concrete block.

Test No	Solid block No	F	h (m)	D (m)	T_M (s)	a_M (m)	M_s	Mechanism
1	Solid-block-1	0.3619	0.25	0.14	0.50	0.0123	0.066	Gravity
2	Solid-block-1	0.0708	0.25	0.14	1.11	0.0028	0.066	Controlled
3	Solid-block-1	0.1123	0.25	0.14	0.74	0.0029	0.066	Controlled
4	Solid-block-1	0.0893	0.25	0.14	0.73	0.0056	0.066	Controlled
5	Solid-block-1	0.3827	0.22	0.14	0.67	0.0146	0.085	Gravity
6	Solid-block-1	0.3870	0.19	0.14	0.50	0.0151	0.114	Gravity
7	Solid-block-1	0.0458	0.19	0.14	1.14	0.0056	0.114	Controlled
8	Solid-block-1	0.1004	0.19	0.14	1.08	0.0056	0.114	Controlled
9	Solid-block-1	0.2205	0.19	0.14	1.06	0.0057	0.114	Controlled
10	Solid-block-1	0.3853	0.16	0.14	0.58	0.0165	0.160	Gravity
11	Solid-block-1	0.3724	0.06	0.14	0.52	0.0234	1.139	Controlled
12	Solid-block-2	0.3650	0.06	0.14	0.50	0.0216	2.028	Controlled
13	Solid-block-2	0.3641	0.28	0.14	0.53	0.0166	0.093	Gravity
14	Solid-block-2	0.3887	0.25	0.14	0.67	0.0194	0.117	Gravity
15	Solid-block-2	0.0510	0.25	0.14	0.89	0.0057	0.117	Controlled
16	Solid-block-2	0.0896	0.25	0.14	0.65	0.0127	0.117	Controlled
17	Solid-block-2	0.1186	0.25	0.14	0.61	0.0107	0.117	Controlled
18	Solid-block-2	0.3795	0.12	0.14	0.65	0.0221	0.507	Controlled
19	Solid-block-2	0.3798	0.19	0.14	0.63	0.0246	0.202	Gravity
20	Solid-block-2	0.0586	0.19	0.14	0.77	0.0101	0.202	Controlled
21	Solid-block-2	0.1903	0.19	0.14	0.69	0.0137	0.202	Controlled
22	Solid-block-2	0.1942	0.19	0.14	0.61	0.0181	0.202	Controlled
23	Solid-block-2	0.3725	0.16	0.14	0.61	0.0278	0.285	Gravity
24	Solid-block-2	0.3646	0.13	0.14	0.65	0.0290	0.432	Gravity
25	Solid-block-3	0.3886	0.30	0.14	0.69	0.0260	0.143	Gravity
26	Solid-block-3	0.3840	0.28	0.14	0.71	0.0261	0.165	Gravity
27	Solid-block-3	0.3725	0.25	0.14	0.67	0.0289	0.206	Gravity
28	Solid-block-3	0.0892	0.25	0.14	1.25	0.0081	0.206	Controlled
29	Solid-block-3	0.0596	0.25	0.14	1.13	0.0123	0.206	Controlled
30	Solid-block-3	0.0883	0.25	0.14	1.08	0.0142	0.206	Controlled
31	Solid-block-3	0.3767	0.22	0.14	0.64	0.0321	0.267	Gravity

32	Solid-block-3	0.3662	0.19	0.14	0.62	0.0348	0.357	Gravity
33	Solid-block-3	0.1362	0.19	0.14	1.41	0.0125	0.357	Controlled
34	Solid-block-3	0.1369	0.19	0.14	1.06	0.0122	0.357	Controlled
35	Solid-block-3	0.0518	0.19	0.14	1.08	0.0146	0.357	Controlled
36	Solid-block-3	0.3827	0.16	0.14	0.64	0.0361	0.504	Gravity
37	Solid-block-3	0.3874	0.13	0.14	0.71	0.0355	0.763	Gravity
38	Solid-block-3	0.3624	0.10	0.14	0.51	0.0328	1.290	Gravity
39	Solid-block-4	0.3649	0.31	0.14	0.71	0.0551	0.271	Gravity
40	Solid-block-4	0.3610	0.28	0.14	0.71	0.0569	0.332	Gravity
41	Solid-block-4	0.3590	0.25	0.14	0.71	0.0579	0.416	Gravity
42	Solid-block-4	0.0511	0.25	0.14	1.51	0.0107	0.416	Controlled
43	Solid-block-4	0.0597	0.25	0.14	1.47	0.0100	0.416	Controlled
44	Solid-block-4	0.0876	0.25	0.14	1.41	0.0126	0.416	Controlled
45	Solid-block-4	0.3827	0.22	0.14	0.68	0.0575	0.537	Gravity
46	Solid-block-4	0.3870	0.19	0.14	0.82	0.0573	0.720	Gravity
47	Solid-block-4	0.0464	0.19	0.14	1.28	0.0116	0.720	Controlled
48	Solid-block-4	0.0682	0.19	0.14	1.41	0.0208	0.720	Controlled
49	Solid-block-4	0.3853	0.16	0.14	0.58	0.0547	1.016	Gravity
50	Solid-block-4	0.3874	0.13	0.14	0.80	0.0475	1.538	Gravity
51	Solid-block-4	0.3820	0.10	0.14	0.52	0.0369	2.600	Gravity

For twenty-five of the experiments, the blocks were allowed to slide freely down the slope after being released from their resting position at the top. The remaining tests were run by varying the solid-block's speed; In particular, a rope with a mounted hook were used for each slide to manually control the speed of slides. The rationale for conducting the controlled tests was to change the velocity of the mass (v_s) and consequently to provide a range for the Froude number (F), which is defined as:

$$F = \frac{v_s}{\sqrt{gh}} \tag{3.14}$$

The average velocity of the sliding blocks was calculated from videos of the experiments recorded with a camera (model Sony A6300) sampling at a rate of 120 frames per second. At a distance of 0.40 m from the toe of the incline, a wave gauge of the HRIA-1016 model was used to record the wave times series.

The Fast Fourier Transform (FFT) algorithm of the MATLAB package (the command 'fft' in MathWorks, 2022) was used to determine the dominant wave period of the waves generated by the landslide. Due to the 6.0 m length of the wave flume, only the initial phases of the waveforms were used, as the later phases represented the reflected waves. The experimental data points were fitted using the Nonlinear least-square regression model from the 'fitoptions' collection of the MATLAB package (MathWorks, 2022) to determine correlations between the wave period and the various

landslide parameters. The stochastic optimization method of the Genetic Algorithm implemented in MathWorks (2022) was used to develop the ultimate predictive equation, a multi-variant equation.

Figures 3.16 and 3.17 demonstrate the time series for all of the physical experiments by classifying the waveforms into two categories studying the impacts of landslide volume (Figure 3.16), and Froude number (Figure 3.17). Regarding the effect of Froude number on the wave characteristic, visual inspections of Figure 3.16 reveal that wave period increases by a decrease in Froude number; wave amplitude increases by an increase in Froude number. The FFT analyses were performed to quantify the dominant wave periods which are presented in Section 4.4.

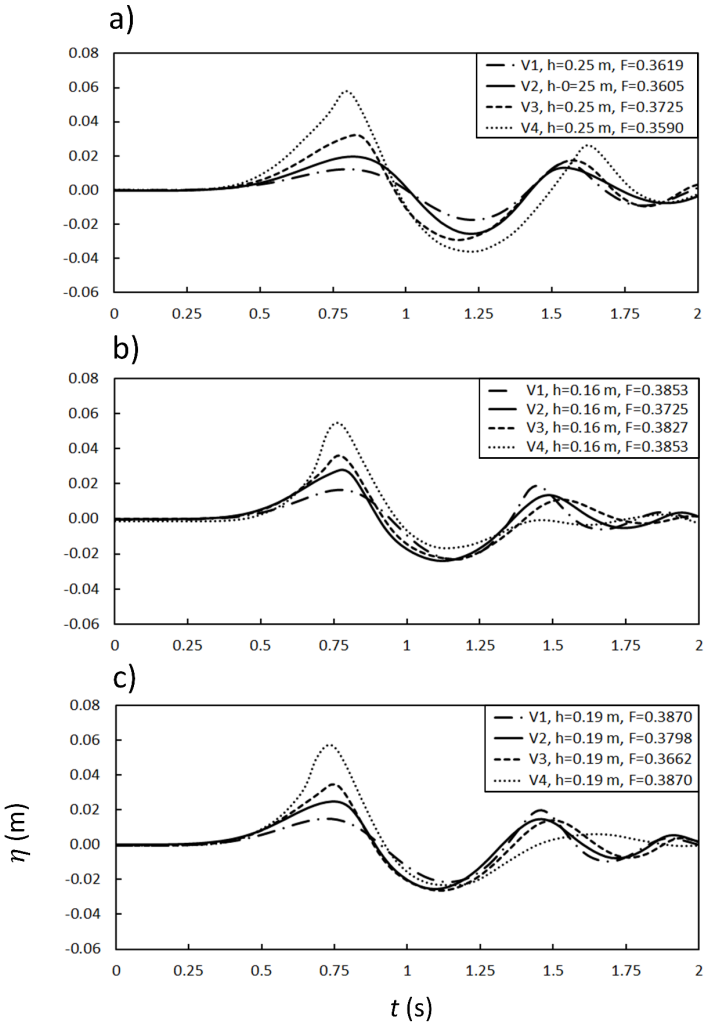

Figure 3.17. The recorded experimental water waveforms for the solid-block subaerial landslide-generated waves during the physical modelling using a range of concrete blocks ($V1$ to $V4$) with diverse water depths (h) and Froude numbers (F) (Table 3.7) to examine the effect of landslide volume on the resulting waveforms. The horizontal axis shows time (t), and the vertical axis shows wave amplitude (η).

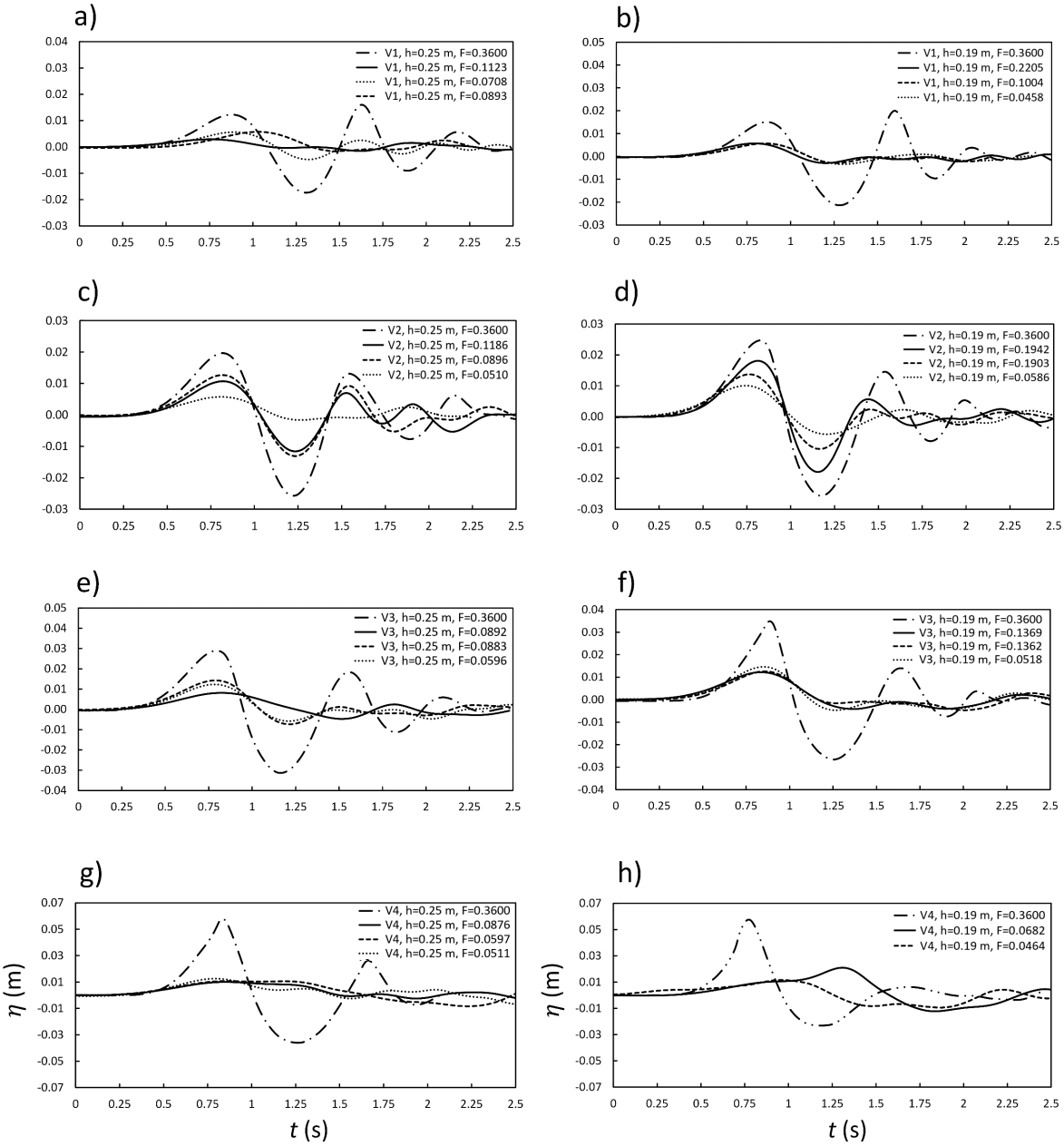

Figure 3.18. The recorded experimental water waveforms for the solid-block subaerial landslide-generated waves during the physical modelling using a range of concrete blocks ($V1$ to $V4$) with diverse water depths (h) and Froude numbers (F) (Table 3.7) to examine the effect of Froude numbers on the resulting waveforms. The horizontal axis shows time (t), and the vertical axis shows wave amplitude (η).

Figure 3.19 depicts a 3D representation of the experiments, mapping the maximum wave amplitudes (a_M) relative to volumes of the landslide blocks (V) and water depth (h).

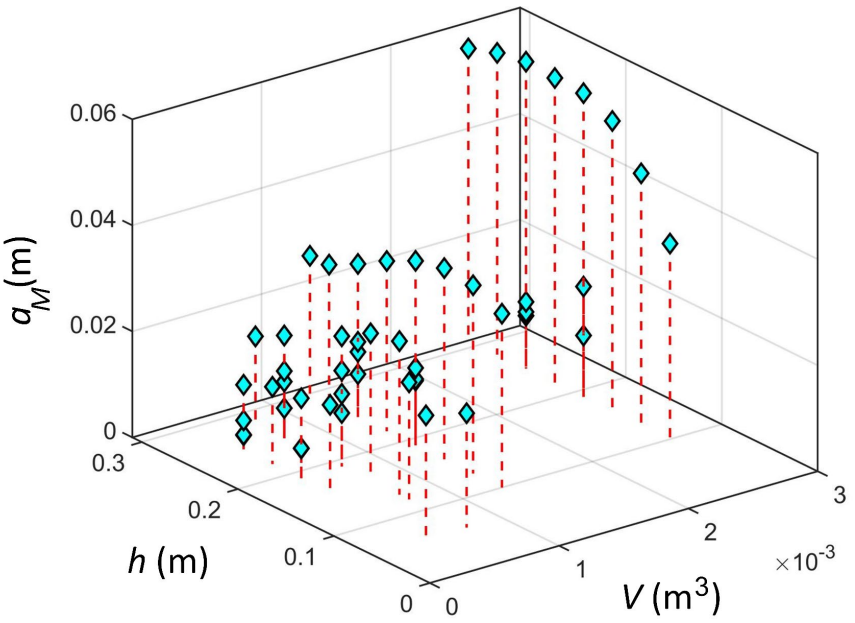

Figure 3.19 A 3D projection of maximum wave amplitudes (a_M) versus solid block volumes (V) and water depths (h) based on this study experiments.

It has long been recognised that experimental studies are vulnerable to scale effects, which can cause laboratory results to deviate from reality (Hughes, 1993; Heller, 2011). As a result, it is critical to investigate potential scale effects and ensure that they are within acceptable limits. According to Hughes (1993) and Heller (2011), most Coastal Engineering problems can be easily experimented with in a hydraulic laboratory using Froude similitude. However, scale effects can be significant in some cases, such as when modelling waterfalls and spillways, which normally experience significant air entrainment. For the physical tests of this study, scale effects were investigated by contrasting results obtained at various scales (Figure 3.20). For this analysis, the pairs of experiments with similar nondimensional parameters M_s (nondimensional mass, $M_s = m_s/(\rho_w w h^2)$ are selected, where m_s is the slide mass, w is slide width), F (Froude number based on Equation 1) and S (nondimensional slide thickness, $T_N = T_s/h$, where T_s is slide thickness, Figure 3.1) according to the method practiced by Heller and Hager (2011). For this study, the waveforms were nondimensionalized (Figure 3.20). Two sets of experiments were examined; one set at a scale ratio of 0.57 (Figure 3.20a) and the other set at a scale ratio of 0.56 (Figure 3.20b). Scale effects seemed small in both instances, as shown in Figure 3.20. It should point out the ratio of slide volumes (V_1 and V_2 for Figure 3.20a, and V_2 and V_3 for Figure 3.20b) were consider as the key parameter to calculate the aforementioned ratios.

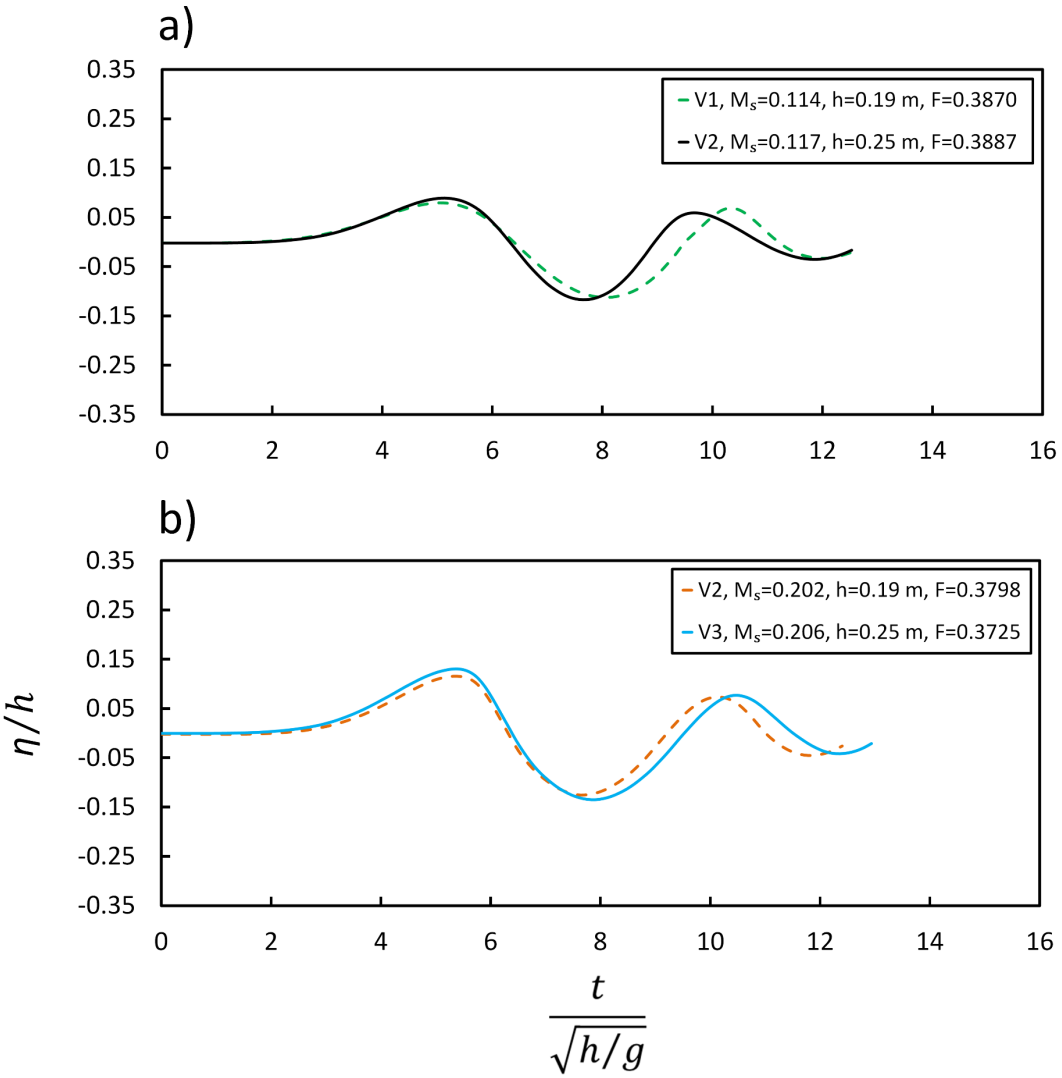

Figure 3.20 Waveforms (nondimensional) for two pairs of physical experiments with nearly equivalent nondimensional masses (M_s) and Froude numbers (F) to study scale effects during physical modelling. $V1$, $V2$, and $V3$ are different solid-blocks (Table 3.7), h is water depth, η is the amplitude of the waves, t is the time, and g is the gravitational acceleration.

Chapter 4: Results

Chapter 4: Results

Chapter 4 describes the results of the physical experiments as well as numerical simulations for both type of landslides (i.e. submarine and subaerial slides). The results of sensitivity analysis through the physical experiments and numerical simulation for submarine and subaerial landslide generated waves are discussed in this chapter. The predictive equations for estimating the maximum initial wave amplitude and period are introduced, and the performance of these equations is evaluated based on reproducing the a_M and T_M for actual previous tsunami events.

4.1: Physical modelling of submarine landslides (wave amplitude)

In this section, the experimental data were used to establish a relationship between $\eta_{max,n}$ and different landslide parameters, based on dimensional parameters.

Three curves were fitted to the experimental data of Watts (1997) (abbreviated as WTS-97), Ennet and Grilli (2007) (ENT-07), and Najafi-Jilani and Ataie-Ashtiani (2008) (JIL-08) to determine the power of the relationship between d and $\eta_{max,n}$ (Figure 4.1a). For these experimental data, the initial submergence depth ranges from 0.025-0.189 m. An inverse relationship between d and $\eta_{max,n}$ was discovered; however, the rate of change varied depending on the experimental data (Figure 4.1a). The powers of the relationship obtained for the experimental data of WTS-97 and JIL-07 $\eta_{max,n}$ were in the same range, but not for ENT-07. This could be attributed to ENT-07's unique landslide geometry and 3D nature (Heller and Hager 2011; Ruffini et al. 2019). The experimental setup in this study was similar to the data from JIL-08 and WTS-97. Accordingly, the effects of the initial submergence, d, was considered with the average relationship power of WTS-97 and JIL-07 data as:

$$\eta_{max,n} \propto d^{-1.095} \tag{4.1}$$

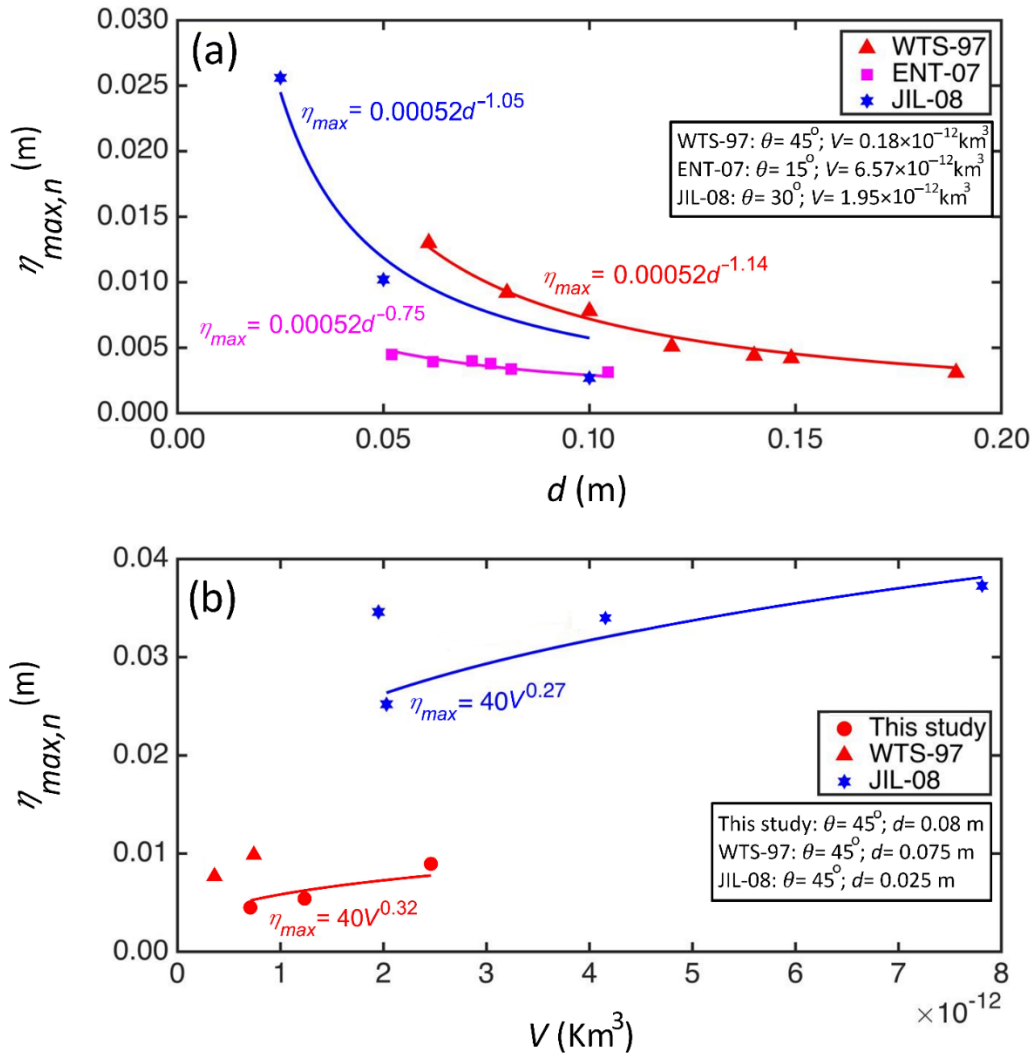

Figure 4.1. Curve fitting to the experimental data of the maximum negative initial wave amplitude ($\eta_{max,n}$) versus (a) initial submergence depth, d, and (b) sliding mass volume, V. WTS-97, Watts (1997); ENT-07, Enet and Grilli (2007); JIL-08, Najafi-Jilani and Ataie-Ashtiani (2008). The data points obtained from this study's experimental work are represented by solid red circles.

In this study, the existing experimental data from WTS-97 and JIL-08 were combined with the generated physical tests for V. (Figure 4.1b). These data, with V ranging from 0.35×10^{-12} -7.80×10^{-12} km^3, revealed a direct relationship between V and $\eta_{max,n}$. The equations associated with the solid lines (Figure 4.1b) were used to derive the following relationship. The average powers obtained by fitting equations to the experimental data from JIL-08 and this study were used to calculate V power as follows:

$$\eta_{max,n} \propto V^{0.295} \quad (4.2)$$

This study's physical experiments and those of JIL-08 were shown a direct relationship between $\eta_{max,n}$ and θ (Figure 4.2). The effect of θ was investigated by varying the slope angle from 15°-60°.

The power of $\sin\theta$ was calculated as follows by averaging the powers of the fitted equations using experimental data from this study and JIL-08:

$$\eta_{max,n} \propto (\sin\theta)^{1.650} \tag{4.3}$$

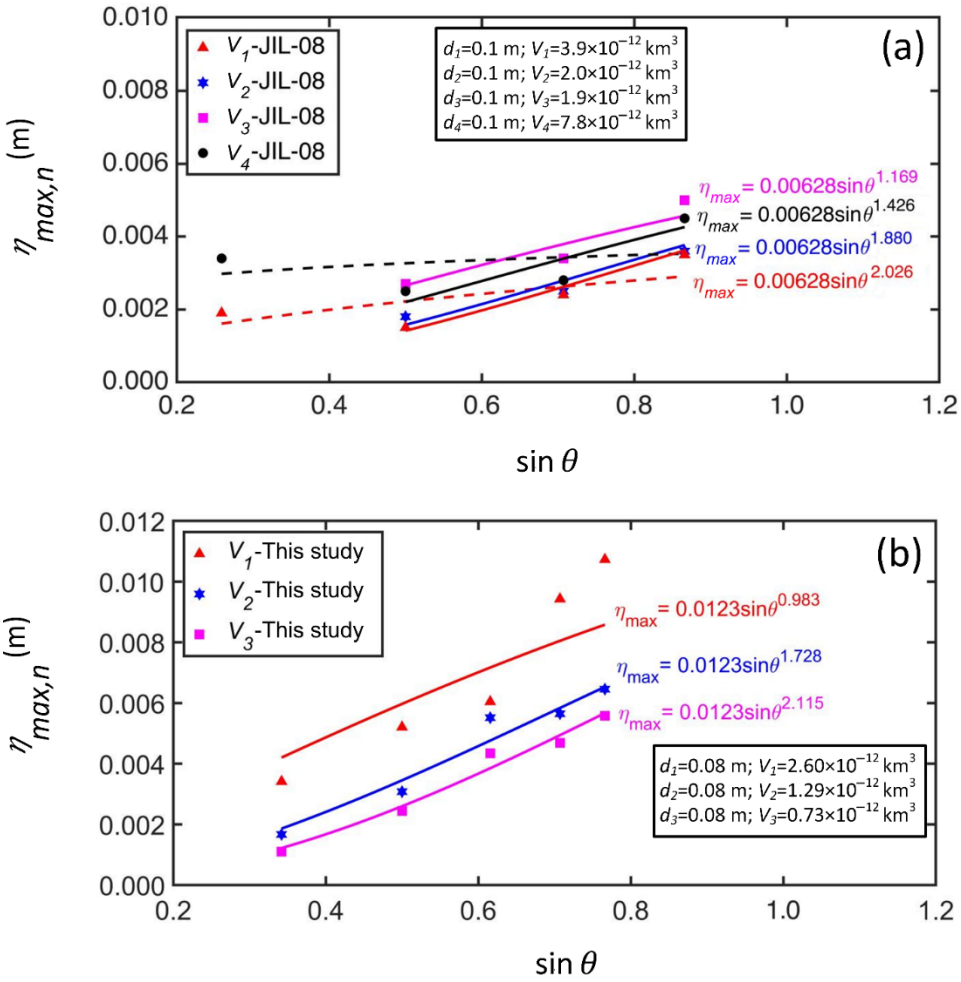

Figure 4.2: Curve fitting of the maximum negative initial wave amplitude ($\eta_{max,n}$) and slope angle (θ) on experimental data for (a) JIL-08 and (b) this study.

Curve fitting on existing experimental data shows that V and θ are directly related to $\eta_{max,n}$ (Figures 4.1b and 4.2), whereas d is inversely related (Figure 4.1a). 14 equations for predicting $\eta_{max,n}$ are developed here by considering the non-dimensional forms of these three essential landslide parameters (Eqs. 4.4–4.12 in Table 4.1).

Table 4.1 The candidate non-dimensional equations for estimating the maximum initial amplitude of landslide waves ($\eta_{max,n}$).

Candidate equations	Equation number	*NRMSE*[*]
$\frac{\eta_{max,n}}{d} = 0.023 \times \frac{(V/d^3)^{0.295} \times \sin\theta^{1.650}}{(d/l_s)^{1.095}}$	(4.4)	0.40
$\frac{\eta_{max,n}}{d} = 0.068 \times (\frac{V/d^3 . \sin\theta}{d/l_s})^{0.33}$	(4.5)	0.49
$\frac{\eta_{max,n}}{d} = 0.049 \times (\frac{V/d^3 . \sin\theta}{d/l_s})$	(4.6)	0.59
$\frac{\eta_{max,n}}{d} = 0.0080 \times \frac{(V/d^3)^{0.295} \times \sin\theta^{1.650}}{(d/h)^{1.095}}$	(4.7)	0.34
$\frac{\eta_{max,n}}{d} = 0.032 \times (\frac{V/d^3 . \sin\theta}{d/h})^{0.39}$	(4.8)	0.37
$\frac{\eta_{max,n}}{d} = 0.0024 \times (\frac{V/d^3 . \sin\theta}{d/h})$	(4.9)	0.50
$\frac{\eta_{max,n}}{d} = 0.014 \times \frac{(V/l_s d^2)^{0.295} \times \sin\theta^{1.650}}{(d/h)^{1.095}}$	(4.10)	0.35
$\frac{\eta_{max,n}}{d} = 0.06 \times (\frac{V/l_s d^2 . \sin\theta}{d/h})^{0.395}$	(4.11)	0.45
$\frac{\eta_{max,n}}{d} = 0.016 \times (\frac{V/d^3 . \sin\theta}{d/l_s})$	(4.12)	0.49
$\frac{\eta_{max,n}}{d} = 0.048 \times \frac{(V/l_s d^2)^{0.295} \times \sin\theta^{1.650}}{(d/l_s)^{1.095}}$	(4.13)	0.19
$\frac{\eta_{max,n}}{d} = 0.027 \times (\frac{V/l_s d^2 . \sin\theta}{d/l_s})^{0.68}$	(4.14)	0.41
$\frac{\eta_{max,n}}{d} = 0.066 \times (\frac{V/l_s d^2 . \sin\theta}{d/l_s})$	(4.15)	0.49
$\frac{\eta_{max,n}}{d} = 0.037 \times \frac{(m_b/\rho_w l_s d^2)^{0.295} \times \sin\theta^{1.650}}{(d/l_s)^{1.095}}$	(4.16)	0.64
$\frac{\eta_{max,n}}{d} = 0.129 \times \frac{(m_b/\rho_w l_s d^2)^{0.295} \times \sin\theta^{1.650}}{(d/h)^{1.095}}$	(4.17)	0.40

[*] Based on Eq. (3.6).

The structures of Eqs. (4.4), (4.7), (10) and (4.13) are influenced by equations for individual parameters (Figures 4.1 and 4.2 in the Section), and the structures of Eqs. (4.5), (4.8), (4.11) and (4.12).

(4.14) are based on our judgements. The format of a prior equation by Murty (2003) was adopted for Eqs. (4.6), (4.9), (4.12), and (4.15), while the two Eqs. (4.16) and (4.17) were inspired by Heller and Spinneken (2015). These equations were developed using three sets of accessible experimental data (Watts 1998; Enet and Grilli, 2007; Najafi-Jilani and Ataie-Ashtiani, 2008), this study's experimental data (Figures 3.3 and 3.4), and some field data from previous real-world landslide tsunami events (Table 4.2).

Table 4.2. Data of real-world landslide tsunamis used here to derive the predictive equations.

Event name	Slide volume (km^3)	Initial submergence depth (m)	Water depth (m)	Slide length (m)	Slope angle (^{0})	Reference
1975 Kitimat (Canada)	0.023	80-120	160-180	274-1000	11	Murty (1979); Kirby et al. (2015)
1979 Nice (France)	0.0022	47	50-100	346-652	11	Murty (2003); Dan et al. (2007)
1994 Skagway (USA)	0.0032	26-40	55-72	180-600	17.5	Watts et al. (2003); Rabinovich et al. (1999)
1999 Izmit (Turkey)	0.0052	25	55	140-160	15	Tinti et al. (2006)

The *NRMSE* index is used to compare these 14 equations (Eq. 3.6). Among the equations listed in Table 4.1, Eq. (4.13) has the lowest *NRMSE*, indicating a better agreement between calculations and observations (Table 4, last column). The performance of the derived equations (Eqs. 4.4 – 4.17) is shown by comparing the calculated maximum negative initial wave amplitude using various equations (η_{max,n_cal}) and the observed experimental and field data (η_{max,n_obs}) (Figure 4.3). For both experimental and field data, Equation (4.13) was predicted $\eta_{max,n}$ with acceptable exactness (i.e., *NRMSE* of 0.2). (Figure 4.3).

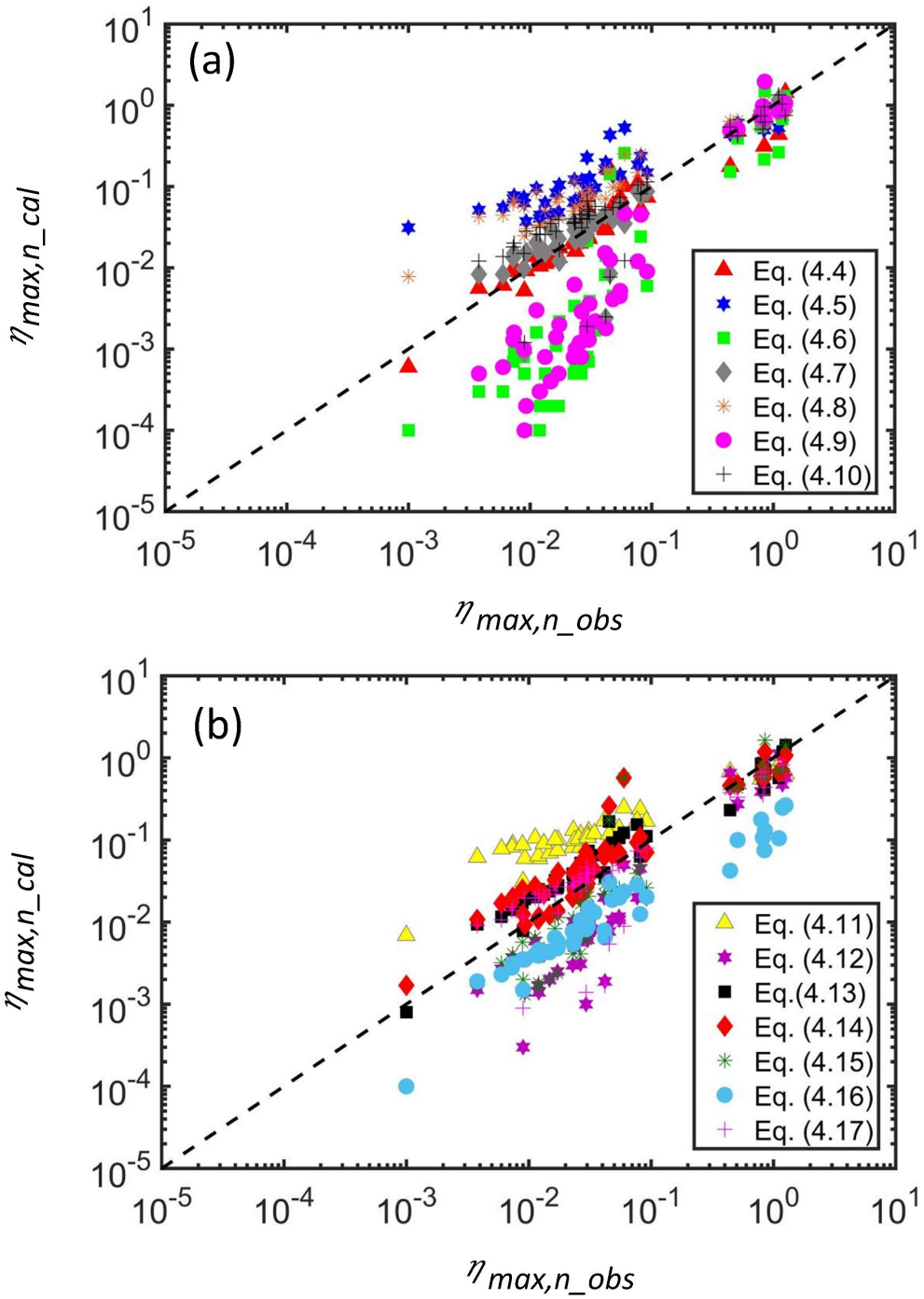

Figure 4.3. Difference of field and experimental data (η_{max,n_obs}) with predictions from various predictive equations (η_{max,n_cal}) for (a) Eqs. 4.4 - 4.10 and (b) Eqs-4.11 - 4.17. (See Table 4.1 for Eqs. 4.4 – 4.17).

To assess the performance of Eq. (4.13), it was applied to three previous landslide tsunami events whose data were not used in the development of this equation (Table 4.3; the events of 2018 Palu, 2013 Pakistan and 1998 PNG). The observed values (Table 4.3; column 7) were the initial wave amplitudes

on the top of the landslide locations (Figure 3.1), which were numerically estimated by Synolakis et al. (2002) for the PNG and Pakistan events, respectively.

Table 4.3. Testing of the developed predictive equation (Eq. 4.13) to three actual landslide events whose data were not used for deriving Eq. (4.13).

Event name	V_s (km^3)	d (m)	Slope angle (^{0})	h (m)	Slide length (m)	η_{obs} (m)	η_{cal} (m) using Eq. (4.13)	References
2018 Palu	0.09	800	10-16	850	1500	9.7	7.4	Frederik et al. (2019); Watts et al. (2005)
2013 Makran (Pakistan)	2.2-3.0	1500-2000	2	2500-3000	10,000-15,000	1.5-2.0	1.0-1.8	Heidarzadeh and Satake (2017)
1998 PNG	4.0-7.0	1000-2000	5-15	2000-3000	3000-7000	11-16	2.0-44.3	Tappin et al. (2008); Synolakis et al. (2002)

The maximum initial wave for the 2018 Palu event was estimated using the bathymetric survey of Frederik et al. (2019), empirical equations of Watts et al (2005), and the study by Heidarzadeh et al. (2019). The results in Table 4.3 showed a relatively good agreement between the calculated values and the observed data using Eq. (4.13). The average prediction errors were 70%, 20%, and 24% for the 1998, 2013 and 2018 events, respectively, indicating that the observations and calculations were in the same range for the 2013 and 2018 events, while the equation was overestimated for the 1998 event. Prior to this study, estimates for $\eta_{max,n}$from existing equations were divided by a few orders of magnitudes (factors of thousands) from actual observation data as discussed in earlier chapters. Although Eq. (4.13) predictions had some errors, it was a step forward in estimating the maximum amplitudes of the landslide generated waves. This improvement could be attributed to the use of both experimental and field data in this study when developing the new predictive equations.

4.2: Results of numerical simulation of submarine landslide (wave amplitude)

In this section a total of 177 simulations were conducted using the validated model and three different sliding block sizes (Solid-block-2, Solid-block-3, Solid-block-4; Table 3.2). The following landslide parameters, which determine wave amplitudes, were examined in these simulations: submergence depth (d), landslide volume (V), water depth (h), and travel distance (S) (Figure. 3.1). The slope angle (θ) was another essential element; however, in this study, a fixed slope angle of 45^o was employed to limit the scope of this work. The simulations were divided into two categories: those with changing submergence depth (d) and constant travel distance (S), and those with varied travel distance but constant d.

A total of 156 simulations were run to investigate the influence of submergence depth on $\eta_{max,n}$; each of the three blocks was examined for 52 different submergence depths (Figure. 4.4).

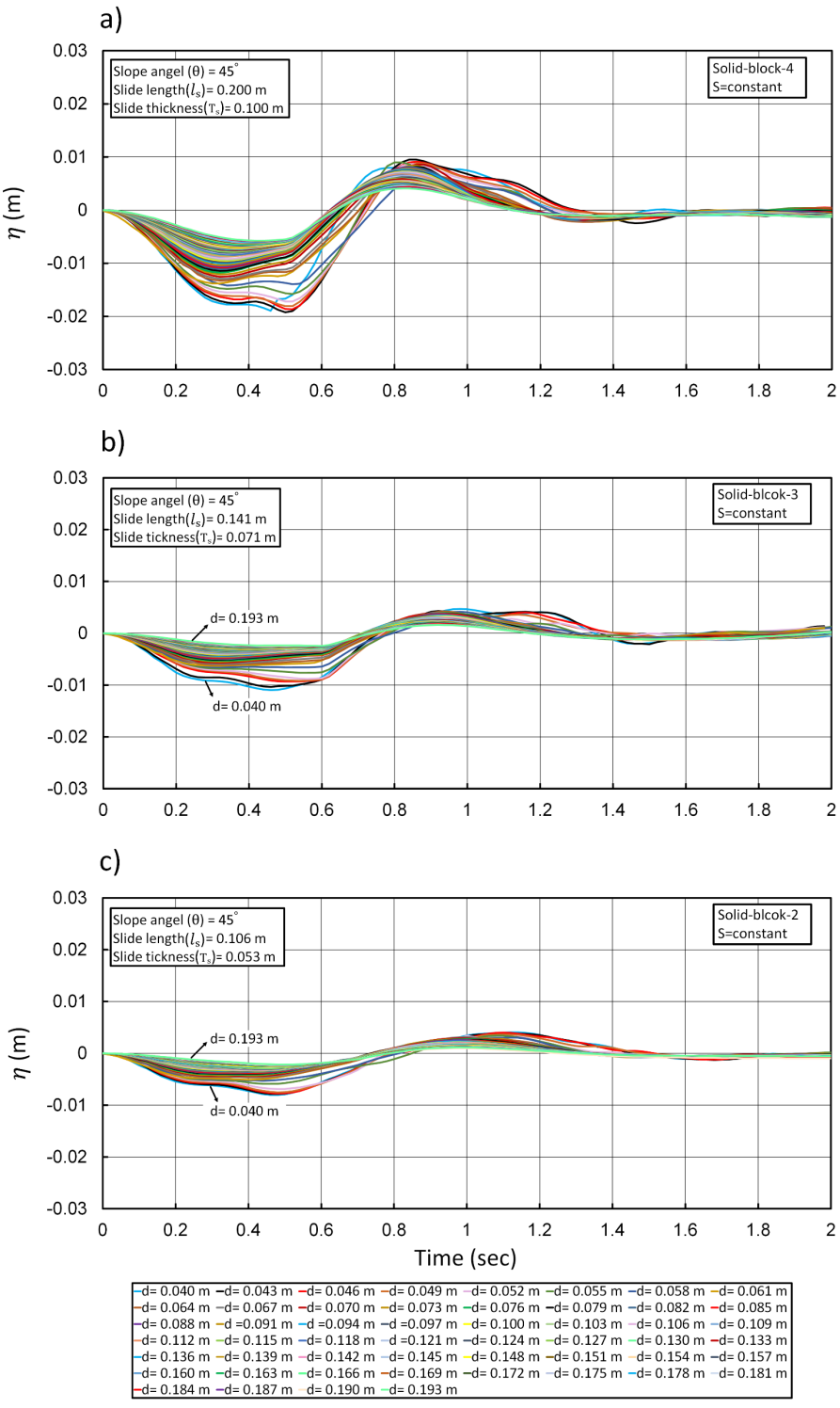

Figure 4.4. Waveform and wave amplitude (η) sensitivity to different submergence depths, d, for three blocks, Solid-block-4 (a), Solid-block-3 (b), and Solid-block-2 (c). The dimensions of the blocks are shown in Table 3.2. The travel distance (S) is maintained constant in these simulations.

In these modelling, the submergence depth (d) was changed between 0.04 and 0.193 m while the travel distance remained fixed. Also, the water level (h) was changed in this example to provide changing submergence depth while the travel distance remained constant. It is obvious that water depth influences the results, although its effects are expected to be lower than those of submergence depth, as previously demonstrated by Watts et al (2005). As predicted, there is an inverse relationship between maximum initial wave amplitude ($\eta_{max,n}$) and submergence depth (Figure 4.4). The various simulations shown in Figure 4.4 show that the maximum negative initial amplitude changes more than the maximum positive initial amplitude. For example, in the case of the solid-block-4 (Figure 4.4a), the greatest negative initial amplitude is in the range of 0.005 0.019 m, whereas the highest positive initial amplitude is from 0.004 m to 0.009 m. The other two blocks (solid-block-3 and solid-block-2) follow the same pattern (Figures. 4.4b, c). A comparison of the waveforms from the three sliding blocks also shows that ($\eta_{max,n}$) grows as the volume of the blocks increases, which was previously observed (e.g. Watts, 1998; Murty, 2003). For example, the solid-block-4's ($\eta_{max,n}$) is 2.4 times more than the solid-block-2. The period of the landslide-generated wave (i.e. the time duration of a full cycle of the wave) appears to rise as the landslide volume diminishes, which appears to be unexpected. The dominating wave durations for the solid-block-4 and small solid-block-2 are 0.70 s and 1.1 s, respectively, according to spectral analysis of the waveforms (Figure 4.5). In general, the greater the landslide, the longer the duration of the created wave, assuming all other factors remain constant. However, in this investigation of landslide-generated waves, this is not the case, most likely due to the impact of landslide velocity.

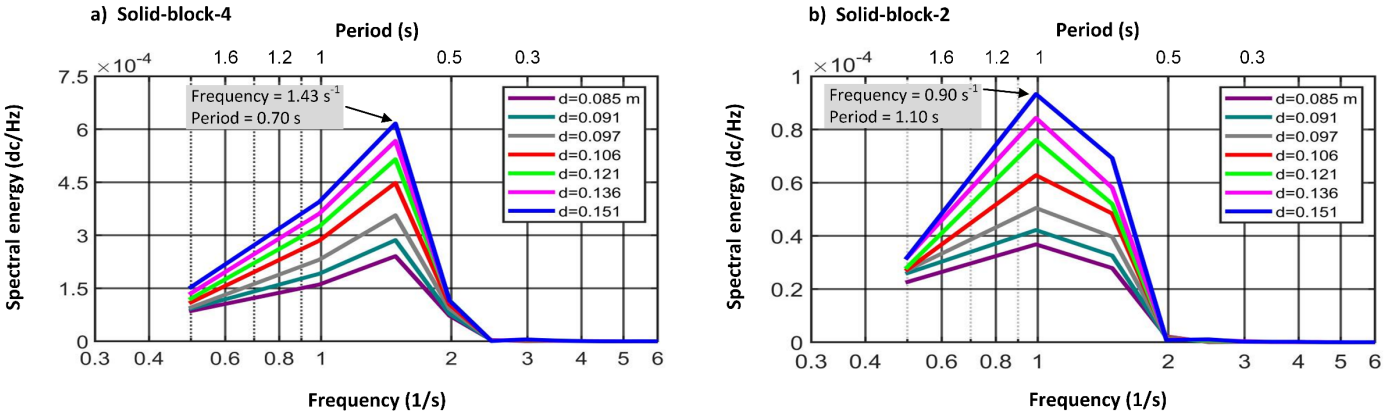

Figure 4.5. Spectral study of the waveforms for Solid-block-4 (a) and Solid-block-2 (b). The letter "d" stands for the depth of initial submergence. The dimensions of the blocks are shown in Table 3.2.

The dimensionless submergence depth ($^{d}/_{l_s}$) versus dimensionless maximal initial amplitude ($\eta_{max,n}$ / l_s) was plotted to evaluate the effects of submergence depth (d) on ($\eta_{max,n}$), as illustrated in Figure 4.6. The slide length is given by l_s. Previous study by Watts et al. (2003) and Grilli and Watts (2005) demonstrated that ($\eta_{max,n}$) is substantially impacted by d. It should be highlighted that the goal here is to understand the relationship between the two factors rather than to build an equation. Based on a power regression analysis using the nonlinear least squares regression approach (MathWorks, 2020), a nonlinear inverse connection between the two parameters is detected as follows:

$$\frac{\eta_{max,n}}{l_s} \propto \left(\frac{d}{l_s}\right)^{-0.772} \tag{4.18}$$

Relationship (4.18) is applicable for following condition: $\theta = 45^{o}$ and $d/l_s \in [0.20, 1.82]$. The experimental study of Watts (1997) (WTS-97) was plotted for $^{\eta_{max,n}}/_{l_s}$ versus $^{d}/_{l_s}$. This study demonstrates that the numerical results are mostly consistent with the experimental efforts, but somewhat diverged. The accuracy of regression analysis, generally reported as R^2 (the index of quality of regression line fitting to the data point) which is 0.96 for Relationship (4.18). To predict the $\eta_{max,n}$, the Relationship (4.18) may not be applied; rather, it is intended to demonstrate the link between ($\eta_{max,n}$) and d.

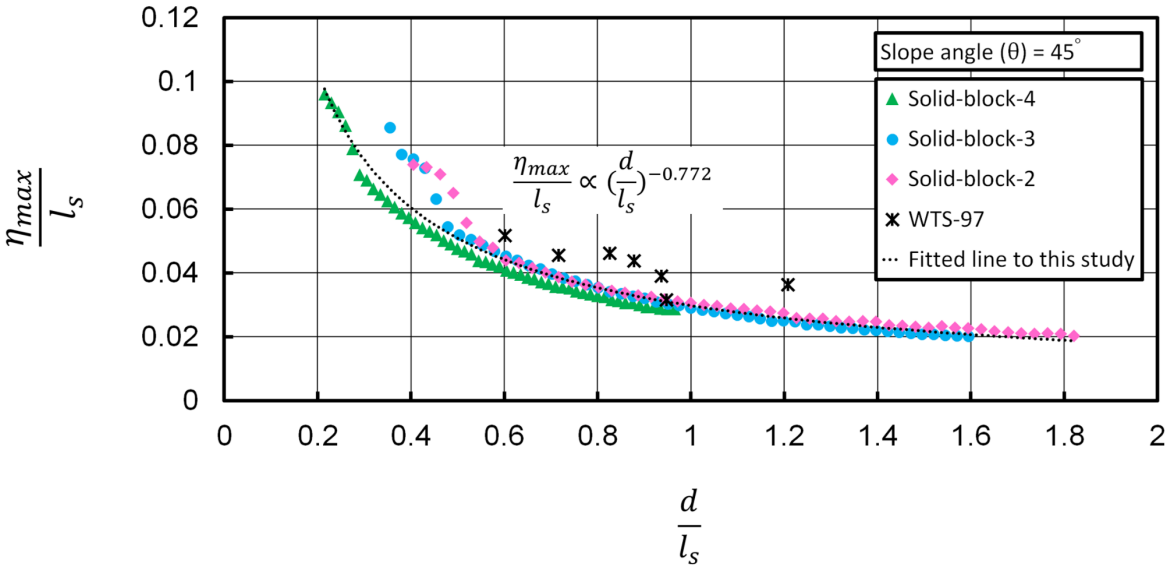

Figure 4.6. Relationship of nondimensional maximum wave amplitude ($^{\eta_{max,n}}/_{l_s}$) vs nondimensional submergence depth ($^{d}/_{l_s}$) for simulations with different submergence depth (d) and constant travel distance. The black asterisks represent Watts experiment data (1997). For block dimensions, refer to Table 3.2.

Figure 4.7 depicts simulated waveforms with varied travel distance (S) and constant d to study the influence of (S) on maximum initial wave amplitude ($\eta_{max,n}$). Seven travel distances were investigated for each block, while the submergence depth was kept constant across all simulations at d = 0.08 m. In total, 21 simulations were run. The results reveal that travel distance has a considerable influence on $\eta_{max,n}$, with an inverse relationship between the two parameters: the shorter the travel distance, the larger the wave amplitude. For example, by reducing travel distance from 0.308 m to 0.223 m, ($\eta_{max,n}$) of the Solid-block-3 was enhanced from 0.005 m to 0.008 m (Figure 4.7b). The first wave generates a free surface with a large negative phase followed by a smaller elevation phase. Because each block had a varied length (l_s) (Table 3.2), the range of travel distance was different for each example. The larger the solid block volume, the greater the maximum initial wave amplitude (Wiegle, 1955). Figure 4.7 shows that the range of ($\eta_{max,n}$) varies from 0.004 m to 0.006 m for the Solid-block-2 and from 0.011 m to 0.016 m for the Solid-block-4.

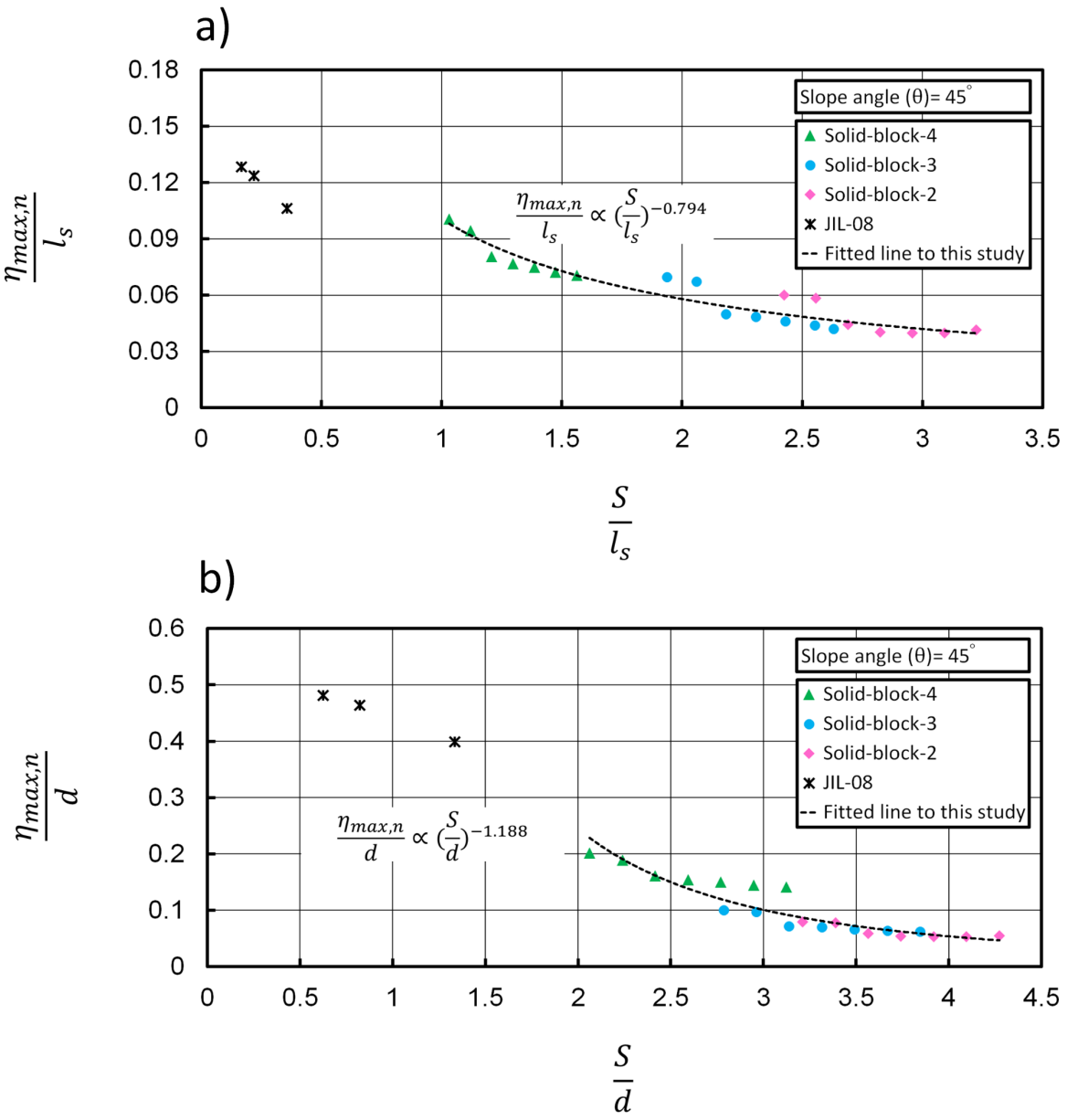

Figure 4.7. Correlation between dimensionless maximum negative initial wave amplitude ($^{\eta_{max,n}}/_{l_s}$) and dimensionless travel distance ($^{S}/_{l_s}$) for simulations with varying travel distance (S) and constant submergence depth. b) Same as "a" but for the correlation between $^{\eta_{max,n}}/_{d}$ and $^{S}/_{d}$. The black asterisks are experimental data from Najafi-Jilani and Ataie-Ashtiani (2008).

To determine a relationship between the travel distance (S) and $\eta_{max,n}$ a regression analysis was applied which benefits from non-linear least square method (MathWorks, 2020) (Figure 4.8). Parameters S and $\eta_{max,n}$ were made dimensionless by landslide length (l_s) and submergence depth (d).

Landslide length (l_s) and submergence depth (d) were employed to make S and $\eta_{max,n}$ dimensionless. A few data points from Najafi-Jilani and Ataie-Ashtiani (2008) (JIL-08) physical experiments were added to this study simulation-based graphs (Figure 4.8). These experimental data were added just for comparison and were not employed in the regression analyses. Although there were minor differences, this study's models and JIL-08 experiments showed a similar pattern. The following relationships were derived between $\eta_{max,n}/l_s$ and S/l_s, and between $\eta_{max,n}/d$ and S/d:

$$\frac{\eta_{max,n}}{B} \propto \left(\frac{S}{l_s}\right)^{-0.794} \tag{4.19}$$

$$\frac{\eta_{max,n}}{d} \propto \left(\frac{S}{d}\right)^{-1.188} \tag{4.20}$$

Relationship (4.19) is applicable only for following range: $S/l_s \in [0.82, 3.22]$. For Relationship (4.20), the range is: $S/d \in [0.82, 3.22]$. For both, a constant slope angle of $\theta = 45^{o}$ is used. The accuracy of regression (R^2), for Relationships (4.19) and (4.20) are 0.89 and 0.86 respectively.

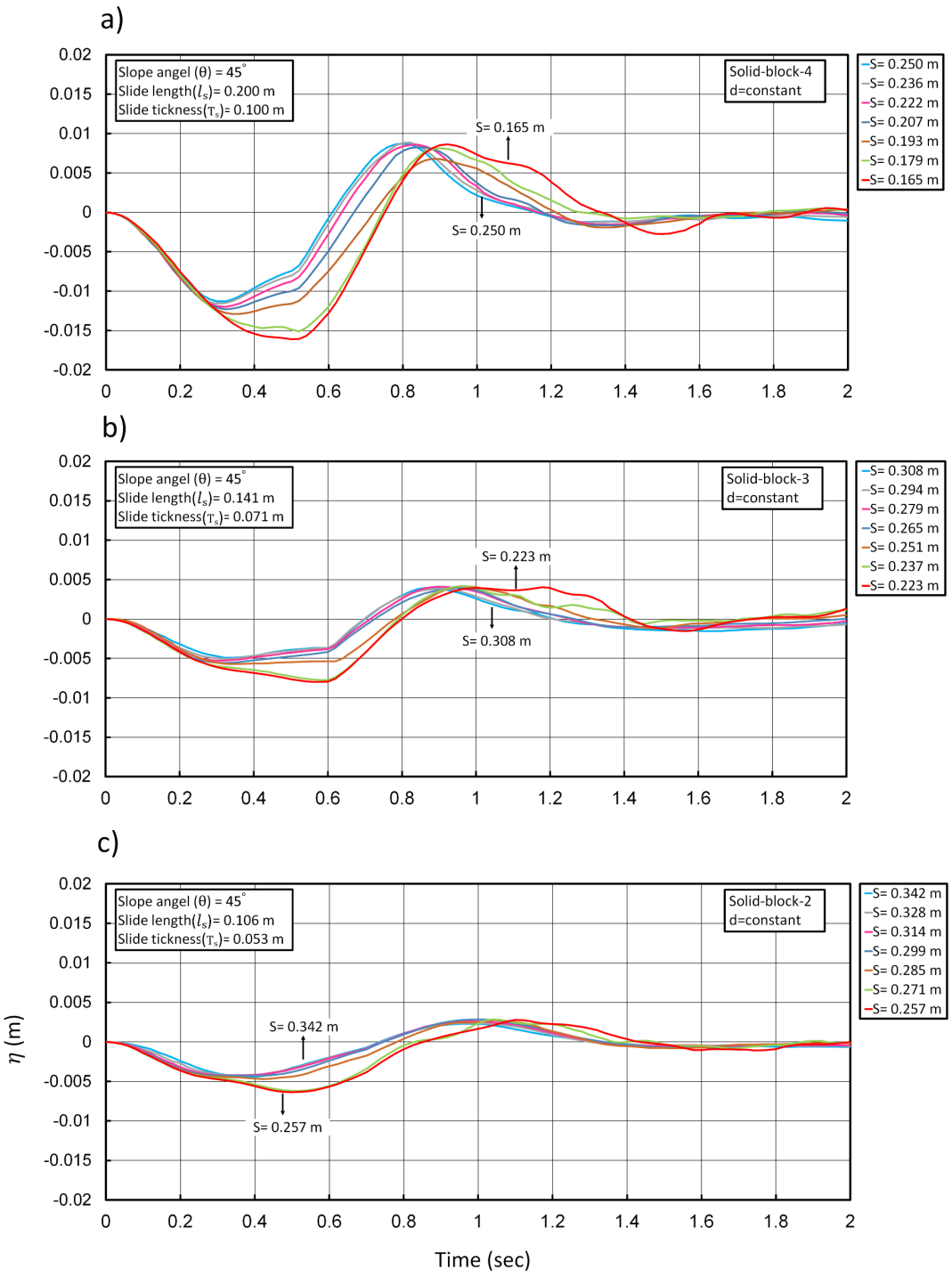

Figure 4.8. The Sensitivity of waveforms and wave amplitude (η) to variations of travel distance (S) for three different block sizes of large (a), medium (b), and small (c). See Table 1 for block dimensions. In these simulations, the submergence depth, d, is kept constant.

Figures 4.9 and 4.10 for the solid-block-4 and solid-block-2, respectively, illustrate a sequence of three velocity vector graphs at different periods during landslide motion. The vector's direction indicates the flow direction, and the length of the vectors indicates the magnitude of the velocity (Figures 4.9-4.10). Throughout this image sequence, a complicated flow pattern involving outward, inward, and upward flows of water is observed. Inward and upward flows combine to generate a circling flow pattern or eddies around the top side of the block (Figures 4.9 – 4.10). A prior investigation on subaerial landslides by Fritz et al. (2004) revealed that such circulating flow is not caused by subaerial mass motions. The solid-block-4 sequence begins at t= 0.060 s after the first landslide motion (Figure 4.9a) and continues with a time step of 0.2 s across a time period of about 5 s (Figure 4.9). The high-water pressure in front of the block forces the water to rise to the surface, forming a crest (Figure 4.9c). At t= 0.060 s, the wave amplitude increases in elevation at the start of the slide motion (Figure 4.9a). This increases until the maximum initial wave amplitude is reached at t= 0.42 s (Figure. 4.9c). As previously reported by Fritz et al., the highest particle velocity recorded in the wave field occurs below a formed wave trough when the block approaches the end of the slope (v= 0.88 m/s; Figure 4.9c) (2009). The maximum water particle velocity (0.88 m/s) is nearly the same magnitude as the maximum landslide velocity (i.e. velocity of the solid block) obtained in laboratory studies. In comparison to the solid-block-4, the solid-block-2 (Figure 4.10) has a lower maximum water particle velocity (v= 0.688 m/s) and a lower maximum initial landslide amplitude (Figure 4.9c and Figure 4.10c).

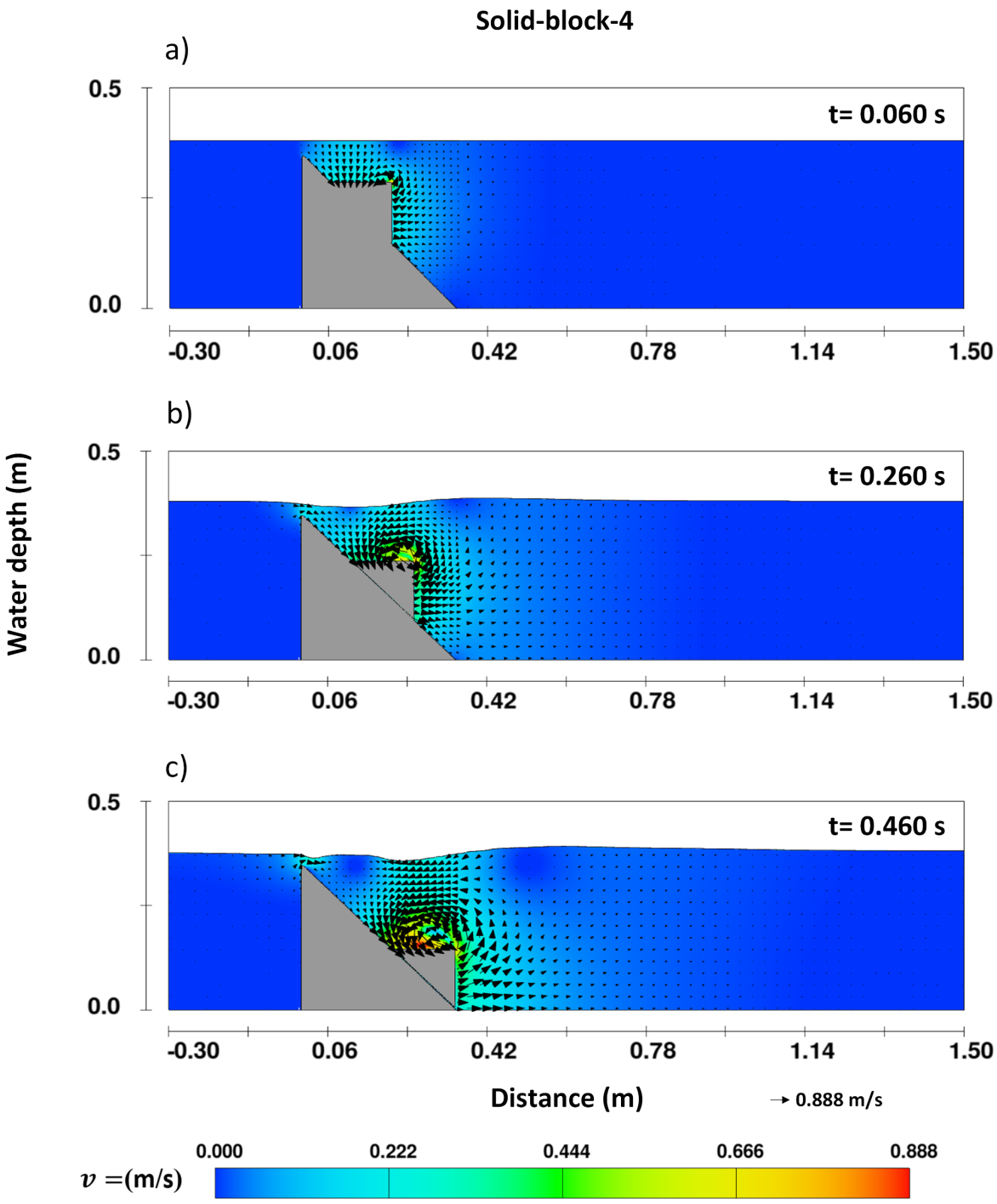

Figure 4.9. Velocity field at different times around the source region as the solid block is moving down the slope for the Solid-block-4 at different times of 0.060 s (a), 0.260 s (b), 0.460 s (c). Dimensions of the block are given in Table 3.2. Velocity magnitude scale is given in this figure.

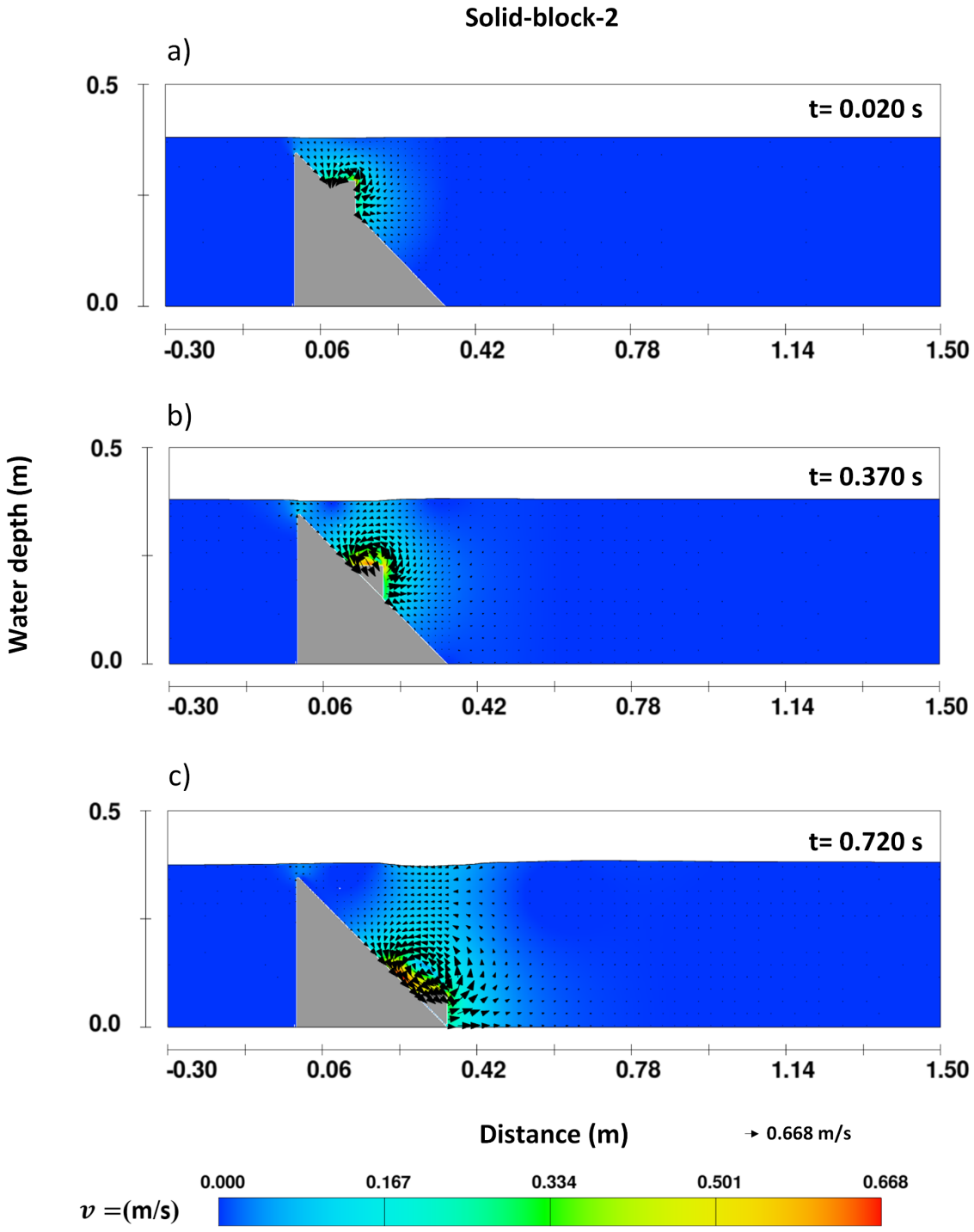

Figure 4.10. Velocity field at different times around the source region as the solid block is moving down the slope for the Solid-block-2 at different times of 0.020 s (a), 0.370 s (b), 0.720 s (c). Dimensions of the block are given in Table 3.2. Velocity magnitude scale is given in this figure.

4.3: Results of numerical simulation of subaerial landslide (wave amplitude)

The verified numerical model was used to simulate subaerial landslide-generated waves produced by two types of slides, solid-block and granular. The sensitivity of wave amplitudes to four major landslide factors was investigated: water depth (h), landslide volume (V), slope angle (θ), and landslide thickness (T_s). Previous research has shown that the aforementioned parameters have the greatest influence on the landslide-generated waves (Kamphuis and Bowering, 1970; Heller and Hager, 2014). For all of these simulations, the travel distance (D) was kept constant. The results are discussed in sub-sections below.

To explore the effect of water depth (h) on Maximum positive initial wave amplitude (a_M), h was changed for solid-block and granular landslides from 0.150 m to 0.246 m. (Figure 4.11). For this series of tests, the slope angle, slide volume, and travel distance were held constant (i.e. θ=45^o, D=0.02 m and V=2.60×10^{-3} m^3) (Figure 4.11). To minimise scale influences on the given models, the water depth was adjusted to larger than 0.150 m, which is close to the criterion proposed by Heller et al. (2008). According to the data, as previously reported by other scientists, the maximum amplitude of both types of landslides increases as water depth drops (Zweifel et al., 2006; Oppikofer et al., 2019). The lowest water depth produced the highest a_M value for solid-block landslides (a_M=0.086 m at h=150 m). Another important discovery was that the greatest amplitude generated by solid blocks is about twice as high as that produced by granular materials. For example, at the same water depth of 0.240 m, a_M=0.07 m is achieved for a solid-block slide and a_M=0.036 m for a granular slide (Figure 4.11b). Once all maximum amplitudes from solid-block and granular slides were compared, it was discovered that maximum amplitudes created by solid-block slides are nearly 92% bigger on average than those produced by granular slides. In the presented experiments, spectral examinations of the waveforms revealed that the wave period remained roughly the same for both solid-block and granular landslides (Figure 4.11c).

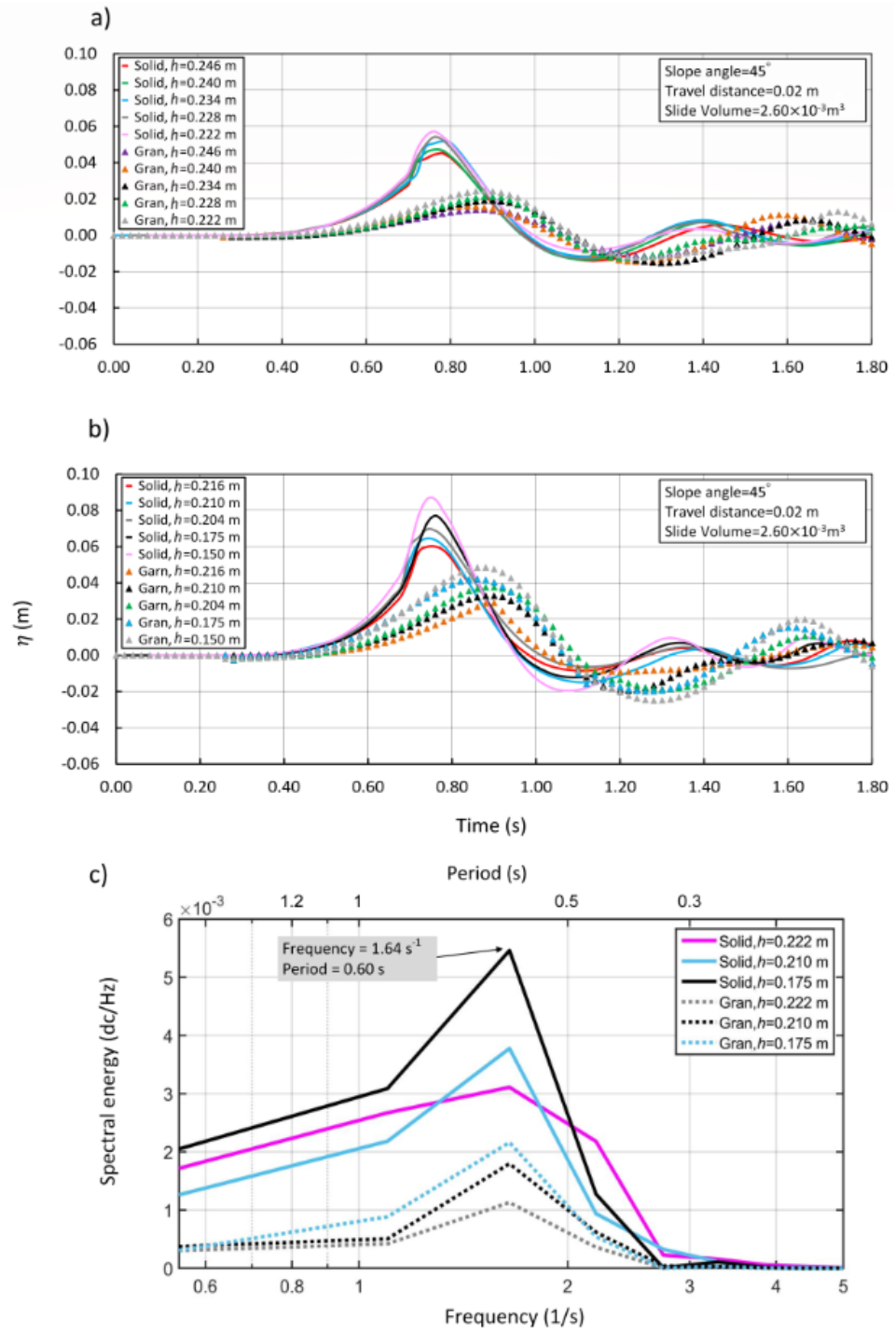

Figure 4.11. (a) Waveforms of landslide-generated waves for solid-block (solid lines) and granular (broken lines) landslides for varying water depths in the range of h=0.222 – 0.246 m. (b) Same as 'a' but for water depths of h=0.150 – 0.216 m. (c) Spectra for a few of the waveforms. "Solid" and "Gran" in the legends represent solid-block and granular landslides. η is wave amplitude.

A series of simulations were carried out to investigate the effect of slide volume (V) on wave amplitudes and waveforms. Figure 12 depicts the simulated waveforms for various volumes ranging

from 0.70×10^{-3}– 2.60×10^{-3} m^3. For this series of analyses, the slope angle, water depth, and travel distance were held constant (i.e. α=45°, h=0.246 m and D=0.02 m) (Figure 4.12). The results showed that raising the V increases the Maximum positive initial wave amplitude for both solid blocks and granular landslides, which was consistent with previous research (e.g., Kamphuis and Bowering, 1970; Wang et al., 2017). The largest solid block (Solid-block-4) (Table 3.2) (V=2.60×10^{-3} m^3) had the highest Maximum positive initial wave amplitude (a_M=0.045 m). Furthermore, given the same slide volume, the highest amplitudes created by solid blocks are nearly twice as large as those generated by granular materials. The maximum amplitudes of solid-block slides were 121% greater than those of granular slides on average. As indicated by these spectral analyses, the wave period was remained nearly unchanged for both solid-block and granular landslides (Figure 4.12c), similar to the influence of water depth discussed in the previous analysis (Figure 4.11c).

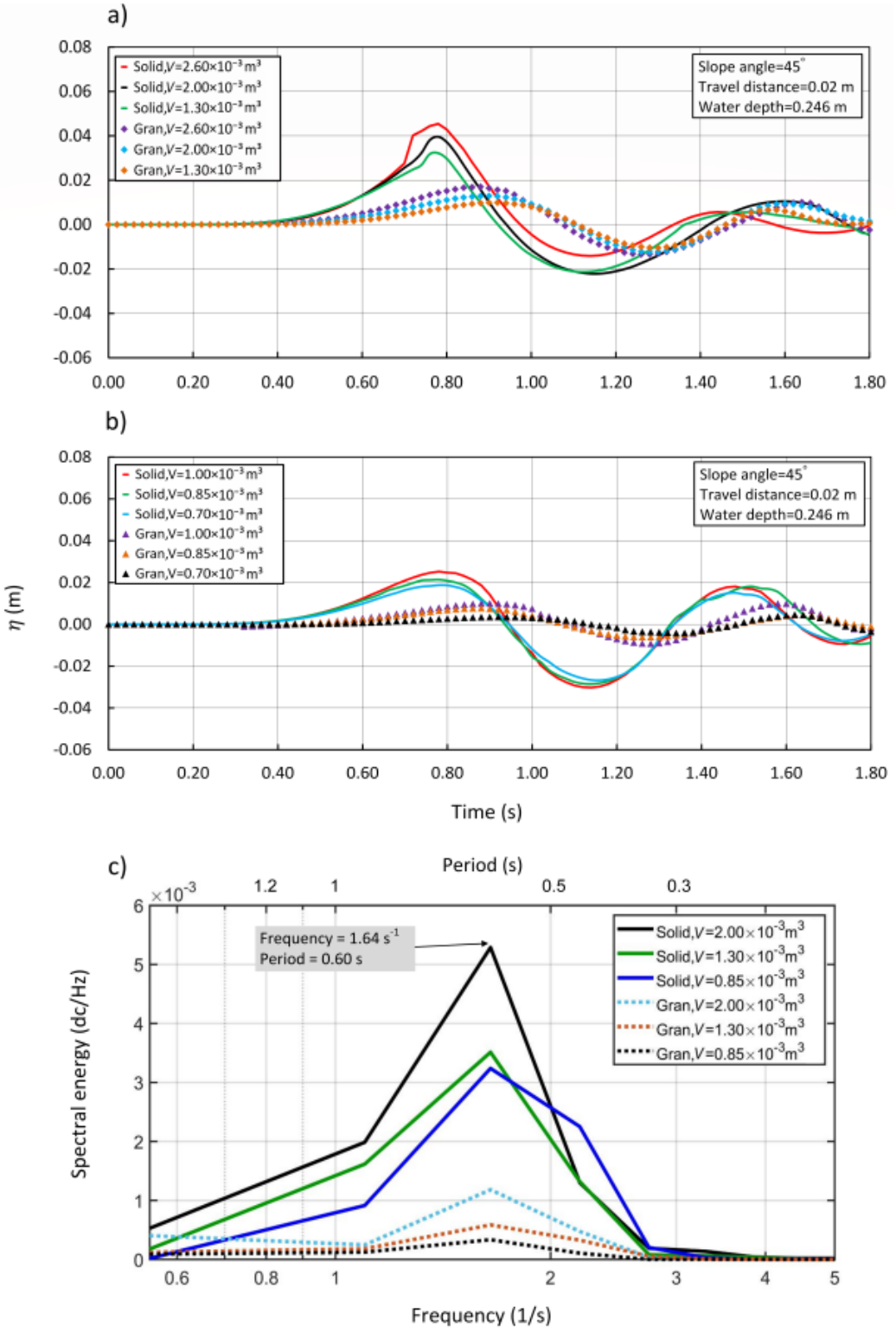

Figure 4.12. (a) Waveforms for solid-block (solid lines) and granular (broken lines) landslides for different slide volumes in the range of V=1.30×10^{-3} – 2.60×10^{-12} m^3. (b) Same as 'a' but for slide volumes V=0.70×10^{-3}– 1.00×10^{-3} m^3. (c) Spectra for some of the waveforms. "Solid" and "Gran" in the legends in the legends stand for solid-block and granular landslides.

By varying slope angles (30°–60°) for both types of landslides, the effect of slope angle on wave amplitude was investigated (Figure 4.13). For this series of simulations, the water depth, travel distance, and slide volume were all kept constant (i.e., h=0.246 m, D=0.02 m and V=2.60×10^{-3} m^3). The results of simulations for solid-block landslides demonstrated a linear relationship between slope angle and a a_M, as the slope angle increased, the maximum wave amplitude decreased (Figure 4.13). The horizontal component of the landslide gravity-driven force exerted on the water body was relatively larger on gentle slopes than on steeper slopes; it should be noted that this observation is valid in the slope angle range of 30° – 60° in these study tests. For granular slides, increasing the slope angle causes an increase in wave amplitude until a critical slope angle was reached, after which the amplitude begins to decline (Figure 4.13). In terms of wave period, a drop was noticed as the slope angle increased for solid-block slides, with the wave period decreasing from 0.91 s to 0.60 s as the slope angle grew from 30°–40° to 55°–65 °. (Figure 4.13c). Surprisingly, the wave period for granular slides was remained constant across all slope angles (Figure 4.13c).

According to Figure 4.14, the critical slope angle is 60°. This finding was consistent with Tang et al. (2018) and Heller and Hager's earlier laboratory investigations (2014). The critical angle was affected by grain size, material density, and bed friction angle (Tang et al., 2018). Heller and Hager (2014) reported critical slope angles ranging from 39.1°–65.1° for several granular sliding scenarios. It is still difficult to explain the mechanics underpinning the formation of a critical slope angle for granular slopes.

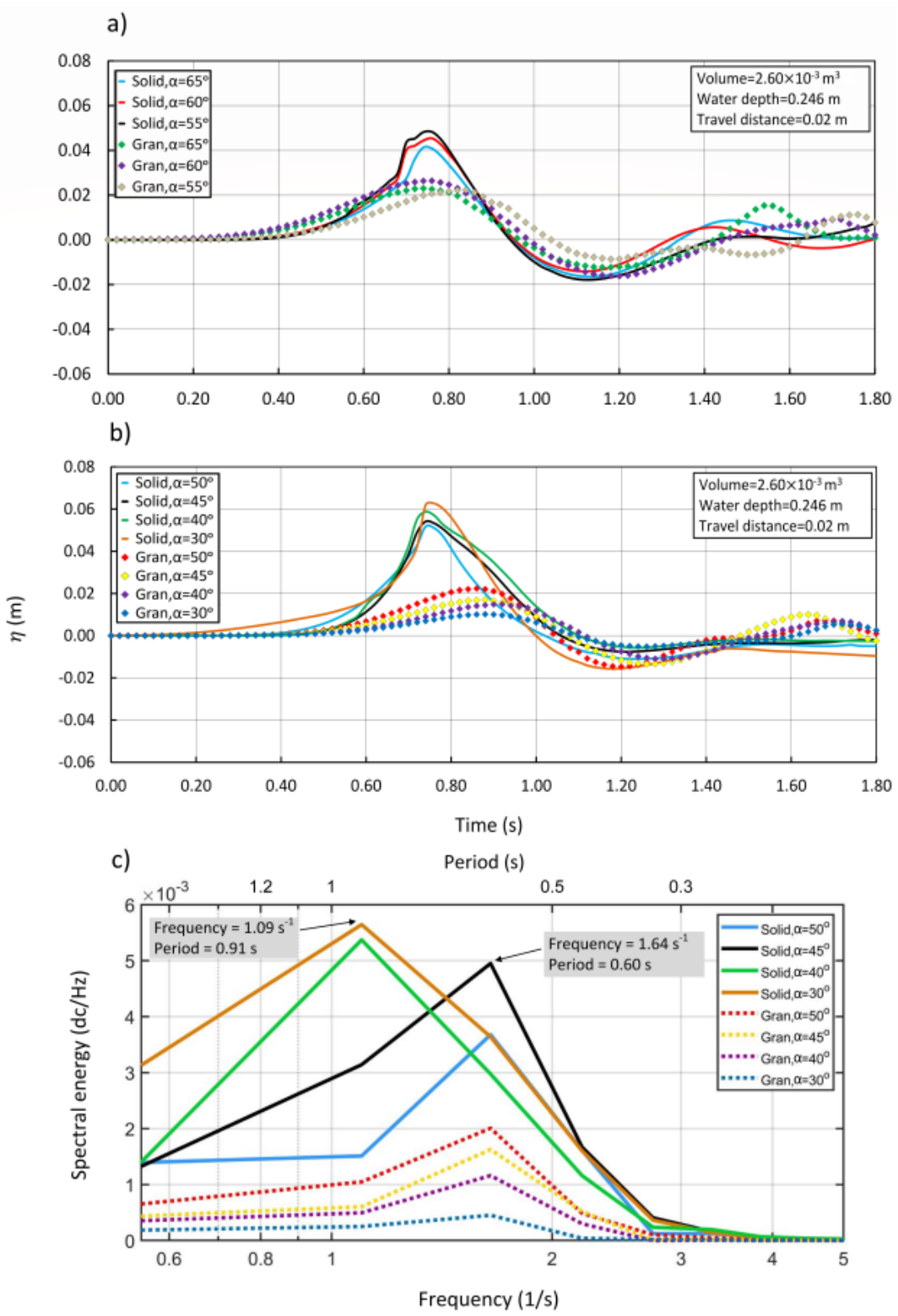

Figure 4.13. (a) Waveforms for granular (broken lines) and solid-block (solid lines) landslides for different slope angles θ= 55º–65º. (b) Same as 'a' but for slope angles θ= 30º– 50º. (c) Spectra for some of the waveforms. "Solid" and "Gran" in the legends in the legends stand for solid-block and granular landslides.

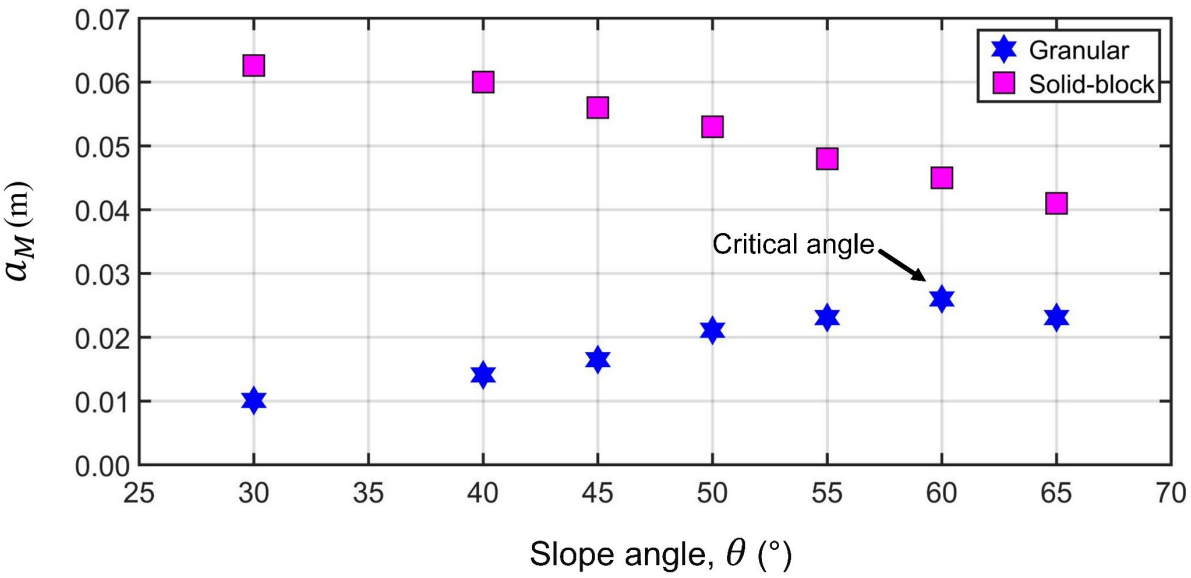

Figure 4.14. Comparing of maximum wave amplitude (a_M) versus slope angle for granular (solid stars) slides and solid-block (solid squares).

To investigate the influence of friction coefficient on maximum initial wave amplitude (a_M), the f was varied between 0.30 and 0.55. (Figure 4.15). This range was comparable with recent reports on dynamic bed friction angle values of 20° – 30° (Mohammed and Fritz, 2012; Lindstrom, 2016; McFall and Fritz, 2016). The results showed that the friction coefficient had slight effect on a_M for both types of landslides (i.e., solid-block, and granular slide). According to Figure 4.15, variations in the friction coefficient in the range of f = 0.30 – 0.55 alter the maximum wave amplitudes by less than 14%.

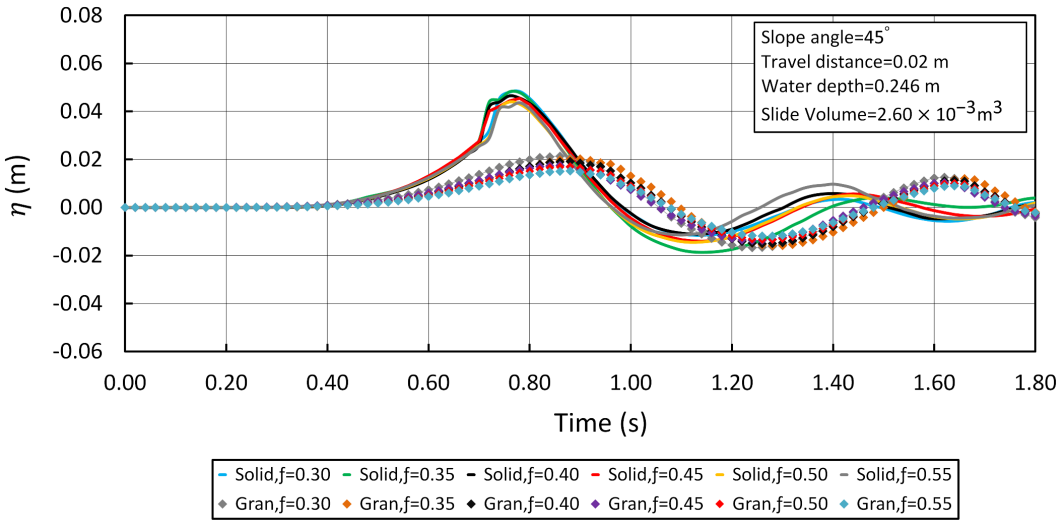

Figure 4.15. The impact of friction coefficient (f= 0.30 – 0.55) on the waveforms and amplitudes of landslide-generated waves for solid-block (solid lines) and granular (broken lines). "Solid" and "Gran" stand for solid-block and granular landslides, respectively.

Figure 4.16 depicts a series of three water particle velocity plots taken at various time during landslide motion. The direction and length of the arrows show the velocity direction and magnitude (Figure 4.16). A complex wave field formed by inward and upward flows emerges around the landslide generation area, explaining the splashing of water and mixing with the air around the source zone (Figure 4.16). The sequence of solid-block landslides was begun at t=0.180 s after landslide impact and included two further snapshots at 0.34 s and 0.48 s following the landslide's onset (Figure 4.16 a–c). The landslide front profile in the numerical image of Figure 10d for the granular landslide was practically vertical as the materials begin to enter the water, followed by a transition from rigid to fluid motion. The results in Figure 4.16 showed that the highest velocity magnitude related to solid-lock landslides was1.62 m/s for a landslide in a water depth of 0.246 m, a slope angle of 45°, and a slide volume of 2.6010-3 m^3, whereas it is 0.92 m/s for granular materials. This discrepancy in wave velocity magnitude could be attributed to granular slides deforming, whereas solid-block slides do not deform. For solid-block landslides with slide volumes ranging from 0.70×10^{-3} m^3 to 2.60×10^{-3} m^3 (Table 3.6), the maximum water particle velocity ranged from 0.98 m/s to 1.62 m/s. For granular slides, this velocity ranged from 0.68 m/s to 0.92 m/s.

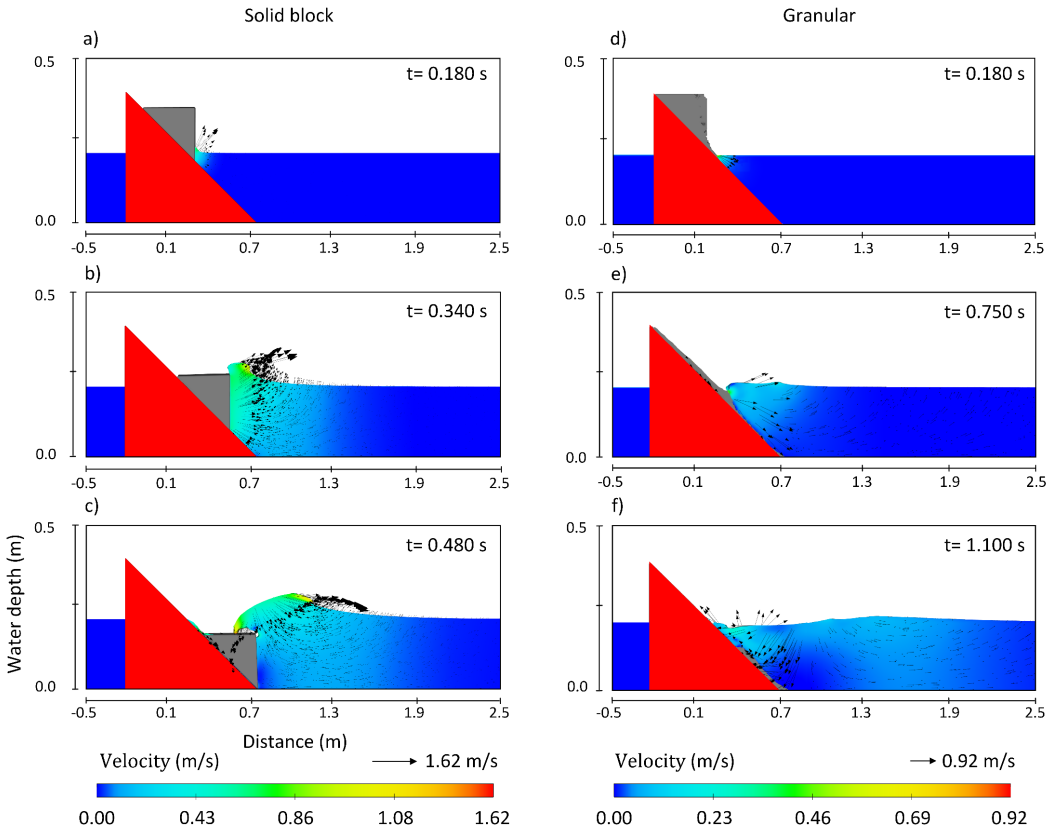

Figure 4.16. Snapshots of simulations at different times for solid-block (a, b, and c) and granular landslides (d, e, and f), with particle velocity indicated by colours and arrows. The colormaps indicate the velocity of water particles in metres per second, and the arrows represent the directions and magnitudes of the velocity.

A combination of previously published experimental data and numerical data of this study (50 simulations) were used to build two novel predictive equations for solid-block and granular landslides. Considering the fact that accessible information on landslide characteristics is typically restricted, four major landslide parameters were considered: slope angle, slide volume, water depth, and landslide thickness to develop these equations. Although the inclusion of a few landslide parameters in the equations and the absence of landslide velocity may introduce some uncertainties in the equations, such uncertainties are expected to be negligible because, in reality, most landslides move under gravity and thus velocity is a predictable parameter.

The simulation data curve-fitting shows that for both types of landslides, V is directly correlated to a_M (Figure 4.11), but h is inversely related to a_M. (Figure 4.10). Based on earlier research and the findings of this study, the link between slope angle and a_M for solid-block landslides is inverse; however, this association is direct for granular material up to the crucial slope angle of θ=40°–60°. Two equations for forecasting a_M were established here by examining the non-dimensional forms of these four crucial landslide parameters.

The following equation gives a_M for solid-block landslides:

$$a_M/h = 0.4545\ (tan\,\alpha)^{0.062}\ (\frac{V}{h^3})^{0.296}\ (\frac{h}{s})^{-0.235} \tag{4.21}$$

The following equation gives a_M for granular landslides:

$$a_M/h = 0.2152\ (tan\,\alpha)^{0.244}\ (\frac{V}{h^3})^{0.603}\ (\frac{h}{s})^{-0.174} \tag{4.22}$$

where a_M represents the maximum positive initial wave amplitude in meters, α is the slope angle in degrees, V represents the slide volume in m^3, s represents the slide thickness in meters, and h represents the water depth in metres. It should be mentioned that based on this study on the impacts of friction coefficient (f = 0.3 – 0.55) on wave amplitudes (Figure 4.15) demonstrated that the amplitudes could alter by up to 10% and 14% for solid-block and granular materials, respectively. As a result, 10% and 14% uncertainty ranges could be considered for Equations (4.21) and (4.22), respectively, which are within an acceptable range based on engineering experiments.

Figure 4.17 depicts the performance of these two equations in predicting experimental data, which indicted satisfactory results since the data points are aligned around the 45-degree lines. To investigate the effectiveness of the predictive equations further, they were applied to three real-world subaerial landslide tsunami events: the 2018 Anak Krakatau (solid-block slide), the 1792 Unzen (granular slide), and the 1958 Lituya Bay (granular slide) (Table 2.3).

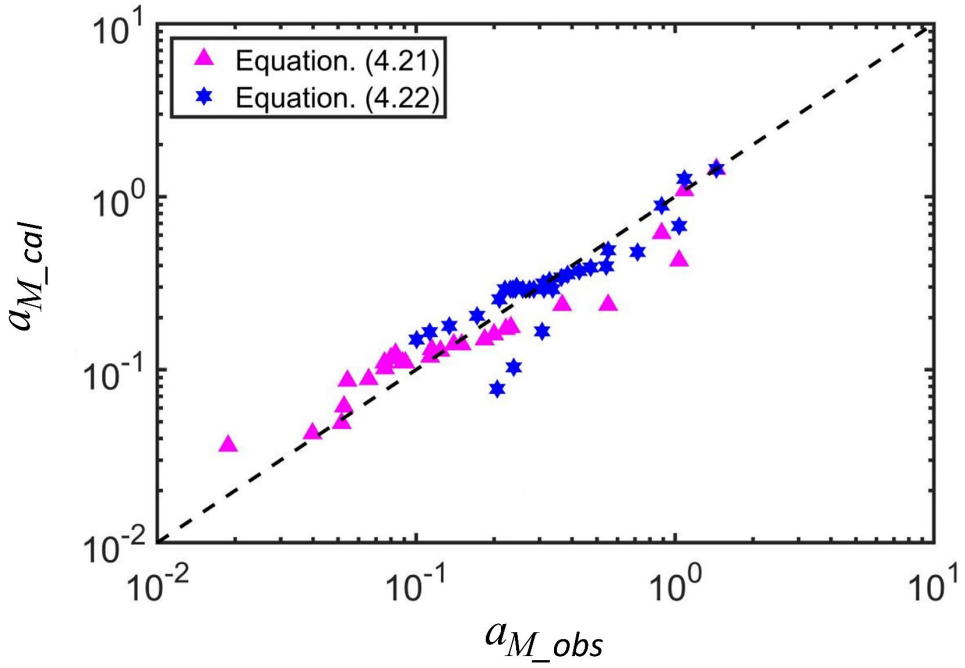

Figure 4.17. Accuracy of the derived predicative equations (a_{M_cal}, Eqs. 4.21 and 4.22) in reproducing experimental data (a_{M_obs}).

In following, the performance of the developed equations (Eqs. 4.21 and 4.22) with that of other previously published relationships for predicting maximum positive initial wave amplitudes of subaerial solid-block and granular landslides was evaluated (Table 4.4).

Table 4.4 Evaluating the performance of the newly developed equations (Eqs. 4.21 and 4.22) with the existing equations for reproducing of the initial maximum wave of real-world subaerial landslide tsunamis. Parameters are a_M, initial maximum wave amplitude; ρ_s, slide density; ρ_w, water density; v_s; slide width, l_s; slide velocity; V, slide volume; b_s, slide width; l_s, slide length; h, water depth; s, slide thickness; α, slope angle; m_s, slide mass; and, V_{im}^F, the volume of the final immersed landslide. For both types of landslides $V_{im}^F = V$ was considered.

Type	Predictive equations*	Author (year)	Observed a_M (m)	Calculated a_M (m)	Error, ε (%)***
Granular landslide (1958 Lituya Bay)	$a_M/h = 10^{[-1.25+0.71\log(0.5\frac{\rho_s}{\rho_w}\frac{V}{h^3}\frac{v_s^2}{gh})]}$	Slingerland and Voight (1982)	152	328	116
	$a_M/h = 0.25\left(\frac{v_s}{\sqrt{gh}}\right)^{1.4}\left(\frac{s}{h}\right)^{0.8}$	Fritz et al. (2004)	152	152	0
	$a_M/h = \frac{4}{9}\left[\frac{v_s}{\sqrt{gh}}\left(\frac{s}{h}\right)^{0.5}(m_s/\rho_w b_s h^2)^{0.25}(\cos\frac{6}{7}\alpha)^{0.5}\right]^{0.8}$	Heller and Hagger (2014)	152	216	42
	$a_M/h = 0.25\left(\frac{V_{im}^F}{b_s h^2}\right)^{0.8}$	Robbe-Saule et al. (2021)	152	129	15
	$a_M/h = 0.2152\ (tan\,\alpha)^{0.244}\ (\frac{V}{h^3})^{0.603}\ (\frac{h}{s})^{-0.174}$	This study	152	144	5

Granular landslide (1792 Unzen)	$a_M/h = 10^{[-1.25+0.71\log(0.5\frac{\rho_s}{\rho_w}\frac{V}{h^3}\frac{v_s^2}{gh})]}$	Slingerland and Voight (1982)	10	4.2	58
	$a_M/h = 0.25\left(\frac{v_s}{\sqrt{gh}}\right)^{1.4}\left(\frac{s}{h}\right)^{0.8}$	Fritz et al. (2004)	10	71	610
	$a_M/h = \frac{4}{9}\left[\frac{v_s}{\sqrt{gh}}\left(\frac{s}{h}\right)^{0.5}(m_s/\rho_w b_s h^2)^{0.25}(\cos\frac{6}{7}\alpha)^{0.5}\right]^{0.8}$	Heller and Hagger (2014)	10	175	1,650
	$a_M/h = 0.25\left(\frac{V_{im}^F}{b_s h^2}\right)^{0.8}$	Robbe-Saule et al. (2021)	10	15	50
	$a_M/h = 0.2152\ (tan\,\alpha)^{0.244}\ (\frac{V}{h^3})^{0.603}\ (\frac{h}{s})^{-0.174}$	This study	10	22	120
Solid-block landslide (2018 Anak Krakatau)	$a_M/h = 1.32\ \frac{v_s}{\sqrt{gh}}$	Noda (1970)	134	134	0
	$a_M/h = 0.667\left(0.5\,(\frac{v_s}{\sqrt{gh}})^2\right)^{0.334}\left(\frac{b_s}{s}\right)^{0.754}\left(\frac{l_s}{s}\right)^{0.506}\left(\frac{s}{h}\right)^{1.631}$	Bolin et al. (2014) **	134	5,762	4,200
	$a_M/h = 0.25\left(\frac{V_{im}^F}{b_s h^2}\right)^{0.8}$	Robbe-Saule et al. (2021)	134	31	77
	$a_M/h = 0.4545\ (tan\,\alpha)^{0.062}\ (\frac{V}{h^3})^{0.296}\ (\frac{h}{s})^{-0.235}$	This study	134	126	6

*: Parameters are a_M, initial maximum wave amplitude; h, water depth; ρ_s, slide density; ρ_w, water density; v_s, slide velocity; V, slide volume; b_s, slide width; l_s, slide length; s, slide thickness; α, slope angle; $m_s(=\rho_s V)$, slide mass; and, V_{im}^F, the volume of the final immersed landslide. We considered $V_{im}^F = V$ for both types of landslides.

Landslide parameters of the 1958 Lituya Bay tsunami are based on Fritz et al. (2004): v_s=110 m/s; ρ_s= 2700 kg/m^3; ρ_w=1000 kg/m^3; and b_s=338 m.

The equations in Table 4 were produced predictions in the range of 129 – 328 m (error ranges of 0–116%) for the granular slide of the 1958 Lituya Bay event with a reported amplitude of 152 m. The best results were obtained by applying the equations of Fritz et al. (2004), this study (Eq. 4.22), and Robbe-Saule et al (2021). The forecasts for the 2018 Anak Krakatau solid-block event (observed amplitude of 134 m) were in the range of 31 – 5,762 m, giving an error domain of 0 – 4,200%. (Table 4.4). This study's equation (Eq. 4.21) and Noda's relationship produced the greatest results (1970). For the 1792 Unzen incident, with a recorded wave amplitude of 10 m, the developed equations in this study (Eq. 4.22) predicted an amplitude of 22 m, whereas other equations estimate a range of 4.2 – 175 m. (Table 4.4).

In comparison with the other predictive equations in the literature, two predictive relationships of this study (Eqs. 4.21 and 4.22) perform well in replicating actual subaerial landslide events, despite the fact that both require only four landslide factors (i.e., volume, water depth, slope angle, and landslide thickness). It should be mentioned that the Fritz et al. (2004) equation has less parameters than developed equations in this study and predicts the 1958 Lituya Bay event better, but it underperforms in the case of the 1792 Unzen event (Table 4.4). The fact that presented prediction equations in this study require fewer parameters for application is an advantage that would improve preliminary tsunami hazard assessment for sensitive regions.

4.4: Results of physical experiment of subaerial landslide (wave period)

The FFT procedure was used to calculate the dominant wave periods for each experimental waveform, and the results were shown in Figure 4.18 and Table 3.8. The dominant wave period for the 51 experiments ranges from 0.51 s to 1.51 s. (Table 3.8). The experiment with Solid-block-1 (the smallest one) at 0.25 m water depth and free gravity movement had the shortest dominant wave period of 0.51 s. The longest period of 1.51 seconds was obtained by using Solid-block-4 (the largest one) at a water depth of 0.25 m and controlled movement. Properties of solid-blocks are reported in Table 3.2. According to the data in Table 3.8, the maximum dominant wave period was Three times longer than the minimum period, indicating that the experimental data were sufficiently separated from one another.

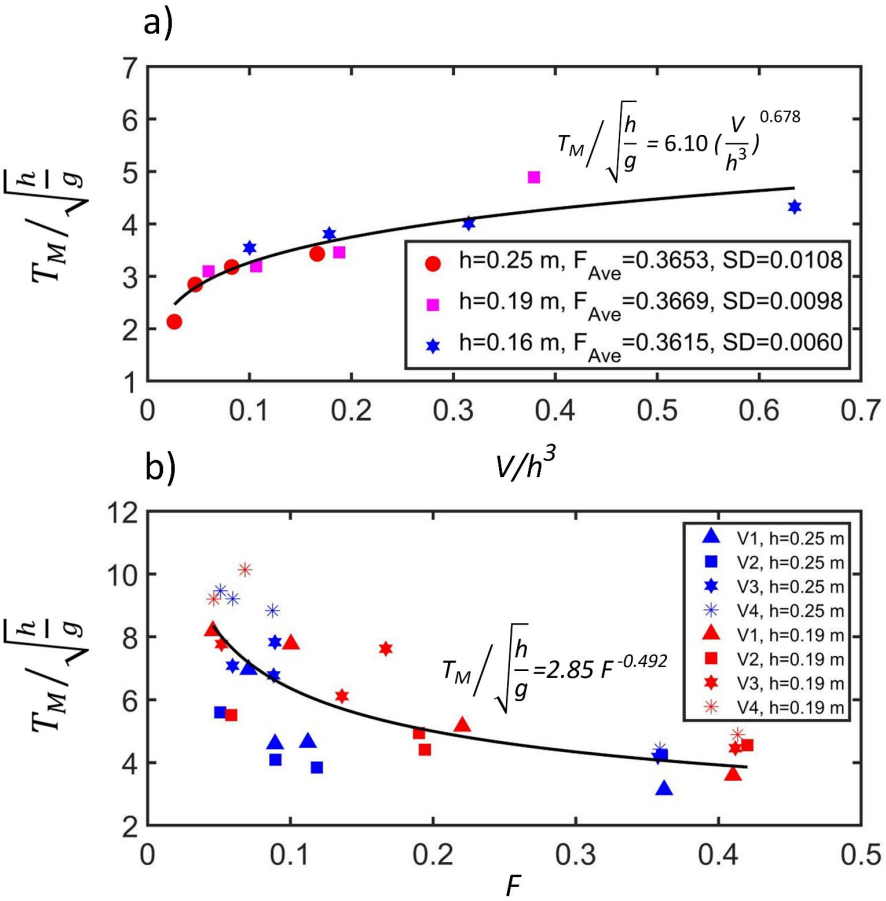

Figure 4.18. Curve fitting to the experimental data of the dominant wave period (T_M). (a) The effect of sliding mass volume (V) on wave period. F_{Ave} is the average Froude number for each test group. Tests with the same release mechanism (i.e., gravity; F≅0.36) and water depth but different slide volumes were grouped together for this analysis. (b) The effect of the landslide Fronde number (F) on the wave period. Here, h is the depth of the water, and g is the gravitational acceleration. For this analysis, tests with the same water depths and volumes but a different Froude number were combined. The abbreviation SD stands for standard deviation.

Two plots were created from the experimental data to study the relationship between wave period and the two landslide parameters of volume (V) and Froude number (F). The data revealed a direct relationship between dominant wave period and landslide volume, as shown in the following equation:

$$T_M = 6.10\, V^{0.678} \tag{4.23}$$

where T_M denotes the dominant wave period in seconds, and V denotes the landslide volume in m^3. Heller and Spinneken previously reported a direct relationship between T_M and V. (2013). According to Equation (4.23), the larger the volume of a landslide, the longer the period of the generated wave.

In terms of the landslide's Froude number (F), this study's experiments revealed an inverse relationship between F and wave period as follows:

$$T_M = 2.85\, F^{-0.529} \tag{4.24}$$

where T_M is the dominant wave period in seconds and F is the landslide's Froude number calculated using Equation (3.5). Heller and Spinneken (2013) found a direct relationship between T_M and F, whereas this study found an inverse relationship. According to the physics of water waves, slower landslides with lower Froude numbers appear to generate waves with longer periods. Van Nieuwkoop's experimental studies have confirmed this (2007).

In this study, data from different scales (laboratory and field scales) were used to generate the predictive equation for the wave period of subaerial solid-block landslide-generated waves as an innovation. Calibration and validation of empirical equations using field data was required to ensure that the equations can be successfully applied to real-world events. The lack of field data has been a challenge for this type of research. However, there have been some subaerial tsunamis in recent years, such as the Anak Krakatau tsunami in December 2018, which provided actual field data. For the 2018 Anak Krakatau event, several authors contributed field data and numerical simulations (Grilli et al. 2019, 2021; Heidarzadeh et al. 2020; Mulia et al. 2020; Paris et al. 2020). Heidarzadeh et al. (2020) calculated the wave period of this tsunami to be in the range of $6.3 - 8.9$ min; in this study, the average of this range is considered (period of 7.6 min = 456 s) for the wave period of the 2018 Anak Krakatau tsunami.

In this study, the experimental data (Table 3.8) were combined with field data from the 2018 Anak Krakatau event to produce the presented predictive equation. The two parameters, slide volume (V/h^3) and landslide Froude number (F), were used in their nondimensional forms. Based on the previous section's results, the same powers were used for these nondimensional parameters in the predictive equation. The final equation for the nondimensional wave period ($T_M/\sqrt{\frac{h}{g}}$) is given as follows:

$$\frac{T_M}{\sqrt{h/g}} = 6.772\,(\frac{V}{h^3})^{0.678}/F^{\,0.529} \quad (4.25)$$

where T_M is the dominant wave period caused by subaerial solid-block landslides in seconds, g is gravitational acceleration (=9.81 m/s^2), F is the Froude number (nondimensional), s is the slide thickness in metres, V is the slide volume in m^3, and h is the water depth in metres. Equation (4.25), for a slope angle of 30^o, is developed. Table 4.5 compares this predictive equation to three other equations proposed by Ataie-Ashtiani and Nik-Khah (2008), Heller and Spinneken (2013), and Heller and Spinneken (2015). For the 2018 Anak Krakatau event, the equations proposed by these authors yield wave periods ranging from 390 s to 24,600 s, 40 s to 52 s, and 34 s to 35 s, respectively (Table 4.5). However, because the data from the 2018 Anak Krakatau tsunami was included in the database that was used to develop the presented predictive equation, it is natural that this equation predicts the wave period of this tsunami in the range of 313 s − 670 s.

Table 4.5. The performance of the developed equation (Equation. 4.25) for predicting the dominant period of the 2018 Anak Krakatau subaerial landslide tsunami is shown in Table 4.5. T_M, is the dominant wave period; V is the landslide volume; h is the water depth; and F is the Froude number. The 2018 Anak Krakatau event parameters are based on the average values reported by Heidarzadeh et al. (2020), Grilli et al (2019, 2021).

Author(s)	Predictive equation*	V (m^3)	h (m)	s (m)	F	Observed T_M (s)*	Predicted T_M (s)
This study	$\frac{T_M}{\sqrt{h/g}} = 6.772\,(\frac{V}{h^3})^{0.678}/F^{\,0.492}$	250×10^6	100–200	100–250	1.0–1.40	378–534	313-765

*: Based on Heidarzadeh et al. (2020).

Figure 4.19 depict the performance of this study predictive equation (Eq. 4) in estimating the experimental data from this study (Table 3) in conjunction with the 2018 Anak Krakatau event. As the data points were aligned around the 45^o line, the results showed acceptable performance.

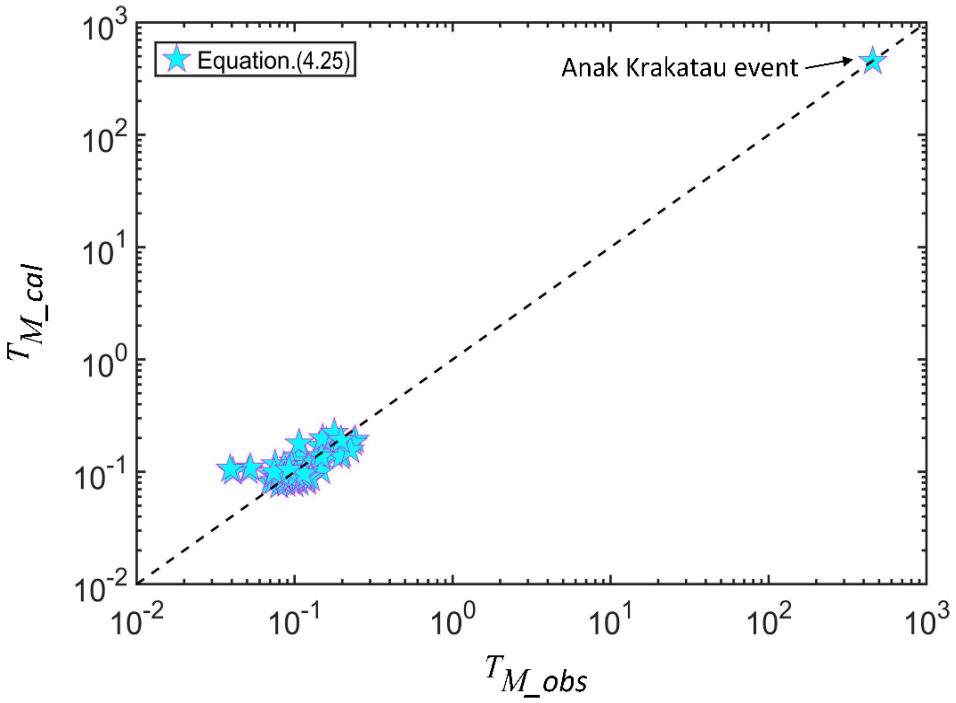

Figure 4.19 Evaluation of the developed predicative equation (T_{M_cal}, Eq. 4.25) in regenerating experimental data (T_{M_obs}).

To test how well the presented predictive equation works, it was applied to one field landslide tsunami event (the Åkerneset landslide in Norway, Harbitz et al., 2014) whose data was not in the database used to create the equation (Table 4.6). The wave period of this event was well predicted by the proposed equation.

Table 4.6. The proposed prediction equation was used to forecast the subaerial landslide tsunami at Åkerneset, Norway based on the Harbitz et al. (2014) modeling; This landslide tsunami event described here is highly hypothetical. Parameters are: T_M, dominant tsunami period; V, landslide volume; h, water depth; v_s, landslide velocity; and F, Froude number.

Event name	Predictive equation	V (m^3)	h (m)	v_s (m/s)	F	Observed T_M (s)**	Predicted T_M (s)
Åkerneset	4.25	54×10^6	250 – 300	70 – 80	1.3 – 1.6	~ 60	49 – 66

**: Based on Harbitz et al. (2014).

Chapter 5: Conclusion

Chapter 5: Conclusion

5.1: Summary

Landslide-generated tsunamis were physically and numerically modelled in this study. A number of predictive equations for estimating the initial wave amplitude and period of landslides (subaerial and submarine) were developed.

- The performance of existing equations was evaluated through an analytical study.
- In order to find the data gap in experimental data, the literature was heavily searched, and relevant studies were detected.
- Three series of experiments, including 75 tests for submarine and subaerial landslides with different types of slides (solid-block and granular material), were conducted considering two aims: i) fill the data gap of literature, and ii) sensitivity analyse of landslide parameters.
- The sensitivity analyses through the physical experiments were done to determine the effect of each landslide parameter on maximum initial wave amplitude and wave period.
- The FLOW3D-Hydro was validated using physical experiments to simulate the landslide-generated waves. The validated model was used to produce further data points and have a comprehensive sensitivity analysis of each landslide parameter. Also, a series of simulations were done to compare the effect of landslide type (solid-block and granular material) on generated wave characteristics. In total, 250 simulations were presented in this study.
- The validated FLOW3D-Hydro model can be used by engineers and scientists working on tackling landslide tsunami hazards, given the fact that experimental works are generally costly and time-consuming.
- The equations were nondimensionalized to be applicable to real-world case studies.
- The performance of predictive equations in this study was evaluated using the actual case studies.

Findings

- It was observed an inverse relationship between maximum initial landslide amplitude of submarine landslide-generated waves and submergence depth. While there were direct relationships between slide volume and slope angle with maximum initial landslide amplitude.
- In the experiments of submarine landslides with varying travel distance, an inverse relationship between travel distance and maximum initial landslide amplitude was seen: the shorter the travel distance, the larger the wave amplitude.

- Among all involved parameters in the existing predictive equations, slide volume (V) appears in most equations, thus emphasising its importance in estimating the maximum initial wave amplitude generated by submarine landslides.
- The predictions of wave amplitude through existing equations are divided by a few orders of magnitude. In particular, the values range from 0.03 to 686.5 m for the prediction of the maximum initial amplitude of the 1994 Skagway and from 3.7 to 6746.0 m for the 1998 Papua New Guinea (PNG) tsunamis. The observed amplitudes for the two aforesaid events are in the ranges of 1.0-2.1 m and 11-16 m, respectively.
- By applying the existing predictive equations to the two cases of 1994 Skagway and 1998 PNG landslide tsunamis, we witnessed a better agreement between the observed and predicted maximum initial wave amplitudes for the small-scale landslide tsunami (1994 Skagway). For the large-scale tsunami (1998 PNG), the predictions are scattered in a wider range. This may emphasis the essentiality of conducting large-scale or field-scale laboratory experiments on landslide-induced tsunamis.
- By changing d in the range of 0.04 – 0.193 m, we observed an inverse relationship between maximum initial landslide amplitude and submergence depth and that the maximum negative initial amplitude varies more significantly than the maximum positive amplitude of the submarine landslide-generated waves.
- It was observed that the dominant wave period of submarine landslide generated by the largest slide was 0.7 s whereas it was 1.1 s for the smallest slide. The latter unexpected observation could be attributed to the relatively lower velocity of the sliding mass for the case of the smaller block.
- The experimental study on subaerial landslide generated waves revealed that a direct relationship exists between the maximum initial wave period and landslide volume. Whereas an inverse relationship was seen between Froude number and wave period.
- The maximum initial wave amplitudes for subaerial solid-block slides were 107% larger than those for granular slides, for the same slide volumes and approximately similar weights.
- An inverse relationship was observed between slope angle and the maximum initial wave amplitudes of subaerial solid-block slides where the maximum amplitudes linearly decrease as the slope angle increases. However, for granular slides, a direct relationship was detected up to a critical slope angle of 60^{o} from where maximum amplitudes start to decrease for slope angles more than 60^{o}.
- Experiments revealed that wave periods remain nearly unchanged as water depth and slide volume vary for both subaerial solid-block and granular slides. However, it was observed that the wave period increases as the slope angle decreases for solid-block slides. Such a change was not seen for granular slides.

Limitations of this study

- This study was done in a 2D environment for both physical modelling and numerical simulations. Although many considerations were applied in this study to adopt the real-world landslide waves to a 2D environment, a 3D setup could reproduce these waves with much less considerations, also a 3D setup is ideal for wave energy dissipation investigations.
- Only one numerical model (FLOW-3D Hydro) was applied to simulate the landslide generated waves. Ideally another numerical model (e.g. OpenFOAM) could be used to compare the results and performance of numerical models.
- The dimension of the flume (wave tank) was relatively small (only 6 m length) in comparison with other studies (e.g. flume with 24 m length employed by Bruggemann, 2012). This limitation led to focusing only on near-field investigation of landslide generated waves.

5.2: Contribution to Tsunami Research

In order to cope with the lack of availability of real-world landslide parameters, the main approach for developing the predictive equation was to minimize the number of input landslide parameters. The proposed equations in this study using three or four parameters are able to estimate the maximum wave amplitude and wave period of landslide waves with high accuracy.

The presented experimental data, including the data point and waveforms, provides high-precision benchmark scenarios to advance and validate numerical models of landslide-generated tsunamis. The validated numerical model (FLOW-3D-Hydro) could be used by engineers and scientists working on landslide tsunami hazards. The comparison between generated waves by solid-block and granular subaerial landslide through the physical experiment and numerical simulations was delivered in this study for the very first time.

5.3 Future directions

- In this study, for analysing the effect of each landslide parameter on wave amplitude or wave period while only one parameter was changed the other parameters were kept constant. Future studies could analyse the effect of changing multiple parameters on the characteristics of landslide-generated waves. Both Genetic Algorithms as a stochastic optimization technique, and Deep-Neural Network machine learning could be used to derive these predictive equations.

- The existing predictive equation for estimating the wave period of landslide-generated waves is very limited; more studies on this topic could improve the performance of predictive equations and, consequently, the accuracy of numerical models. Further field surveys in order to find more actual data are essential for improving the estimation of predictive equations. The physical experiments and numerical simulations of submarine landslides in this research are limited to solid-block landslides. However, the granular submarine landslides may generate tsunami waves, which could be investigated in future studies.

- The other numerical models (e.g. OpenFOAM; Ansys Fluent; MIKE-21) could be used to provide a benchmark for evaluating the performance of this study numerical model (FLOW-3D Hydro).

- Although dual-source tsunamis are known to be particularly hazardous, they are not well studied and the majority of existing studies investigate the tsunami's waves generated by landslide or earthquake independently; as modelling landslide-generated tsunamis is challenging. However, it is being recognised that landslide and dual-source tsunamis are more common than previously thought. The lack of hazard assessment from dual-source tsunamis, coupled with the increasing risk to coastal populations and infrastructure, means we lack data and information on what the future risk might be. Since there are two or more waves interacting, wave interference is a key concept. Depending on how the crests and troughs of the water waves are matched up, the waves will possibly add together, or they can partially or even completely cancel each other. As a result of positive interference, the amplitude of the combined wave could be much larger and more destructive than the amplitude of an individual wave. This makes dual-source tsunamis particularly dangerous and difficult to predict. The proposed work as the further study will lead to new insights into the hydrodynamics of dual-source tsunamis. Given we have already "baked in" future sea-level rises due to global warming, knowing the future risk to the 1.5 billion people living in the low-elevation coastal zones is vital to creating tangible coastal defences (Rossetto et al, 2014; Merkens et al., 2016).

Reference

Aida, I., 1978. Reliability of a tsunami source model derived from fault parameters. *Journal of Physics of the Earth*, *26*(1), pp.57-73.

Abadie, S., Morichon, D., Grilli, S. and Glockner, S., 2010. Numerical simulation of waves generated by landslides using a multiple-fluid Navier–Stokes model. *Coastal engineering*, *57*(9), pp.779-794.

Ataie-Ashtiani, B. and Najafi-Jilani, A., 2008. Laboratory investigations on impulsive waves caused by underwater landslide. *Coastal Engineering*, *55*(12), pp.989-1004.

Ataie-Ashtiani, B. and Nik-Khah, A., 2008. Impulsive waves caused by subaerial landslides. *Environmental Fluid Mechanics*, *8*, pp.263-280.

Ataie-Ashtiani, B. and Najafi Jilani, A., 2007. A higher-order Boussinesq-type model with moving bottom boundary: applications to submarine landslide tsunami waves. *International journal for numerical methods in fluids*, *53*(6), pp.1019-1048.

Ataie-Ashtiani, B. and Yavari-Ramshe, S., 2011. Numerical simulation of wave generated by landslide incidents in dam reservoirs. *Landslides*, *8*, pp.417-432.

Aránguiz, R., Esteban, M., Takagi, H., Mikami, T., Takabatake, T., Gómez, M., González, J., Shibayama, T., Okuwaki, R., Yagi, Y. and Shimizu, K., 2020. The 2018 Sulawesi tsunami in Palu city as a result of several landslides and coseismic tsunamis. *Coastal Engineering Journal*, *62*(4), pp.445-459.

Bolin, H., Yueping, Y., Xiaoting, C., Guangning, L., Sichang, W. and Zhibing, J., 2014. Experimental modeling of tsunamis generated by subaerial landslides: two case studies of the Three Gorges Reservoir, China. *Environmental Earth Sciences*, *71*, pp.3813-3825.

Bruggemann, M., 2012, June. Composite modelling of the influence of geometry on landslide generated impulse waves. In *Proceedings of the 1st Civil and Environmental Engineering Student Conference*.

Bullard, G.K., Mulligan, R.P., Carreira, A. and Take, W.A., 2019. Experimental analysis of tsunamis generated by the impact of landslides with high mobility. *Coastal Engineering*, *152*, p.103538.

Chipperfield, A.J., Fleming, P.J., Pohlheim, H. and Fonseca, C.M., 1994, September. A genetic algorithm toolbox for MATLAB. In *Proc. International Conference on Systems Engineering, Coventry, UK* (Vol. 6, No. 8).

Choi, B.H., Kim, D.C., Pelinovsky, E. and Woo, S.B., 2007. Three-dimensional simulation of tsunami run-up around conical island. *Coastal Engineering*, *54*(8), pp.618-629.

Dan, G., Sultan, N. and Savoye, B., 2007. The 1979 Nice harbour catastrophe revisited: trigger mechanism inferred from geotechnical measurements and numerical modelling. *Marine Geology*, *245*(1-4), pp.40-64.

Dean, R.G. and Dalrymple, R.A., 1991. *Water wave mechanics for engineers and scientists* (Vol. 2). world scientific publishing company.

Du Pont, S.C., Gondret, P., Perrin, B. and Rabaud, M., 2003. Wall effects on granular heap stability. *Europhysics letters*, *61*(4), p.492.

Enet, F. and Grilli, S.T., 2007. Experimental study of tsunami generation by three-dimensional rigid underwater landslides. *Journal of waterway, port, coastal, and ocean engineering*, *133*(6), pp.442-454.

Evers, F.M., Hager, W.H. and Boes, R.M., 2019. Spatial impulse wave generation and propagation. *Journal of Waterway, Port, Coastal, and Ocean Engineering*, *145*(3), p.04019011.

Frederik, M.C., Adhitama, R., Hananto, N.D., Sahabuddin, S., Irfan, M., Moefti, O., Putra, D.B. and Riyalda, B.F., 2019. First results of a bathymetric survey of Palu Bay, Central Sulawesi, Indonesia following the Tsunamigenic Earthquake of 28 September 2018. *Pure and Applied Geophysics*, *176*, pp.3277-3290.

Fritz, H.M., Hager, W.H. and Minor, H.E., 2004. Near field characteristics of landslide generated impulse waves. *Journal of waterway, port, coastal, and ocean engineering*, *130*(6), pp.287-302.

Fernández-Nieto, E.D., Bouchut, F., Bresch, D., Diaz, M.C. and Mangeney, A., 2008. A new Savage–Hutter type model for submarine avalanches and generated tsunami. *Journal of Computational Physics*, *227*(16), pp.7720-7754.

Flow Science., 2022. FLOW3D-Hydro version 12.0 user's manual Computer software. *Santa Fe, NM, USA*. https://www.flow3d.com/ (Accessed on 10th Dec 2022).

Fritz, H.M., 2002. *Initial phase of landslide generated impulse waves* (Doctoral dissertation, ETH Zurich).

Fritz, H.M., Synolakis, C.E., Kalligeris, N., Skanavis, V., Santoso, F.J., Rizal, M., Prasetya, G., Liu, Y. and Liu, P.L., 2019, January. The 2018 Sulawesi tsunami: Field survey and eyewitness video analysis using LiDAR. In *Geophysical Research Abstracts* (Vol. 21).

Fritz, H.M., Mohammed, F. and Yoo, J., 2009. Lituya Bay landslide impact generated mega-tsunami 50 th Anniversary. *Tsunami Science Four Years after the 2004 Indian Ocean Tsunami: Part II: Observation and Data Analysis*, pp.153-175.

Fine, I.V., Rabinovich, A.B., Bornhold, B.D., Thomson, R.E. and Kulikov, E.A., 2005. The Grand Banks landslide-generated tsunami of November 18, 1929: preliminary analysis and numerical modeling. *Marine Geology*, *215*(1-2), pp.45-57.

Fuhrman, D.R. and Madsen, P.A., 2009. Tsunami generation, propagation, and run-up with a high-order Boussinesq model. *Coastal Engineering*, *56*(7), pp.747-758.

Fujii, N., Matsuyama, M. and Mori, H., 2018. Hydraulic experiments of tsunami generation with plane water tank due to landslide. *Doboku Gakkai Ronbunshu B2. Kaigan Kogaku (Online)*, *74*(2), pp.1-145.

Gómez, J., Berezowsky, M., Lara, A. and González, E., 2016. Prediction of the water waves generated by a potential semisubmerged landslide in La Yesca reservoir, Mexico. *Landslides*, *13*, pp.1509-1518.

Grilli, S.T. and Watts, P., 2005. Tsunami generation by submarine mass failure. I: Modeling, experimental validation, and sensitivity analyses. *Journal of waterway, port, coastal, and ocean engineering*, *131*(6), pp.283-297.

Grilli, S.T., Tappin, D.R., Carey, S., Watt, S.F., Ward, S.N., Grilli, A.R., Engwell, S.L., Zhang, C., Kirby, J.T., Schambach, L. and Muin, M., 2019. Modelling of the tsunami from the December 22, 2018 lateral collapse of Anak Krakatau volcano in the Sunda Straits, Indonesia. *Scientific reports*, *9*(1), p.11946.

Gusman, A.R., Supendi, P., Nugraha, A.D., Power, W., Latief, H., Sunendar, H., Widiyantoro, S., Wiyono, S.H., Hakim, A., Muhari, A. and Wang, X., 2019. Source model for the tsunami inside Palu Bay following the 2018 Palu earthquake, Indonesia. *Geophysical Research Letters*, *46*(15), pp.8721-8730.

Grilli, S.T., Shelby, M., Kimmoun, O., Dupont, G., Nicolsky, D., Ma, G., Kirby, J.T. and Shi, F., 2017. Modeling coastal tsunami hazard from submarine mass failures: effect of slide rheology, experimental validation, and case studies off the US East Coast. *Natural hazards*, *86*, pp.353-391.

Grilli, S.T., Vogelmann, S. and Watts, P., 2002. Development of a 3D numerical wave tank for modeling tsunami generation by underwater landslides. *Engineering analysis with boundary elements*, *26*(4), pp.301-313.

Grilli, S.T., Zhang, C., Kirby, J.T., Grilli, A.R., Tappin, D.R., Watt, S.F.L., Hunt, J.E., Novellino, A., Engwell, S., Nurshal, M.E.M. and Abdurrachman, M., 2021. Modeling of the Dec. 22nd 2018 Anak Krakatau volcano lateral collapse and tsunami based on recent field surveys: Comparison with observed tsunami impact. *Marine Geology*, *440*, p.106566.

Grilli, S.T., Tappin, D.R., Carey, S., Watt, S.F., Ward, S.N., Grilli, A.R., Engwell, S.L., Zhang, C., Kirby, J.T., Schambach, L. and Muin, M., 2019. Modelling of the tsunami from the December 22, 2018 lateral collapse of Anak Krakatau volcano in the Sunda Straits, Indonesia. *Scientific reports*, *9*(1), p.11946.

Harbitz, C.B. and Pedersen, G., 1992. Model theory and analytical solutions for large water waves due to landslides. *Preprint series. Mechanics and Applied Mathematics http://urn. nb. no/URN: NBN: no-23418*.

Harbitz, C.B., 1992. Model simulations of tsunamis generated by the Storegga slides. *Marine geology*, *105*(1-4), pp.1-21.

Harbitz, C.B., Løvholt, F. and Bungum, H., 2014. Submarine landslide tsunamis: how extreme and how likely? *Natural Hazards*, *72*, pp.1341-1374.

Harlow, F.H. and Welch, J.E., 1965. Numerical calculation of time-dependent viscous incompressible flow of fluid with free surface. *The physics of fluids*, *8*(12), pp.2182-2189.

Heidarzadeh, M., Ishibe, T., Sandanbata, O., Muhari, A. and Wijanarto, A.B., 2020. Numerical modeling of the subaerial landslide source of the 22 December 2018 Anak Krakatoa volcanic tsunami, Indonesia. *Ocean Engineering*, *195*, p.106733.

Heidarzadeh, M. and Satake, K., 2015. Source properties of the 1998 July 17 Papua New Guinea tsunami based on tide gauge records. *Geophysical Journal International*, *202*(1), pp.361-369.

Heidarzadeh, M. and Satake, K., 2017. A combined earthquake–landslide source model for the Tsunami from the 27 November 1945 M w 8.1 Makran earthquake. *Bulletin of the Seismological Society of America*, *107*(2), pp.1033-1040.

Heidarzadeh, M. and Satake, K., 2014. Possible sources of the tsunami observed in the northwestern Indian Ocean following the 2013 September 24 M w 7.7 Pakistan inland earthquake. *Geophysical Journal International*, *199*(2), pp.752-766.

Heidarzadeh, M., Ishibe, T., Sandanbata, O., Muhari, A. and Wijanarto, A.B., 2020. Numerical modeling of the subaerial landslide source of the 22 December 2018 Anak Krakatoa volcanic tsunami, Indonesia. *Ocean Engineering*, *195*, p.106733.

Heinrich, P., 1992. Nonlinear water waves generated by submarine and aerial landslides. *Journal of Waterway, Port, Coastal, and Ocean Engineering*, *118*(3), pp.249-266.

Heller, V., 2007. *Landslide generated impulse waves: Prediction of near field characteristics* (Doctoral dissertation, Eth Zurich).

Heller, V. and Spinneken, J., 2015. On the effect of the water body geometry on landslide–tsunamis: Physical insight from laboratory tests and 2D to 3D wave parameter transformation. *Coastal Engineering*, *104*, pp.113-134.

Heller, V. and Hager, W.H., 2011. Wave types of landslide generated impulse waves. *Ocean Engineering*, *38*(4), pp.630-640.

Heller, V. and Spinneken, J., 2015. On the effect of the water body geometry on landslide–tsunamis: Physical insight from laboratory tests and 2D to 3D wave parameter transformation. *Coastal Engineering*, *104*, pp.113-134.

Heller, V., Hager, W.H. and Minor, H.E., 2008. Scale effects in subaerial landslide generated impulse waves. *Experiments in Fluids*, *44*, pp.691-703.

Heller, V. and Hager, W.H., 2014. A universal parameter to predict subaerial landslide tsunamis? *Journal of Marine Science and Engineering*, *2*(2), pp.400-412.

Heller, V. and Spinneken, J., 2013. Improved landslide-tsunami prediction: effects of block model parameters and slide model. *Journal of Geophysical Research: Oceans*, *118*(3), pp.1489-1507.

Heller, V. and Hager, W.H., 2011. Wave types of landslide generated impulse waves. *Ocean Engineering*, *38*(4), pp.630-640.

Heller, V., 2011. Scale effects in physical hydraulic engineering models. *Journal of Hydraulic Research*, *49*(3), pp.293-306.

Heinrich, P., 1992. Nonlinear water waves generated by submarine and aerial landslides. *Journal of Waterway, Port, Coastal, and Ocean Engineering*, *118*(3), pp.249-266.

Horrillo, J., Wood, A., Kim, G.B. and Parambath, A., 2013. A simplified 3-D Navier-Stokes numerical model for landslide-tsunami: Application to the Gulf of Mexico. *Journal of Geophysical Research: Oceans*, *118*(12), pp.6934-6950.

Hirt, C.W. and Nichols, B.D., 1981. Volume of fluid (VOF) method for the dynamics of free boundaries. *Journal of computational physics*, *39*(1), pp.201-225.

Hughes, S.A., 1993. *Physical models and laboratory techniques in coastal engineering* (Vol. 7).

Ioualalen, M., Migeon, S. and Sardoux, O., 2010. Landslide tsunami vulnerability in the Ligurian Sea: case study of the 1979 October 16 Nice international airport submarine landslide and of identified geological mass failures. *Geophysical Journal International*, *181*(2), pp.724-740.

Imamura, F. and Imteaz, M.A., 1995. Long waves in two-layers: governing equations and numerical model. *Science of Tsunami Hazards*, *13*(1), pp.3-24.

Iwasaki, S.I., 1982. 12. Experimental Study of a Tsunami Generated by a Horizontal Motion of a Sloping Bottom.

Jin, Y.C., Guo, K., Tai, Y.C. and Lu, C.H., 2016. Laboratory and numerical study of the flow field of subaqueous block sliding on a slope. *Ocean Engineering*, *124*, pp.371-383.

Kamphuis, J.W. and Bowering, R.J., 1970. Impulse waves generated by landslides. In *Coastal Engineering 1970* (pp. 575-588).

Kim, G.B., Cheng, W., Sunny, R.C., Horrillo, J.J., McFall, B.C., Mohammed, F., Fritz, H.M., Beget, J. and Kowalik, Z., 2020. Three-dimensional landslide generated tsunamis: Numerical and physical model comparisons. *Landslides*, *17*, pp.1145-1161.

Kirby, J.T., Shi, F., Nicolsky, D., Ma, G., Misra, S. and Rao, P., 2017. The 1975 Kitimat Landslide Tsunami: validation and comparative testing of modeling strategies. In *Coastal Structures and Solutions to Coastal Disasters 2015: Tsunamis* (pp. 13-23). Reston, VA: American Society of Civil Engineers.

Kim, G., 2012. *Numerical simulation of three-dimensional tsunami generation by subaerial landslides* (Doctoral dissertation).

Liu, P.F., Wu, T.R., Raichlen, F., Synolakis, C.E. and Borrero, J.C., 2005. Runup and rundown generated by three-dimensional sliding masses. *Journal of fluid Mechanics*, *536*, pp.107-144.

Løvholt, F., Glimsdal, S. and Harbitz, C.B., 2020. On the landslide tsunami uncertainty and hazard. Landslides, 17(10), pp.2301-2315.

Løvholt, F., Pedersen, G. and Kim, J., 2017. Modeling of Benchmark 2; The Oslo group.

Liu, P.F., Wu, T.R., Raichlen, F., Synolakis, C.E. and Borrero, J.C., 2005. Runup and rundown generated by three-dimensional sliding masses. *Journal of fluid Mechanics*, *536*, pp.107-144.

Lo, H.Y. and Liu, P.L.F., 2017. On the analytical solutions for water waves generated by a prescribed landslide. *Journal of Fluid Mechanics*, *821*, pp.85-116.

Løvholt, F., Harbitz, C.B. and Haugen, K.B., 2005. A parametric study of tsunamis generated by submarine slides in the Ormen Lange/Storegga area off western Norway. In *Ormen lange–an*

integrated study for safe field development in the storegga submarine area (pp. 219-231). Elsevier.

Løvholt, F., Pedersen, G., Harbitz, C.B., Glimsdal, S. and Kim, J., 2015. On the characteristics of landslide tsunamis. *Philosophical Transactions of the Royal Society A: Mathematical, Physical and Engineering Sciences*, *373*(2053), p.20140376.

Lynett, P.J., Borrero, J.C., Liu, P.L.F. and Synolakis, C.E., 2003. Field survey and numerical simulations: A review of the 1998 Papua New Guinea tsunami. *Landslide tsunamis: Recent findings and research directions*, pp.2119-2146.

Lynett, P. and Liu, P.L.F., 2002. A numerical study of submarine–landslide–generated waves and run–up. *Proceedings of the Royal Society of London. Series A: Mathematical, Physical and Engineering Sciences*, *458*(2028), pp.2885-2910.

Lynett, P. and Liu, P.L.F., 2005. A numerical study of the run-up generated by three-dimensional landslides. *Journal of Geophysical Research: Oceans*, *110*(C3).

Lee, C.H. and Huang, Z., 2022. Effects of grain size on subaerial granular landslides and resulting impulse waves: experiment and multi-phase flow simulation. *Landslides*, *19*(1), pp.137-153.

Lindstrøm, E.K., 2016. Waves generated by subaerial slides with various porosities. *Coastal Engineering*, *116*, pp.170-179.

Liu, P.L.F., Lynett, P. and Synolakis, C.E., 2003. Analytical solutions for forced long waves on a sloping beach. *Journal of Fluid Mechanics*, *478*, pp.101-109.

Ma, G., Shi, F. and Kirby, J.T., 2012. Shock-capturing non-hydrostatic model for fully dispersive surface wave processes. *Ocean Modelling*, *43*, pp.22-35.

Ma, G., Kirby, J.T., Hsu, T.J. and Shi, F., 2015. A two-layer granular landslide model for tsunami wave generation: Theory and computation. *Ocean Modelling*, *93*, pp.40-55.

Mathworks., 2020. MATLAB user manual, The Math Works Inc., *MA, USA*.

McFall, B.C., 2014. *Physical modeling of landslide generated tsunamis in various scenarios from fjords to conical islands* (Doctoral dissertation, Georgia Institute of Technology).

Mohammed, F. and Fritz, H.M., 2012. Physical modeling of tsunamis generated by three-dimensional deformable granular landslides. *Journal of Geophysical Research: Oceans*, *117*(C11).

Monaghan, J.J. and Kos, A., 2000. Scott Russell's wave generator. *Physics of Fluids*, *12*(3), pp.622-630.

Montagna, F., Bellotti, G. and Di Risio, M., 2011. 3D numerical modeling of landslide-generated tsunamis around a conical island. *Natural hazards*, *58*, pp.591-608.

Muhari, A., Heidarzadeh, M., Susmoro, H., Nugroho, H.D., Kriswati, E., Wijanarto, A.B., Imamura, F. and Arikawa, T., 2019. The December 2018 Anak Krakatau volcano tsunami as inferred from post-tsunami field surveys and spectral analysis. *Pure and Applied Geophysics*, *176*, pp.5219-5233.

Mulligan, R.P., Franci, A., Celigueta, M.A. and Take, W.A., 2020. Simulations of landslide wave generation and propagation using the particle finite element method. *Journal of Geophysical Research: Oceans*, *125*(6), p.e2019JC015873.

Murty, T.S., 1979. Submarine slide-generated water waves in Kitimat Inlet, British Columbia. *Journal of Geophysical Research: Oceans*, *84*(C12), pp.7777-7779.

Murty, T.S., 2003. Tsunami wave height dependence on landslide volume. *Pure and applied geophysics*, *160*, pp.2147-2153.

Najafi-Jilani, A. and Ataie-Ashtiani, B., 2008. Estimation of near-field characteristics of tsunami generation by submarine landslide. *Ocean Engineering*, *35*(5-6), pp.545-557.

Nassiraei, H., Heidarzadeh, M. and Shafieefar, M., 2016. NUMERICAL SIMULATION OF LONG W AVES (TSUNAMI) FORCES ON CAISSON BREAKWATERS. *Sharif Journal of Civil Engineering*, *32*(3.2), pp.3-12.

Noda, E., 1970. Water waves generated by landslides. *Journal of the Waterways, Harbors and Coastal Engineering Division*, *96*(4), pp.835-855.

Omira, R. and Ramalho, I., 2020. Evidence-calibrated numerical model of December 22, 2018, Anak Krakatau flank collapse and tsunami. *Pure and Applied Geophysics*, *177*, pp.3059-3071.

Oppikofer, T., Hermanns, R.L., Roberts, N.J. and Böhme, M., 2019. SPLASH: semi-empirical prediction of landslide-generated displacement wave run-up heights. *Geological Society, London, Special Publications*, *477*(1), pp.353-366.

Oberkampf, W.L. and Trucano, T.G., 2002. Verification and validation in computational fluid dynamics. *Progress in aerospace sciences*, *38*(3), pp.209-272.

Pastor, M., Herreros, I., Merodo, J.F., Mira, P., Haddad, B., Quecedo, M., González, E., Alvarez-Cedrón, C. and Drempetic, V., 2009. Modelling of fast catastrophic landslides and impulse waves induced by them in fjords, lakes and reservoirs. *Engineering Geology*, *109*(1-2), pp.124-134.

Panizzo, A., De Girolamo, P. and Petaccia, A., 2005. Forecasting impulse waves generated by subaerial landslides. *Journal of Geophysical Research: Oceans*, *110*(C12).

Paris, A., Heinrich, P., Paris, R. and Abadie, S., 2020. The December 22, 2018 Anak Krakatau, Indonesia, landslide and tsunami: preliminary modeling results. *Pure and Applied Geophysics*, *177*(2), pp.571-590.

Rauter, M., Hoße, L., Mulligan, R.P., Take, W.A. and Løvholt, F., 2021. Numerical simulation of impulse wave generation by idealized landslides with OpenFOAM. *Coastal Engineering*, *165*, p.103815.

Pelinovsky, E., 2006. *Hydrodynamics of tsunami waves* (pp. 1-48). Springer Vienna.

Pelinovsky, E. and Poplavsky, A., 1996. Simplified model of tsunami generation by submarine landslides. *Physics and Chemistry of the Earth*, *21*(1-2), pp.13-17.

Putra, P.S., Aswan, A., Maryunani, K.A., Yulianto, E., Nugroho, S.H. and Setiawan, V., 2020. Post-event field survey of the 22 December 2018 Anak Krakatau tsunami. *Pure and Applied Geophysics*, *177*, pp.2477-2492.

Paris, A., Heinrich, P., Paris, R. and Abadie, S., 2020. The December 22, 2018 Anak Krakatau, Indonesia, landslide and tsunami: preliminary modeling results. *Pure and Applied Geophysics*, *177*(2), pp.571-590.

Panizzo, A., De Girolamo, P., Di Risio, M., Maistri, A. and Petaccia, A., 2005. Great landslide events in Italian artificial reservoirs. *Natural Hazards and Earth System Sciences*, *5*(5), pp.733-740.

Rabinovich, A.B., Thomson, R.E., Kulikov, E.A., Bornhold, B.D. and Fine, I.V., 1999. The landslide-generated tsunami of November 3, 1994 in Skagway Harbor, Alaska: A case study. *Geophysical Research Letters*, *26*(19), pp.3009-3012.

Ruffini, G., Heller, V. and Briganti, R., 2019. Numerical modelling of landslide-tsunami propagation in a wide range of idealised water body geometries. *Coastal Engineering*, *153*, p.103518.

Rabinovich, A.B., Thomson, R.E., Kulikov, E.A., Bornhold, B.D. and Fine, I.V., 1999. The landslide-generated tsunami of November 3, 1994 in Skagway Harbor, Alaska: A case study. *Geophysical Research Letters*, *26*(19), pp.3009-3012.

Robbe-Saule, M., Morize, C., Bertho, Y., Sauret, A., Hildenbrand, A. and Gondret, P., 2021. From laboratory experiments to geophysical tsunamis generated by subaerial landslides. *Scientific reports*, *11*(1), p.18437.

Ren, Z., Wang, Y., Wang, P., Hou, J., Gao, Y. and Zhao, L., 2020. Numerical study of the triggering mechanism of the 2018 Anak Krakatau tsunami: eruption or collapsed landslide?. *Natural Hazards*, *102*, pp.1-13.

Sælevik, G., Jensen, A. and Pedersen, G., 2009. Experimental investigation of impact generated tsunami; related to a potential rock slide, Western Norway. *Coastal Engineering*, *56*(9), pp.897-906.

Salmanidou, D.M., Heidarzadeh, M. and Guillas, S., 2019. Probabilistic landslide-generated tsunamis in the Indus Canyon, NW Indian Ocean, using statistical emulation. *Pure and Applied Geophysics*, *176*, pp.3099-3114..

Sassa, K., Dang, K., Yanagisawa, H. and He, B., 2016. A new landslide-induced tsunami simulation model and its application to the 1792 Unzen-Mayuyama landslide-and-tsunami disaster. *Landslides*, *13*, pp.1405-1419.

Satake, K. and Tanioka, Y., 2003. The July 1998 Papua New Guinea earthquake: Mechanism and quantification of unusual tsunami generation. *Pure and Applied Geophysics*, *160*, pp.2087-2118.

Shan, T. and Zhao, J., 2014. A coupled CFD-DEM analysis of granular flow impacting on a water reservoir. *Acta Mechanica*, *225*, pp.2449-2470.

Slingerland, R. and Voight, B., 1982. Evaluating hazard of landslide-induced water waves. *Journal of the Waterway, Port, Coastal and Ocean Division*, *108*(4), pp.504-512.

Synolakis, C.E. and Raichlen, F., 2003. Waves and run-up generated by a three-dimensional sliding mass. In *Submarine Mass Movements and Their Consequences: 1 st International Symposium* (pp. 113-119). Springer Netherlands.

Synolakis, C.E., Bardet, J.P., Borrero, J.C., Davies, H.L., Okal, E.A., Silver, E.A., Sweet, S. and Tappin, D.R., 2002. The slump origin of the 1998 Papua New Guinea tsunami. *Proceedings of the Royal Society of London. Series A: Mathematical, Physical and Engineering Sciences*, *458*(2020), pp.763-789.

Synolakis, C.E., Bardet, J.P., Borrero, J.C., Davies, H.L., Okal, E.A., Silver, E.A., Sweet, S. and Tappin, D.R., 2002. The slump origin of the 1998 Papua New Guinea tsunami. *Proceedings of the Royal Society of London. Series A: Mathematical, Physical and Engineering Sciences*, *458*(2020), pp.763-789.

Takagi, H., Pratama, M.B., Kurobe, S., Esteban, M., Aránguiz, R. and Ke, B., 2019. Analysis of generation and arrival time of landslide tsunami to Palu City due to the 2018 Sulawesi earthquake. *Landslides*, *16*, pp.983-991.

Tappin, D.R., Watts, P. and Grilli, S.T., 2008. The Papua New Guinea tsunami of 17 July 1998: anatomy of a catastrophic event. *Natural Hazards and Earth System Sciences*, *8*(2), pp.243-266.

Tinti, S., Armigliato, A., Manucci, A., Pagnoni, G., Zaniboni, F., Yalçiner, A.C. and Altinok, Y., 2006. The generating mechanisms of the August 17, 1999 Izmit bay (Turkey) tsunami: regional (tectonic) and local (mass instabilities) causes. *Marine Geology*, *225*(1-4), pp.311-330.

Tinti, S. and Tonini, R., 2013. The UBO-TSUFD tsunami inundation model: validation and application to a tsunami case study focused on the city of Catania, Italy. *Natural Hazards and Earth System Sciences*, *13*(7), pp.1795-1816.

Takabatake, T., Mäll, M., Han, D.C., Inagaki, N., Kisizaki, D., Esteban, M. and Shibayama, T., 2020. Physical modeling of tsunamis generated by subaerial, partially submerged, and submarine landslides. *Coastal Engineering Journal*, *62*(4), pp.582-601.

Takabatake, T., Han, D.C., Valdez, J.J., Inagaki, N., Mäll, M., Esteban, M. and Shibayama, T., 2022. Three-Dimensional Physical Modeling of Tsunamis Generated by Partially Submerged Landslides. *Journal of Geophysical Research: Oceans*, *127*(1), p. e2021JC017826.

Takagi, H., Pratama, M.B., Kurobe, S., Esteban, M., Aránguiz, R. and Ke, B., 2019. Analysis of generation and arrival time of landslide tsunami to Palu City due to the 2018 Sulawesi earthquake. *Landslides*, *16*, pp.983-991.

Tappin, D.R., Grilli, S.T., Harris, J.C., Geller, R.J., Masterlark, T., Kirby, J.T., Shi, F., Ma, G., Thingbaijam, K.K.S. and Mai, P.M., 2014. Did a submarine landslide contribute to the 2011 Tohoku tsunami? *Marine Geology*, *357*, pp.344-361.

Tang, G., Lu, L., Teng, Y., Zhang, Z. and Xie, Z., 2018. Impulse waves generated by subaerial landslides of combined block mass and granular material. *Coastal Engineering*, *141*, pp.68-85.

Takabatake, T., Mäll, M., Han, D.C., Inagaki, N., Kisizaki, D., Esteban, M. and Shibayama, T., 2020. Physical modeling of tsunamis generated by subaerial, partially submerged, and submarine landslides. *Coastal Engineering Journal*, *62*(4), pp.582-601.

Takagi, H., Pratama, M.B., Kurobe, S., Esteban, M., Aránguiz, R. and Ke, B., 2019. Analysis of generation and arrival time of landslide tsunami to Palu City due to the 2018 Sulawesi earthquake. *Landslides*, *16*, pp.983-991.

Van Nieuwkoop, J.C.C., 2007. Experimental and numerical modelling of tsunami waves generated by landslides.

Wang, J., Ward, S.N. and Xiao, L., 2019. Tsunami Squares modeling of landslide generated impulsive waves and its application to the 1792 Unzen-Mayuyama mega-slide in Japan. *Engineering Geology*, *256*, pp.121-137.

Wang, Y., Liu, J., Li, D. and Yan, S., 2017. Optimization model for maximum tsunami amplitude generated by riverfront landslides based on laboratory investigations. *Ocean Engineering*, *142*, pp.433-440.

Watts, P., 2000. Tsunami features of solid block underwater landslides. *Journal of waterway, port, coastal, and ocean engineering*, *126*(3), pp.144-152.

Watts, P., 1998. Wavemaker curves for tsunamis generated by underwater landslides. *Journal of waterway, port, coastal, and ocean engineering*, *124*(3), pp.127-137.

Watts, P., 1997. *Water waves generated by underwater landslides*. California Institute of Technology.

Watts, P., Grilli, S.T., Kirby, J.T., Fryer, G.J. and Tappin, D.R., 2003. Landslide tsunami case studies using a Boussinesq model and a fully nonlinear tsunami generation model. *Natural hazards and earth system sciences*, *3*(5), pp.391-402.

Watts, P., Grilli, S.T., Tappin, D.R. and Fryer, G.J., 2005. Tsunami generation by submarine mass failure. II: Predictive equations and case studies. *Journal of waterway, port, coastal, and ocean engineering*, *131*(6), pp.298-310.

Wessel, P. and Smith, W.H., 1998. New, improved version of Generic Mapping Tools released. *Eos, Transactions American Geophysical Union*, *79*(47), pp.579-579.

Wiegel, R.L., 1955. Laboratory studies of gravity waves generated by the movement of a submerged body. *Eos, Transactions American Geophysical Union*, *36*(5), pp.759-774.

Wei, G., 2005. A fixed-mesh method for general moving objects in fluid flow. *Modern Physics Letters B*, *19*(28n29), pp.1719-1722.

Xue, H., Ma, Q., Diao, M. and Jiang, L., 2019. Propagation characteristics of subaerial landslide-generated impulse waves. *Environmental Fluid Mechanics*, *19*, pp.203-230.

Yakhot, V. and Orszag, S.A., 1986. Renormalization group analysis of turbulence. I. Basic theory. *Journal of scientific computing*, *1*(1), pp.3-51.

Yavari-Ramshe, S. and Ataie-Ashtiani, B., 2016. Numerical modeling of subaerial and submarine landslide-generated tsunami waves—recent advances and future challenges. *Landslides*, *13*, pp.1325-1368.

Yin, Y.P., Huang, B., Chen, X., Liu, G. and Wang, S., 2015. Numerical analysis on wave generated by the Qianjiangping landslide in Three Gorges Reservoir, China. *Landslides*, *12*, pp.355-364.

Yuk, D., Yim, S.C. and Liu, P.F., 2006. Numerical modeling of submarine mass-movement generated waves using RANS model. *Computers & geosciences*, *32*(7), pp.927-935.

Zahraei, S.M. and Heidarzadeh, M., 2007. Destructive effects of the 2003 bam earthquake on structures.

Zengaffinen, T., Løvholt, F., Pedersen, G.K. and Muhari, A., 2020. Modelling 2018 Anak Krakatoa Flank Collapse and Tsunami: effect of landslide failure mechanism and dynamics on tsunami generation. *Pure and Applied Geophysics*, *177*, pp.2493-2516.

Zweifel, A., 2004. *Impulswellen: Effekte der Rutschdichte und der Wassertiefe* (Doctoral dissertation, ETH Zurich).

Zweifel, A., Hager, W.H. and Minor, H.E., 2006. Plane impulse waves in reservoirs. *Journal of waterway, port, coastal, and ocean engineering*, *132*(5), pp.358-368.

Appendix

Solid-blocks

Sliding blocks used in this study for physical experiments Sb_{1-4}. See Table (3.2) for properties of these blocks.

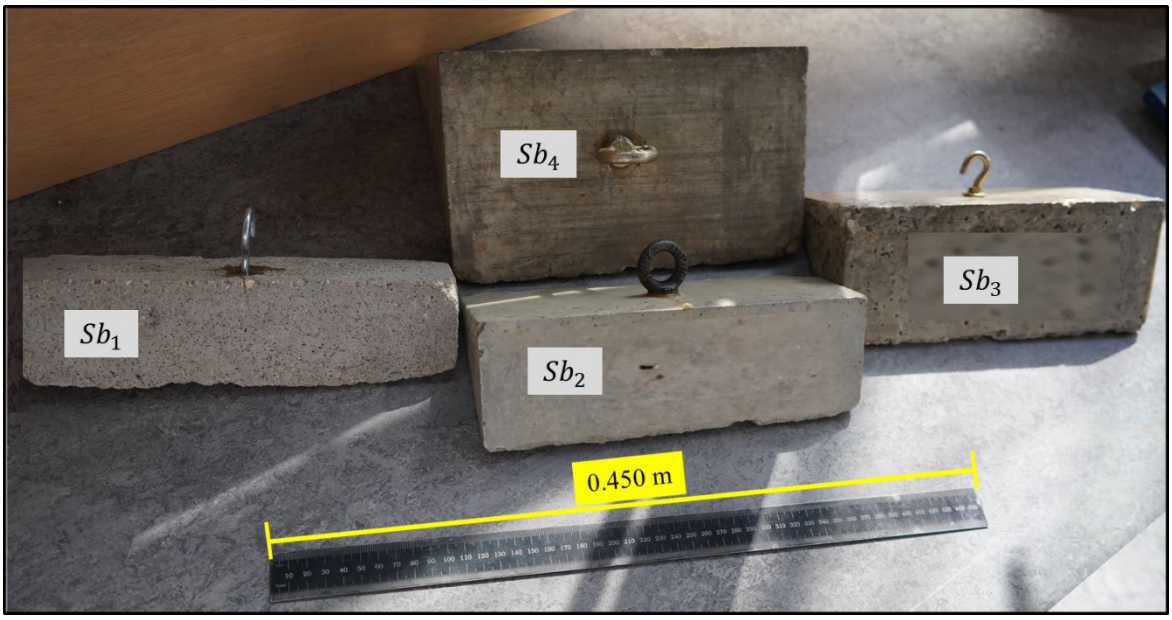

Ramtin Sabeti

I am a hydraulic engineer with expertise in modelling tsunami waves generated by landslides. I am broadly interested in studying the submarine and subaerial landslide generated waves. My current research (2019-2022) focuses on *physical modelling and numerical simulation of landslide generated waves*. My contention is that this research can help engineers and scientists by providing a preliminary and rapid estimate of the potential hazards associated with submarine/subaerial landslides. My writing related to landslide-generated waves has appeared in Natural Hazard Journal, Landslide's Journal, Journal of waterway port coastal, Ocean Engineering Journal, and Coastal Engineering Journal among various other publications. I hold a Master of Science with distinction in Water Engineering from Brunel University London (2017-2018), and a Master of Science in Water Resources Management from Azad University Central Tehran (with distinction) (2014-2016), where I also received his Bachelor of Science degree in Civil Engineering-Water (2009-2013). After my graduation, Ramtin worked for various companies in Tehran as a design engineer.